ABSTRACT

ZHANG, JIAYONG. Vibrational Spectroscopy of Complex Materials: First-principles Calculations and Inelastic Neutron Scattering Study. (Under the direction of Jerzy Bernholc.)

The studies on vibrational spectroscopy are playing very important roles in multiple disciplines, and both theoretical frameworks and experimental techniques have been well developed. On the one hand, the progress made in experimental techniques such as neutron scattering with high resolutions can now enable people to obtain more detailed vibrational information in phonon spectra and phonon dispersions. On the other hand, with the advancement of first-principles molecular dynamics (MD) and total energy calculations within density functional theory (DFT), one can now simulate the vibrational properties of molecules and crystals and access the phonon information including phonon modes, phonon density of states, and phonon interactions with other particles. Combination of the high-resolution experimental spectra and the highly accurate theoretical simulation, we can gain deep a understanding of new materials. This work will make use of those techniques to provide a better understanding of vibrational spectroscopy and phonon behaviors in complex materials.

In this dissertation, three projects have been addressed:

(I) The methodology of large-scale phonon calculation with the real-space multigrid (RMG) method. The RMG package is used as the core kernel for ab initio molecular dynamics (AIMD) and total energy calculations, the phonon properties are investigated based on both lattice dynamics method (finite displacement method, FDM) and AIMD. By comparing with other widely used DFT packages and experimental data from inelastic neutron scattering (INS), we demonstrate that RMG is very accurate in

calculating forces at small displacements from equilibrium positions. The calculated phonon band structures and vibrational spectra for a variety of different systems are in very good agreement with simulated results by other plane-waves-based DFT codes, Quantum ESPRESSO, CASTEP, and VASP, as well as inelastic neutron scattering experimental data.

(II) The anharmonicity in zirconium hydrides. A detailed study on the anharmonicity of zirconium hydrides/deuterides is performed by exploring the 2D potential energy surface of hydrogen/deuterium atoms. The corresponding 2D single-particle Schrodinger equation is solved to get the phonon eigenfrequencies. We demonstrated that the obtained results can well describe the experimental INS spectra, typically the strong anharmonicity at high energies.

(III) The high pressure induced phase change in alkali hydrides. We have measured the INS spectra of NaH at pressures 1 and 2 GPa for the first time and simulated INS from the first-principles calculations with either local density approximation (LDA) or the generalized gradient approximation (GGA). Thermodynamic properties such as lattice parameters, bulk modulus, and their derivatives are calculated using full lattice dynamics theory within the quasi-harmonic approximation (QHA) for all alkali hydrides. Anharmonic effects are investigated from the molecular dynamics trajectories and are found to be negligible at a given temperature and pressure.

© Copyright 2020 by Jiayong Zhang

All Rights Reserved

Vibrational Spectroscopy of Complex Materials: First-principles Calculations and Inelastic Neutron Scattering Study

by
Jiayong Zhang

A dissertation submitted to the Graduate Faculty of
North Carolina State University
in partial fulfillment of the
requirements for the Degree of
Doctor of Philosophy

Physics

Raleigh, North Carolina

2020

APPROVED BY:

Wenchang Lu	Lubos Mitas
Matthias Stallmann	Jerzy Bernholc Chair of Advisory Committee

DEDICATION

To my parents, my sister, and my wife.

BIOGRAPHY

The author was born in a small town called Leqiao in Chaohu city (now Hefei city), Anhui Province, P.R.C. Before enrolling in University of Science and Technology of China (USTC) in 2010 as an undergraduate student in physics, he spent his most valuable three years in Lujiang No.1 Middle School, where he found his love of life. He obtained his B.S. in physics in 2014.

In the same year, the author entered North Carolina State University to pursue his Ph.D. in physics. He later joined Prof. Jerzy Bernholc's high-performance simulation group to conduct research on first-principles calculations with the real-space multigrid method. During his Ph.D., he also spent four years at Oak Ridge National Laboratory for his thesis work supervised by Dr. Anibal J. Ramirez-Cuesta. One very important thing that happened to the author during his fifth year of Ph.D. is the marriage to his high school classmate.

Besides research, the author also likes reading, traveling, and table-tennis.

ACKNOWLEDGEMENTS

First, I would like to express my highest gratitude and appreciation to my advisor Prof. Jerzy (Jerry) Bernholc for his guidance and inspiration during my Ph.D. time at NC State. His constant support and insightful advice keep me moving forward during my whole research. Without his help, it will be impossible for me to finish this work.

I would like to thank all current and former members of the Bernholc group: Dr. Wenchang Lu, who has guided me through my first steps in density functional theory and phonon calculations, and has given me so much detailed advice in my research. Dr. Emil Briggs, for his development on the RMG code and my discussions with him on RMG simulations. Dr. Miroslav Hodak, who has inspired me on computational physics at my beginning time in the Bernholc group. Bing Zhang, Dr. Zhongcan Xiao, Dr. Yan Li, and Dr. Rui Dong, for their useful and inspiring discussions with me from research to life. Your work impressed me and inspired me a lot. I also wish all the best to younger students, Hancheng Qin and Jiale Chen, for their developments in the future.

I also wish to acknowledge the help and support from my supervisor and collaborators at Oak Ridge National Laboratory. Dr. Anibal J. (Timmy) Ramirez-Cuesta and Dr. Yongqiang (YQ) Cheng have provided me with so many useful discussions and introduced me to neutron scattering. Their patience and willingness to share their knowledge have deepened my understanding of neutron scattering and phonon theory. Dr. Anup Pandey, Dr. Alexander I. Kolesnikov and Dr. Eugene Mamontov have shared so many interesting physical phenomena and ideas with me. It was a nice experience working with you all.

Thanks to my committee members, Prof. Lubos Mitas for his illuminating lectures

on computational physics, and Prof. Matthias Stallmann for his fascinating lectures on algorithms. Those courses have inspired me so much on programming, computations, and analysis in my research.

Finally, my deepest thanks go to my parents, Quangen Zhang and Shiyun Rao; my sister, Yan Zhang, for their unconditional love and support throughout all those years I spent in studying. You make a happy and warm family for me. And especially, all my gratitude is due to my friend, family member, and lover, Min Tian. Your accompaniment, encouragement, and support have been a continuous source of power and inspiration to drive me forward. You make my world go around.

TABLE OF CONTENTS

LIST OF FIGURES . . . . . **ix**

LIST OF TABLES . . . . . **xiv**

Chapter 1 Introduction **1**

Chapter 2 Theoretical and Computational Background: Density Functional Theory and Molecular Dynamics **6**
2.1 Pre-Density Functional Theory 7
2.1.1 The Quantum Many-Body Problem 7
2.2 Density Functional Theory 8
2.2.1 Born-Oppenheimer Approximation 8
2.2.2 Hohenberg-Kohn Theorems 9
2.2.3 The Kohn-Sham *Ansatz* and the Kohn-Sham Equations 10
2.2.4 Exchange-Correlation Functional 12
2.2.5 Basis Sets 13
2.2.6 Pseudopotentials 15
2.2.7 Numerical Considerations 19
2.3 Real-Space Multi-Grid Method 19
2.3.1 Real-space Kohn-Sham Equations 21
2.3.2 Algorithms and Implementations 22
2.4 Molecular Dynamics 24
2.4.1 Classical MD 25
2.4.2 *Ab Initio* MD 25
2.4.3 Ensembles 26

Chapter 3 Theoretical and Computational Background: Phonons **28**
3.1 Classical Lattice Dynamics Theory 29
3.2 Harmonic Phonon Theory 31
3.2.1 Implementation: FDM 32
3.2.2 Implementation: DFPT 33
3.2.3 FDM & DFPT: Connections and Differences 36
3.3 Quasi-Harmonic Phonon Theory 37
3.3.1 Theory 37
3.3.2 Thermal Quantities 38
3.4 Anharmonic Phonon Theory 39
3.4.1 Phonon Scattering in Solids 39
3.4.2 Phonon Calculations from MD 44

Chapter 4 Inelastic Neutron Scattering **48**
4.1 Introduction to Neutron Scattering 49
4.2 Neutron Scattering: Theory and Simulations 50
4.2.1 Scattering Theory 50
4.2.2 Simulations: the OCLIMAX Software 53
4.3 Neutron Spectrometers 54
4.3.1 Indirect Geometry: VISION 54

Chapter 5 Large-Scale Phonon Calculations Using the Real-Space Multi-grid Method **57**
5.1 Abstract 58
5.2 Introduction 58
5.3 Methodology 62
5.4 Results and Discussion 67
5.4.1 Silicon 68
5.4.2 Zirconium(II) Hydride 68
5.4.3 Carbazole 72
5.4.4 ZIF-8 74
5.5 Summary and Conclusions 74

Chapter 6 Study of Anharmonicity in Zirconium Hydrides using Inelastic Neutron Scattering and *Ab initio* Computer Modeling **76**
6.1 Abstract 77
6.2 Introduction 77
6.3 Methods 80
6.4 Results and discussion 82
6.4.1 Atomic structures and phonon properties of ZrH_x 82
6.4.2 Harmonic approximation: frozen phonon method 85
6.4.3 A direct method: mapping eigenfrequencies from Schrödinger equations with simulated INS spectra 87
6.5 Conclusion 98

Chapter 7 Theoretical Study of Alkali-Metal Hydrides at High Pressures: A case of NaH Supported by Inelastic Neutron Scattering (INS) Experiments at 1 and 2 GPa **100**
7.1 Abstract 101
7.2 Introduction 101
7.3 Methodology 103
7.4 Results and Discussion 106
7.4.1 Inelastic Neutron Spectroscopy (INS) 106
7.4.2 Phase Change with Pressure and Thermodynamic Properties . . 111

7.4.3 Phonon Dispersion and Born Charges 116
7.5 Summary and Conclusions 118

Chapter 8 Summary and Outlook 120

BIBLIOGRAPHY 122

APPENDIX 134
Appendix A Supplementary Information for Chapter 6 135
A.1 Eigen states based on 2D Schrödinger equation 135
A.2 Comparisons of eigenfrequencies among ZrH_x 135
A.3 The probability distribution of H atoms in ZrH_2 138

LIST OF FIGURES

Figure 2.1 Typical workflow to computationally solve the Kohn-Sham equations self-consistently. 20

Figure 3.1 The harmonic & anharmonic potentials of an atom's vibration and its eigenvalues. Adapted from [53]. 32

Figure 4.1 The trajectory map (Q, ω) of an INS spectrometer with a low fixed final energy for two scattering angles: 45 and 135. The inset shows the scattering triangle for the case where $k_i \gg k_f$. Adapted from [30]. 55

Figure 5.1 Phonon dispersions of crystalline silicon calculated by QE-Phonopy (blue) and RMG-Phonopy (red). The results are nearly identical, and the two curves fall on top of each other. 69

Figure 5.2 Phonon dispersions of ZrH_2 calculated by RMG-Phonopy (red) and QE-Phonopy (blue). 70

Figure 5.3 Vibrational spectra from RMG-Phonopy (red), QEPhonopy (blue), RMG-ALAMODE (cyan), and VISION's experimental data (black) at 5 K for ZrH_2. Overtone peaks, which correspond to multiple phonon scattering events, are generated by the convolution of the DFT-calculated fundamental peaks by the OCLIMAX software. The peaks below 200 meV are from onephonon scattering events, while those above 200 meV result from the scattering of two or more phonons. Extra sharp peaks marked by black arrows might be due to anharmonic effects. 71

Figure 5.4 Normalized intensity comparisons between RMG-Phonopy (red), QE-Phonopy (blue), VASP-Phonopy (green), CASTEP (magenta), and experimental data (black) at 5 K for carbazole. 73

Figure 5.5 Comparisons of low-frequency vibrational intensities among RMG-Phonopy (red), QE-Phonopy (blue), and experimental data (black) at 5 K for ZIF-8. 75

Figure 6.1 (a) Crystal unit cells for ϵ-ZrH_2 (space group I4/mmm), γ-ZrH and γ-ZrD (both are of space group Cccm), where H atoms in red exist in all structures, and H atoms in black only exist in ϵ-ZrH_2. Note that in calculations, lattice constants of ϵ-ZrH_2 and γ-ZrD(H) are different. Color scheme: Zr, green; H, red/black. Figures are drawn using the VESTA program [121]. (b), (c) and (d) are calculated phonon dispersions and PDOS for γ-ZrD, γ-ZrH and ϵ-ZrH_2, respectively. The BZ paths and notation are adopted from [122]. 83

Figure 6.2 The INS spectra for ϵ-ZrH_2 measured with the VISION instrument at 5K (blue), γ-ZrH (red) at 4.5K and γ-ZrD (black) at 30K measured with the TFXA spectrometer. Spectra have been normalized to the same maximum value of the fundamental peaks for comparison purposes. Note that γ-ZrD sample has been contaminated by $\sim$1 at.% H, and also contained α- and δ-phases [98], with the actual ratio of Zr atoms in the different phases as $0.718(\alpha\text{-}ZrD_{0.001})+0.269(\gamma\text{-}ZrD_{0.98})+0.013(\delta\text{-}ZrD_{1.2})$, which results in extra peaks at $\sim$140 meV and higher intensity of the lattice modes (<30 meV) compared to the expected spectrum for pure γ-ZrD. Figures are drawn using the Mantid program [123]. . . . 84

Figure 6.3 VISION INS spectrum (red) at 5K and simulated spectra with RMG (green) and VASP (blue) at 0K of ϵ-ZrH_2. Spectra are normalized with respect to their area under the fundamental spectra curve. Black arrows are marking peaks resulted from anharmonic effect (split peaks). The simulated data assumes the harmonic approximation. 86

Figure 6.4 PDOS comparisons between γ-ZrD (black) and scaled high energy modes of γ-ZrD (magenta), γ-ZrH (red), and ϵ-ZrH_2 (blue). The high energy modes of γ-ZrD are scaled by a factor of $\sqrt{2}$ in energy, and $1/\sqrt{2}$ in intensity to obey DOS properties, which are represented by the black arrow. Low energy modes are almost identical between γ-ZrH and γ-ZrD, while high energy modes are nearly identical after scaled. 88

Figure 6.5 Crystal unit cells with sampling plane, contour plots and sectional views (blue curves) of PES for ZrH_x. (a)(b)(c)(d): plane (112) of ϵ-ZrH_2; (e)(f)(g)(h): plane (-112) of γ-ZrH and γ-ZrD. Color scheme: Zr, green; H, white; sampling plane: pink. The energy range within (0, 12) eV with 50 levels are used in contour plots, with minimum energies of 0 are all located at (0, 0). Red lines in (c) and (g) are enlarged plots in vertical directions within the energy range of (0, 1) eV, and black lines are indicating the first six eigenfrequencies (see Fig. **??**) from Schrödinger equations of ϵ-ZrH_2 and γ-ZrD, respectively. 91

Figure 6.6 Comparisons between eigenfrequencies from Schrödinger equations and experimental INS spectra for: (a) ϵ-ZrH_2, (b) γ-ZrH, (c) γ-ZrD. Eigenfrequencies from Schrödinger equations are in red lines, experimental INS spectra are in black solid lines, simulated INS spectra are in magenta lines, and the black dashed lines are for eye guidance of comparisons between eigenfrequencies and anharmonic peaks for the first to third overtones. 94

Figure 6.7 A schematic figure showing the convolution procedure. The convolution procedure was done within each individual quantum event indexed by n. Magenta lines are indicating simulation results, red are results from direct solutions from the Schrödinger equation, and blue lines are adjusted results after convolution between simulations and eigenfrequencies. 96

Figure 6.8 INS spectra for: (a) ϵ-ZrH_2, (b) γ-ZrH, (c) γ-ZrD. Eigenfrequencies from Schrödinger equations are in red lines, experimental INS spectra are in black lines, simulated INS spectra are in magenta lines, blue lines represent adjusted spectra after convolution, and purple lines in (c) are simulated spectra of contaminated γ-ZrD. Spectra are normalized with respect to their area under the fundamental spectra curve. The ratio of neutron scattering cross-section of H and D is 82.02/7.64=10.74, and m(D)/m(H)=2, therefore fundamental modes intensities ratio of 3% H to 97% D should be $\sim$10.74*2*0.03/0.97=0.66 (without corrections for the Debye-Waller factor). Note that in (c), the simulation spectra of ZrD and $ZrD_{0.96875}H_{0.03125}$ are almost on top of each other. 97

Figure 7.1 Variation of Helmholtz free energy at 5 K and the density functional theory (DFT) static energy for NaCl-type structure of NaH with volume using LDA. Corresponding minimum energies are shown by the respective arrows. 107

Figure 7.2 Inelastic neutron scattering (INS) spectrum of NaH at 0 GPa pressure (black) at temperature 5 K measured at a VISION spectrometer at Spallation Neutron Source (SNS). Simulated INS spectra for NaCl-type structure of NaH at the static energy equilibrium structure (blue) and free-energy equilibrium structure at 5 K (red) using DFT under LDA. 108
Figure 7.3 Inelastic neutron scattering (INS) spectrum of NaH at pressures 0, 1, and 2 GPa and temperature 5 K from the VISION spectrometer at Spallation Neutrons Source (SNS). Arrows show the shift in starting positions of peaks around 500 cm^{-1}. The region below 500 cm^{-1}, shown by the arrow, is dominated by the background peaks from the CuBe sample holder can. (Middle panel) Simulated INS for the NaCl-type structure of NaH at 5 K using DFT under GGA at experimental pressures. (Lowest panel) Simulated INS for the NaCltype structure of NaH at 5 K using DFT under LDA. Black: equilibrium volume, red: 1 GPa and blue: 2 GPa. . . 110
Figure 7.4 Gibbs Free energy as a function of pressure for NaCl-type and CsCl-type structures of NaH using LDA and GGA at 298 K. (a) NaH for calculations using LDA and (b) NaH for calculations using GGA. 112
Figure 7.5 Gibbs Free energy as a function of pressure for NaCl-type and CsCl-type structures of KH and RbH using LDA at 298 K. (a) KH and (b) RbH. 113
Figure 7.6 Equation of state for the NaCl-type structure of NaH at 298 K. Phase-change volume is shown in the small bracket. The experimental regions are shown in the inset by the arrows where inelastic neutrons scattering (INS) are simulated using the Oclimax software. "a" represents the equilibrium region with zero pressure, "b" and "c" are low-pressure regions with pressures 1 and 2 GPa, respectively. 114
Figure 7.7 Phonon dispersion of NaH at different pressures. Solid lines are from the lattice dynamics calculations and the broken lines are from the finite-temperature phonon calculations from the MD trajectories. (a) NaH at V_0 (equilibrium volume), (b) NaH at V/V_0 = 0.96 (1 GPa), (c) NaH at V/V_0 = 0.92 (2 GPa) and (d) NaH at V/V_0 = 0.61 (PCP). 117
Figure 7.8 Phonon dispersion of NaH at volumes before and after phonon softening to zero. (a) NaH at V/V_0 = 0.48 (P = 71.76 GPa) and (b) NaH at V/V_0 = 0.46 (P = 81.55 GPa). 118

Figure A.1 First fifteen eigenfrequencies and wavefunctions of H/D for: (a) (112) plane of ϵ-ZrH_2, (b) (-112) plane of ZrH, and (c) (-112) plane of ZrD. 137
Figure A.2 Comparisons of eigenfrequencies by solving Schrödinger equations for ZrH_x in the energy range below 1000 meV. 138
Figure A.3 Unnomalized probability distributions of H atom in ZrH_2 in (112) plane along x (blue) and y (red) directions, where the dashed lines are indicating full width at half maximum (FWHM). 139

LIST OF TABLES

Table 2.1 Central difference scheme coefficients 23

Table 4.1 Some physical properties of neutrons [85]. 49

Table 6.1 Calculated MSD (and $\sqrt{MSD}$ in brackets) of Zr at (0, 0, 0), H/D at $(3/4, 1/4, 3/4)$ for ZrH_x in different energy range, units are in $Å^2$ for MSD and Å for $\sqrt{MSD}$. In γ-ZrH(γ-ZrD), MSD(Zr) varies slightly at different Zr positions (within 3%). 89

Table 7.1 Shift in First and Second Peak Positions for 1 and 2 GPa Relative to Zero Pressure (0 GPa) 111

Table 7.2 Phase-Change Pressure (PCP) and Volume Fraction (V/V_0) at the Phase Change for Alkali Hydrides from Lattice Dynamics Calculations. V_0 is the Equilibrium Volume 112

Table 7.3 Equilibrium Lattice Constant (a), the Bulk Modulus (B_0) and its First Derivative (B_0') for Alkali Hydrides from the Lattice Dynamics Calculations compared to Experimental and Theoretical Results 115

Table 7.4 Calculated Born Effective Charges and LO-TO Gap for NaH at Different Pressures 119

CHAPTER 1

INTRODUCTION

The study of phonons plays an important part in multiple disciplines, including condensed matter physics, chemistry, mechanical engineering, etc. In particular, the long-wavelength phonons give rise to sound in solids, hence the name phonē in Greek, or phonon. Ever since the concept was introduced in as early as 1932, phonons have found wide applications in studies of heat dissipation [1–3], thermoelectric devices [4–6], surface physics [7, 8], and potential usage in newly emerging fields such as phononics [9, 10], quantum computing [11, 12], etc. Thus, for the past few decades, lots of phonon theories and experimental techniques have been developed, and some of them are briefly overviewed here.

From the theoretical perspective, in the 1950s, Born and Huang's work [13] on the dynamical theory of crystal lattices presents a systematic study of phonons by describing the dynamical and thermodynamical properties of crystal lattices in the classical limit. Under Born-von Karman periodic boundary conditions, one can derive

the phonon dynamical equations analytically for small systems. However, analytical solutions are impractical for large or even moderate-size systems, or when quantum-mechanical effects are explicitly included. Several methods have been developed since then, including the Thomas-Fermi approximation, the Hartree-Fock approximation, etc.. Nevertheless, all these methods have accuracy limitations. With the advancement of the *ab initio* methods and modern supercomputers, and especially the development of density functional theory (DFT) [14, 15], accurate phonon methodologies and calculations are possible. In the 1990s, the finite displacement method (FDM) [16–18] and density functional perturbation theory (DFPT) [19, 20] method were developed, making phonon calculations practical, accurate and cost-efficient. Those two methods, however, have some limitations: 1) they are based on harmonic approximation, which means that there are no interactions between phonons and other (quasi-) particles (like electrons, polaritons, etc.); 2) DFT simulations are limited to 0K, thus finite temperature effects cannot be simulated; 3) due to the $O(N^4)$ scalability in most phonon calculations, system sizes are limited to at most a few hundred atoms. To address those limitations, quasi-harmonic and anharmonic phonon theories have been developed to deal with the situation when the harmonic approximation fails, and phonon interactions with other particles have also been studied. Later studies revealed that phonon-phonon interactions are essential to explain thermal properties, and electron-phonon interactions are fundamental in conventional superconductivity. For the temperature effects, the velocity autocorrelation function [21] obtained from molecular dynamics (MD) includes anharmonic and temperature effects. More recently, the temperature-dependent effective potential (TDEP) method [22] and the Green's function MD (GFMD) [23] based on the fluctuation-dissipation theorem allow researchers to explore phonon properties beyond the harmonic regime. Our

group's real-space-based phonon methodology has recently proven to be efficient for large-scale phonon calculations [24].

From the experimental perspective, many experimental techniques have been developed. Infra-red (IR) [25] and Raman spectroscopy [26] can be used to probe the optical phonon interactions with photons. Both methods, however, are subject to selection rules arising from conservation laws of energy and momentum and symmetry constraints. Furthermore, the optical phonon modes are restricted to the first Brillione Zone (BZ). X-ray scattering [27], on the other hand, can be used to probe phonon modes across the whole BZ. However, X-rays have limitations as their energy is normally two orders of magnitude larger than phonons' energy, which causes difficulties in determining phonons' energy. Surface phonons can be alternatively probed by Electron-Energy-Loss Spectroscopy (EELS) [28] and Helium Atom Scattering [29] techniques. As the state-of-the-art probing method, neutron scattering techniques [30, 31] have been widely used to further detect atomic vibrations in materials because of their advantages of no selection rules and non-destructive probing. Neutron scattering is the technique of focus in this thesis.

In this monograph, we first review the theoretical and experimental background of the presented research. Beginning with the Schrödinger equation, I will introduce some basic concepts and theorems before we dive into DFT in chapter 2. Phonon theory based on the lattice dynamics theory is then introduced in chapter 3, and experimental techniques in phonon analysis are discussed in chapter 4.

The thesis then presents our results and findings. In chapter 5, I will introduce our real-space phonon methodology with RMG and Phonopy/ALAMODE, along with its applications to various materials. The RMG code is extremely suitable for large-scale systems' phonon calculations. The simulated INS spectra with RMG are

compared with the results from other DFT codes and experiments. In chapter 6, I will describe the anharmonic phonon behaviors in zirconium hydrides. It was found that the spectra simulated with the harmonic approximation are in good agreement with the experiment at phonon energy lower than 200 meV. Strong anharmonicity exists at energy higher than 200 meV and the spectra in this range cannot be explained with the harmonic approximation. Since the high-frequency modes are related to the hydrogen/deuterium vibrations, we investigate the anharmonicity by calculating the 2D potential energy surface around H/D equilibrium positions. We find that the eigenfrequencies from 2D Schrödinger equations can describe well the anharmonicity in experimental spectra up to 600 meV. In chapter 7, I will discuss our study of high-pressure effects on alkali hydrides by using quasi-harmonic approximations and MD-based phonon calculations. It was found that the phonon softening to negative frequencies is insufficient to predict the phase-change pressure in NaH, and both the zero-point energy and the thermal contributions to the static energy are essential for accurate prediction of the phase-change pressure. And finally, the conclusion and outlook from this research will be presented in chapter 8.

The research presented in this thesis has resulted in the following publications:

1. J. Zhang, Y. Cheng, W. Lu, E. Briggs, A. J. Ramirez-Cuesta, and J. Bernholc, Large-scale phonon calculations using the real-space multigrid method, Journal of Chemical Theory and Computation (2019).

2. Jiayong Zhang, Yongqiang Cheng, Wenchang Lu, Jerzy Bernholc, Anibal J. Ramirez-Cuesta, Study of anharmonicity in Zirconium Hydrides using inelastic neutron scattering and *ab initio* computer modeling. Submitted to Physical Review B.

3. A. Pandey, J. Zhang, Y. Cheng, L. Daemen, and A. J. Ramirez-Cuesta, Theoretical Study of Alkali-Metal Hydrides at High Pressures: A Case of NaH Supported by Inelastic Neutron Scattering (INS) Experiments at 1 GPa and 2 Gpa, The Journal of Physical Chemistry A 123, 10079 (2019).

CHAPTER 2

THEORETICAL AND COMPUTATIONAL BACKGROUND: DENSITY FUNCTIONAL THEORY AND MOLECULAR DYNAMICS

In this chapter, we review the theoretical and computational background that is employed in this work, with a focus on DFT and MD methods.

2.1 Pre-Density Functional Theory

2.1.1 The Quantum Many-Body Problem

To describe a many-body system in quantum mechanics, the essential and fundamental property is the wavefunctions $|\psi\rangle$. With the wavefunctions, one can easily calculate charge density, eigenstates, atomic forces, stress, etc. Starting with the time-independent Schrödinger equation in quantum mechanics,

$$H\,|\psi\rangle = E\,|\psi\rangle \tag{2.1}$$

where H is the Hamiltonian of the system and E is the system's energy, other observables at the ground state are calculated by:

$$o(|\psi\rangle) = \langle\psi|\,o\,|\psi\rangle \tag{2.2}$$

The Hamiltonian of a complex system is

$$H = -\frac{\hbar^2}{2m_e}\sum_i \nabla_i^2 - \frac{\hbar^2}{2m_I}\sum_I \nabla_I^2 + \sum_i\sum_{j>i}\frac{e^2}{|r_i - r_j|} + \sum_I\sum_{J>I}\frac{Z_I Z_J e^2}{|R_I - R_J|} - \sum_{i,I}\frac{Z_I e^2}{|r_i - R_I|} \tag{2.3}$$

where lower case subscripts are labeling electrons and upper case subscripts are labeling nuclei. The first two terms are denoting the kinetic energies of electrons and nuclei, respectively, and the last three terms are electron-electron, nuclei-nuclei, and electron-nuclei Coulomb interactions. Due to the complexity of the Coulomb interaction terms, Eq. 2.1 is unsolvable analytically when the number of electrons is larger than one.

Considering the fact that the mass ratio of proton/electron is ~ 1836, one may assume that electrons move much faster than nuclei. Within Born-Oppenheimer approximation (which is to be discussed later), Eq. 2.3 can be rewritten as:

$$\begin{aligned} H &= T + V_{int} + V_{ext} \\ &= -\frac{1}{2}\sum_i \nabla_i^2 + \sum_i \sum_{j>i} \frac{1}{|r_i - r_j|} - \sum_{i,I} \frac{Z_I}{|r_i - R_I|} \end{aligned} \tag{2.4}$$

Here we use the atomic units with $\hbar = m_e = e = 1$.

With Eq. 2.4, the number of degrees of freedom is reduced dramatically. However, it is still unsolvable for real-world problems, which could involve hundreds to millions of atoms. Thus, multiple approximations have been employed to address this problem, including Thomas-Fermi-Dirac models, Hartree-Fock approximation, and density functional theory (DFT).

2.2 Density Functional Theory

2.2.1 Born-Oppenheimer Approximation

To make the Schrödinger equation solvable and retain reliable results, it is important to assume the movements of electrons and nuclei are independent and to decouple their movements (which is the so-called Born-Oppenheimer approximation or adiabatic approximation),

$$|\psi\rangle (r, R) = |\psi\rangle_e (r, R) \, |\psi\rangle_n (R) \tag{2.5}$$

where $|\psi\rangle_n (R)$ are the wavefunctions of the nuclei that depend on their positions R, and $|\psi\rangle_e (r, R)$ are the electronic wavefunctions that depend on positions of both

nuclei and electrons r.

Substituting this equation into Eq. 2.1, the Schrödinger equation for many-body electrons can be calculated as:

$$H\left|\psi\right\rangle_e = E\left|\psi\right\rangle_e \tag{2.6}$$

The physics of Born-Oppenheimer approximation can be explained by the fact that electrons move much faster than nuclei, and thus electrons can adapt the movements of nuclei instantaneously. For every snapshot of the system, the nuclei can be viewed as stationary. The Born-Oppenheimer approximation is valid when temperatures are not very high.

If not specified otherwise, $|\psi\rangle$ refers to $|\psi\rangle_e$ in the following contents.

2.2.2 Hohenberg-Kohn Theorems

With the Born-Oppenheimer approximation, it is possible to separate the movements of electrons from nuclei. However, the exact solution of Eq. 2.6 is still very hard. The Hohenberg-Kohn theorems [32] provide the fundamental theoretical basis for the density functional theory by stating that:

1. For any system of interacting particles in an external potential $V_{ext}(r)$, the potential $V_{ext}(r)$ is determined uniquely, except for a constant, by the ground state particle density $n_0(r)$.

2. A universal functional for the energy $E[n]$ in terms of the density $n(r)$ can be defined, valid for any external potential $V_{ext}(r)$. For any particular $V_{ext}(r)$, the exact ground state energy of the system is the global minimum value of this functional, and the density $n(r)$ that minimizes the functional is the exact ground

state energy $n_0(r)$.

Although the functional $E[n]$ is sufficient to determine the exact ground state, its exact form is unknown.

2.2.3 The Kohn-Sham *Ansatz* and the Kohn-Sham Equations

The original many-body problem is further simplified by the Kohn-Sham *ansatz* [33], which states that:

1. The exact ground state density can be represented by the ground state density of an auxiliary system of non-interacting particles.

2. The auxiliary Hamiltonian is chosen to have the usual kinetic operator and an effective local potential $V^{\sigma}_{eff}(r)$ acting on an electron of spin σ at point r.

The importance of the Kohn-Sham *ansatz* lies in that it reduces the original many-body interacting system to auxiliary independent-particle equations by assuming that the ground state density of the original interacting system is equal to that of some chosen non-interacting system, with all the difficult many-body terms incorporated into an exchange-correlation functional of the density.

The auxiliary independent-particle Hamiltonian is:

$$H^{\sigma}_{aux} = -\frac{1}{2}\nabla^2 + V^{\sigma}(r) \tag{2.7}$$

And the Hohenberg-Kohn expression for energy is rewritten as:

$$E_{KS} = T_S[n] + \int \mathrm{d}r V_{ext} n(r) + E_{Hartree}[n] + E_{II} + E_{XC}[n] \tag{2.8}$$

where $n(r) = \sum_\sigma \sum_{i=1}^{N^\sigma} |\psi_i^\sigma(r)|^2$ is the electron density, $E_{Hartree}[n] = \frac{1}{2}\int \mathrm{d}^3r\mathrm{d}^3r' \frac{n(r)n'(r)}{|r-r'|}$ is the Hartree energy representing the classical long-range Coulomb interaction energy, $T_S[n] = \frac{1}{2}\sum_\sigma \sum_{i=1}^{N^\sigma} |\nabla\psi_i^\sigma|^2$ is the independent-particle kinetic energy, and $E_{XC}[n]$ are many-body effects, namely exchange and correlation. By giving an accurate $E_{XC}[n]$, Eq. 2.8 can be solved accurately and accurate ground-state properties can be calculated.

The solution of the Kohn-Sham auxiliary system can be obtained by minimizing the E_{KS} with respect to $n(r)/\psi_i^\sigma(r)$:

$$\frac{\delta E_{KS}}{\delta\psi_i^{\sigma *}(r)} = \frac{\delta T_S}{\delta\psi_i^{\sigma *}(r)} + \left[\frac{\delta E_{ext}}{\delta n(r,\sigma)} + \frac{\delta E_{Hartree}}{\delta n(r,\sigma)} + \frac{\delta E_{XC}}{\delta n(r,\sigma)}\right]\frac{\delta n(r,\sigma)}{\delta\psi_i^{\sigma *}(r)} = 0 \tag{2.9}$$

With the orthonormalization constraints,

$$\left\langle \psi_i^\sigma \middle| \psi_j^{\sigma'} \right\rangle = \delta_{i,j}\delta_{\sigma,\sigma'} \tag{2.10}$$

one can derive the well-known Kohn-Sham equations:

$$(H_{KS}^\sigma - \epsilon_i^\sigma)\psi_i^\sigma(r) = 0 \tag{2.11}$$

where the ϵ_i are the eigenvalues, and H_{KS}^σ is the effective Hamiltonian $H_{KS}^\sigma = -\frac{1}{2}\nabla^2 + V_{KS}^\sigma(r)$ with

$$V_{KS}^\sigma(r) = V_{ext}(r) + \frac{\delta E_{Hartree}}{\delta n(r,\sigma)} + \frac{\delta E_{XC}}{\delta n(r,\sigma)} = V_{ext}(r) + V_{Hartree}(r) + V_{XC}^\sigma(r) \tag{2.12}$$

2.2.4 Exchange-Correlation Functional

The Kohn-Sham *ansatz* states that by explicitly separating out the effects of independent-particle kinetic energy and the long-range Hartree terms, the remaining exchange-correlation functional can be reasonably approximated as a local or nearly local functional of the density. The exchange-correlation functional includes two parts:

$$E_{XC}[n] = E_X[n] + E_C[n] \tag{2.13}$$

where $E_X[n]$ denotes the exchange effects arising from the Pauli exclusion of electrons with the same spins, and $E_C[n]$ represents correlation effects due to electrons with different spins. Both attain non-positive values.

A number of methods have been proposed to approximate the exchange-correlation functional. Here we only briefly introduce two of them, LDA and GGA.

2.2.4.1 Local Density Approximation

The local density approximation (LDA) method [34, 35] treats the electron gas in the homogeneous electron gas (HEG) approximation, and thus the XC can be parameterized as:

$$E_{XC}[n] = \int \mathrm{d}^3 r n(r) \epsilon_{XC}^{HEG}(n(r)) \tag{2.14}$$

where $\epsilon_{XC}^{HEG}(n(r))$ is the exchange and correlation energy density of a HEG of constant density $n = n(r)$. The LDA should only work for systems of slowly varying densities like metals. However, it turns out that it works better than it should be. Local spin density approximation (LSDA), is a more general form of LDA with considerations of the spin effects of electrons.

2.2.4.2 Generalized Gradient Approximation

Compared to only local density is considered in LDA, the generalized gradient approximation (GGA) also takes the gradient of density into consideration:

$$E_{XC}[n] = \int \mathrm{d}^3 r n(r) \epsilon_{XC}(n, |\nabla n|) \tag{2.15}$$

In this dissertation, we mainly use the GGA proposed by Perdew, Burke and Enzerhof (PBE) [36]. PBE provides very good bond-lengths, vibrational frequencies, energy differences, and ionization potentials for most of the materials we studied.

2.2.5 Basis Sets

To numerically solve the Kohn-Sham equations, it is efficient to represent the electronic wavefunctions by a basis set in order to turn the partial differential equations into algebraic equations. In principle, these basis sets should obey some rules, like being complete. In practice, due to the consideration of speed and convergence, the basis set is chosen so that the errors introduced are small enough for the targeted properties.

2.2.5.1 Plane-wave Basis

One of the most commonly used bases in the solid-state community is the plane-wave basis, where the wavefunctions are represented by a linear combination of plane waves. The kinetic term can be written in an analytic form, and the Hartree potential can be calculated by fast Fourier transforms (FFTs). The expansion in plane-wave basis is

truncated at a cutoff energy:

$$\frac{\hbar^2}{2m_e}|G+K|^2 < E_{cutoff} \tag{2.16}$$

where G are the reciprocal lattice vectors. The error introduced by a finite basis set should always be carefully checked before production DFT calculations.

2.2.5.2 Real-space Basis

In real-space methods, the wavefunctions are represented by the Bloch waves and the phase factors due to the periodicity of the system. In our case, the wavefunctions are represented on 3D grids in real space [37, 38]. The advantages of this approach are that the potential operator is diagonal, and the Laplacian operator can be discretized at grid points using finite-difference formulas:

$$\nabla^2\psi(r_i) = \sum_j c_j\psi(r_j) \tag{2.17}$$

The cutoff of the basis set is controlled by the grid-spacing parameter $h = \frac{L}{N}$ ($L =$ length, $N =$ number of points). It controls the accuracy of the DFT calculations in the sense that a small h results in a dense grid, and thus a large basis set and high accuracy. A simple map between h and its equivalent kinetic energy cutoff comparable with E_{cutoff} in the plane-wave method is: $E^{rs}_{cutoff} = \pi^2/2h^2$ [38].

2.2.5.3 Atomic Basis Sets

The basis functions centered on the atoms are called "atomic orbitals". However, it is important to note that this does not imply that they are the actual solutions to the

electronic Schrödinger equation for the atom.

Atomic basis sets include Slater type orbitals, numerical atomic orbitals, Gaussian type orbitals (GTO), etc. Most of these orbitals are centered on atoms and localized around a region near the atoms. These kinds of basis sets have advantages; for example, two-center integrals and the kinetic energy term can be evaluated analytically in the basis of GTOs. The disadvantage of these kinds of basis sets is the control of accuracy. Unlike the plane-wave or real-space grids basis set, one cannot have a general single parameter determining the accuracy.

2.2.6 Pseudopotentials

In most of the properties we are interested in, the valance electrons play much more important roles than the core electrons because the core electrons' wavefunctions are highly localized around the nuclei and they do not interact with surrounding atoms. However, the valence electrons' wavefunctions need to be highly oscillatory in order to be orthogonal to the core electrons' wavefunctions. Taking into consideration that core electrons are chemically inert and strongly localized in the closed inner atomic shells, one can replace the all-electron potential with an appropriate pseudopotential so that the valence electrons have similar behaviors as in the all-electron calculations. In general, there are three types of pseudopotentials:

2.2.6.1 Norm-conserving Pseudopotentials

Several conditions need to be observed in building norm-conserving pseudopotentials (NCPPs) [39]:

1. Eigenvalues of valence electrons with the pseudopotentials must be the same as

those in all-electron calculations for a given atomic configuration.

2. Pseudo and all-electron wavefunctions agree beyond the core radius r_c.

3. Within the sphere ($r < r_c$), the charge densities from the pseudo wavefunctions must be the same as those from all-electron wavefunctions.

4. The pseudo wavefunctions and their first and second derivatives must be continuous.

Point 3 implies the name "norm-conserving". NCPPs usually have good "transferability", i.e., consistent performance in different environments. However, a high cutoff energy is usually necessary.

2.2.6.2 Ultrasoft Pseudopotentials

By giving up the norm-conserving constraint, the method proposed by Vanderbilt [40] requires a much smaller plane-wave cutoff and thus a much smaller number of plane-waves (thus the name "ultrasoft" pseudopotentials, USPPs). The valence electrons' wavefunctions are split into a smooth part, and an auxiliary part that varies rapidly within the core region:

$$\hat{V}_{US} = V_{loc}(r) + \sum_{nm} D_{nm} \left|\beta_n\right\rangle \left\langle\beta_m\right| \tag{2.18}$$

And the electron density with USPPs is:

$$n(r) = \sum_i \left[|\psi_i(r)|^2 + \sum_{nm,I} Q^I_{nm}(r) \left\langle \psi_i \middle| \beta^I_n \right\rangle \left\langle \beta^I_m \middle| \psi_i \right\rangle \right] \tag{2.19}$$

where the Q_{nm} ("augmentation charges") are:

$$Q_{nm}(r) = \psi_n^*(r)\psi_m(r) - \tilde{\psi}_n^*(r)\tilde{\psi}_m(r) \tag{2.20}$$

and

$$D_{nm} = B_{nm} + \epsilon_m q_{nm} \tag{2.21}$$

$$B_{nm} = \langle \psi_n | \chi_m \rangle \tag{2.22}$$

$$|\chi_n\rangle = (\epsilon_n - T - V_{loc}) |\psi_n\rangle \tag{2.23}$$

The constraint for the orthonormality condition of smooth wavefunctions is relaxed by introducing a generalized orthonormality through the overlap matrix S

$$\langle \psi_i | S | \psi_j \rangle = \delta_{ij} \tag{2.24}$$

where

$$S = 1 + \sum_{nm,I} q_{nm} \left| \beta_n^I \right\rangle \left\langle \beta_m^I \right| \tag{2.25}$$

Then, it can be proven that $|\psi\rangle$ are eigenvectors of the generalized eigenvalue problem:

$$[H - \epsilon_i S] |\psi_i\rangle = 0 \tag{2.26}$$

where

$$H = T + V_{eff} + \sum_{nm,I} D_{nm}^I \left| \beta_n^I \right\rangle \left\langle \beta_m^I \right| \tag{2.27}$$

All other properties can thus be calculated accordingly.

2.2.6.3 Projector Augmented Waves

Like USPPs, projector augmented waves (PAWs) [41, 42] introduce projectors and auxiliary localized functions. PAWs keep full all-electron wavefunctions. The smooth part of the wavefunction, which is referred to as $|\tilde{\psi}\rangle$, is related to the full all-electron wavefunction $|\psi\rangle$ by the transformation

$$|\psi\rangle = T\,|\tilde{\psi}\rangle \tag{2.28}$$

where T is known as the transformation operator. It is desired that T be unity only outside a sphere centered around an atomic nucleus such that $|\psi\rangle$ and $|\tilde{\psi}\rangle$ agree outside the atomic nucleus.

Within the spherical augmentation region around an atomic nucleus, we may expand the smooth wavefunction as

$$|\tilde{\psi}\rangle = \sum_i c_i\,|\tilde{\psi}_i\rangle \tag{2.29}$$

For a linear transformation operator T, the c_i correspond to projections within the augmented spherical region

$$c_i = p_i\,|\tilde{\psi}\rangle \tag{2.30}$$

where p_i are the required set of projection operators with the property

$$\langle p_i|\tilde{\psi}_j\rangle = \delta_{ij} \tag{2.31}$$

since the full all-electron wavefunction may be written as

$$|\psi\rangle = |\tilde{\psi}\rangle + \sum_i c_i(\psi_i - \tilde{\psi}_i) \tag{2.32}$$

we see that

$$T = 1 + \sum_i (\psi_i - \tilde{\psi}_i) p_i \tag{2.33}$$

2.2.7 Numerical Considerations

2.2.7.1 Workflow: Self-consistent Kohn-Sham Equations

The charge density can be obtained by numerically solving the Kohn-Sham Eq. 2.11, while the effective potential $V_{eff}(r)$ depends on the charge density. Therefore, one needs to solve the equations iteratively as shown in Fig. 2.1. Beginning with a trial charge density, effective potential $V_{eff}(r)$ and hence the Hamiltonian are formed. The new charge density is then obtained by solving the equations. The above procedure is repeated until the charge density and potential converge.

2.3 Real-Space Multi-Grid Method

Different from the plane-wave method, the real-space multi-grid method, which is developed by the Bernholc group [37, 38, 43], has two main techniques to solve the Kohn-Sham equations: real-space discretization of the Kohn-Sham equations, and the multi-grid algorithms to accelerate the convergence.

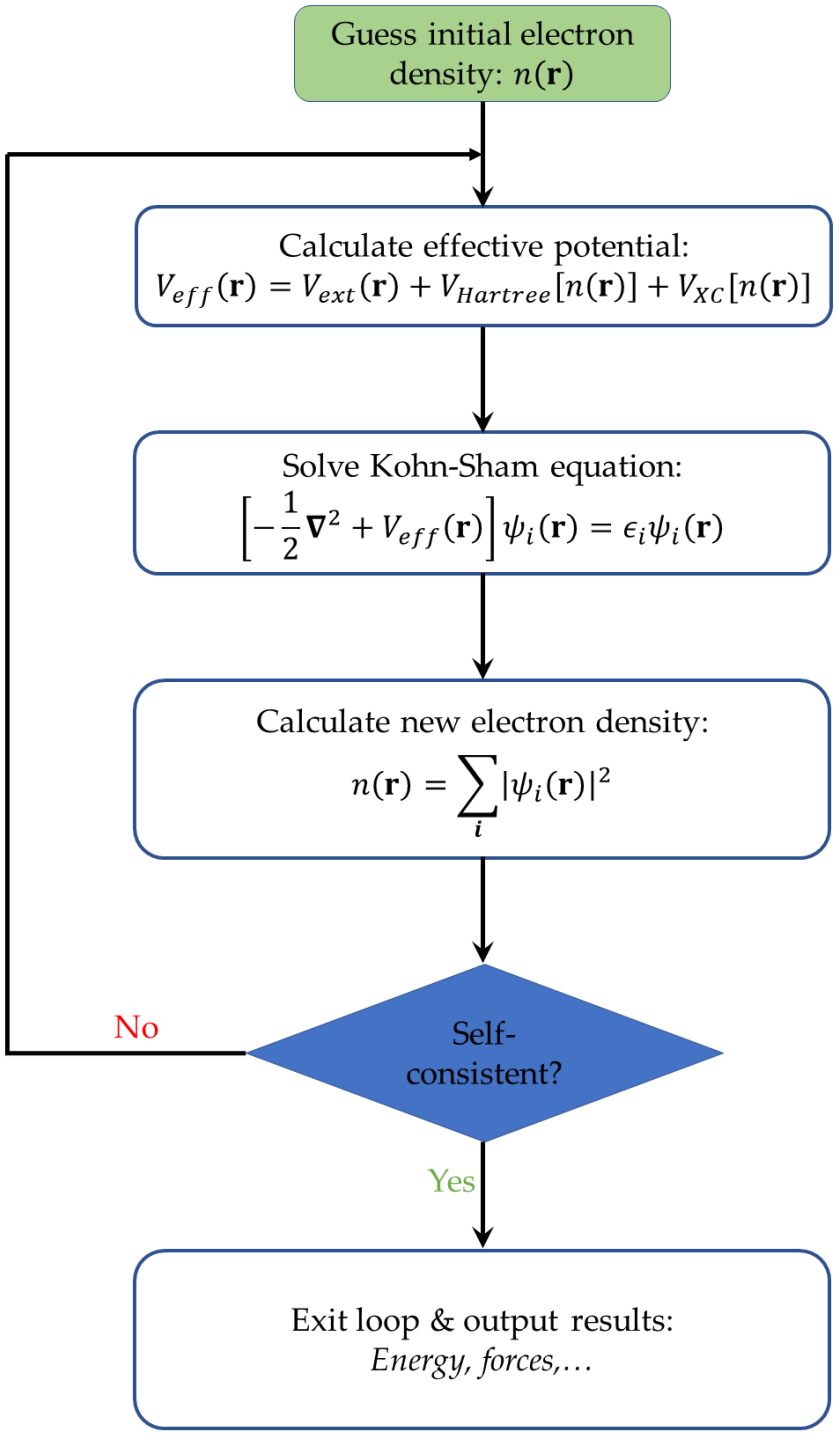

Figure 2.1 Typical workflow to computationally solve the Kohn-Sham equations self-consistently.

2.3.1 Real-space Kohn-Sham Equations

To begin with, it is helpful to introduce two main methods employed to numerically solve partial differential equations (PDE): finite difference method (FDM) and finite element method (FEM). The FDM approximates the differential equation by using finite differences to approximate the derivatives, while the latter approximates the solution of differential equations directly by subdividing a large system into smaller, simpler parts called finite elements. This work will focus on FDM as this is employed in the real-space multi-grid method.

Utilizing the FDM, the Kohn-Sham Eq. 2.11 is discretized in real-space, and the physical properties are represented on 3D grids:

$$\begin{gathered}(x_i, y_j, z_k) = (ih, jh, kh) \\ i = 1, \ldots, N_x, j = 1, \ldots, N_y, k = 1, \ldots, N_z\end{gathered} \tag{2.34}$$

Chelikowsky *et al*. [44] expand the kinetic energy Laplacian operator with the FDM on a real-space Cartesian grid with grid spacing h. At each direction at the grid point (x_i, y_j, z_k)

$$\left[\frac{\partial^2 \psi}{\partial x^2}\right]_{(x_i, y_j, z_k)} = \sum_{-m}^{m} c_m \psi(x_i + mh, y_j, z_k) + O(h^{2m+2}) \tag{2.35}$$

c_m is the coefficient for the FDM.

Since the set of grid points to map the above quantities is discrete, it can introduce spurious dependence of the Kohn-Sham eigenvalues, the total energy, and the ionic forces on the positions of ions with respect to the real-space grid. A set of techniques have been developed in order to overcome these difficulties and accurately calculate

the properties of large physical systems.

2.3.2 Algorithms and Implementations

2.3.2.1 Central Difference Scheme

One of the most common way to compute the numerical derivative of a function $f(x)$ at any point x_i is to approximate $f(x)$ by some polynomial function over the neighbors $x_j, j = 1, \ldots, N$ of x_i:

$$f(x_i) = \sum_{j=1}^{N} c_j f(x_j) \tag{2.36}$$

if the variations between neighboring points are sufficiently smooth.

N can vary per accuracy requirements on $f(x)$. If we sample $f(x)$ at the N (N is odd) equidistant points around x_i:

$$f_k = f(x_k), x_k = x_i + kh, k = -\frac{N-1}{2}, \ldots, \frac{N-1}{2} \tag{2.37}$$

where h is the spatial step. It can be proven that expressions of c_i can be obtained for any N. Formulas for larger numbers, e.g., $N = 5, 7, 9$, are listed in Tab. 2.1.

2.3.2.2 Multi-grid Algorithm

To numerically solve a discrete model problem in matrix form (discretized real-space Kohn-Sham equation), commonly used methods such as Gaussian elimination, Jacobi, Conjugate gradient are too slow, as they only reduce the components of error with wavelengths comparable to the grid spacing, but leave low-frequency components (long wavelength) undamped. The multigrid algorithm [38] accelerates convergence

Table 2.1 Central difference scheme coefficients

N	Expressions
5	$\frac{f_{-2}-8f_{-1}+8f_1-f_2}{12h}$
7	$\frac{-f_{-3}+9f_{-2}-45f_{-1}+45f_1-9f_2+f_3}{60h}$
9	$\frac{3f_{-4}-32f_{-3}+16f_{-2}-672f_{-1}+672f_1-168f_2+32f_3-3f_4}{840h}$

by employing a sequence of grids of varying resolutions. The long-wavelength errors from a fine grid will appear as high-frequency components at progressively larger grid spacing and thus attenuate rapidly on the coarser grids.

2.3.2.3 The RMG Code

The Real-space Multi-Grid based DFT code, RMG, has been implemented with the central differencing scheme and the multi-grid algorithm to solve the Kohn-Sham equations in real-space for electronic structure calculations. Benefiting from the inherent locality of the real-space method, RMG is effectively parallelizable and highly scalable by assigning specific regions of space to particular processors. Little communication is required, which is very suitable for large-scale first-principles calculations on advanced and very powerful modern supercomputers. Thus, RMG can be advantageous over other DFT codes in the phonon calculations, especially with the finite displacement method, in which supercells are usually built to obtain reliable results and the large system sizes can be challenging for other codes.

Features of the RMG code include but are not limited to:

1. Ground state calculations
2. Geometry optimizations
3. Molecular dynamics
4. Nudged elastic band calculations
5. Non-equilibrium Green's function (NEGF) calculations
6. Phonon calculations based on finite displacement method and the temperature-dependent effective potential method (interfaces with other packages)
7. GPU accelerated
8. Both USPPs and NCPPs are supported

2.4 Molecular Dynamics

As the name suggests, Molecular Dynamics (MD) is a technique to mimic atoms' behaviors in the real world using numerical methods, by dividing continuous real time into discrete time steps, and evolves the system in time using discretization of Newton's equations of motion for the atoms. Even though quantum theory may be necessary to treat a system in atomistic level, the classical method proves to be accurate enough in MD. Based on the method to calculate forces, MD is categorized into two types: classical MD which uses force fields or potentials to calculate interatomic forces, and *ab initio* MD (AIMD) which utilizes *ab initio* quantum mechanical methods to obtain forces. It should be noted that, though the forces are calculated by *ab initio* methods in AIMD, the atoms are moving along classical trajectories.

2.4.1 Classical MD

Classical MD uses simple interatomic potentials in analytical forms to calculate the forces:

$$F = -\nabla U \tag{2.38}$$

where U is the potential. The U function can be fitted from experimental values (such as LJ potentials), or in more complicated forms such as EAM [45], reactive force field [46] (ReaxFF) potentials, to describe complex systems better.

2.4.2 *Ab Initio* MD

2.4.2.1 Hellmann-Feynman Theorem

The Hellmann-Feynman theorem [47] is used to calculate the *ab initio* forces based on electronic wavefunctions. The theorem states that:

$$\frac{dE_\lambda}{d\lambda} = \langle \psi_\lambda | \frac{dH_\lambda}{d\lambda} | \psi_\lambda \rangle \tag{2.39}$$

where λ is a continuous parameter, H is a Hamiltonian operator, ψ is the ground-state wavefunction of the many-electron system, and E is the total energy of the state.

Ab initio forces can thus be derived:

$$F = -\frac{dE}{dr} = -\langle \psi_r | \frac{dH}{dr} | \psi_r \rangle \tag{2.40}$$

2.4.2.2 Car-Parinello MD and Born-Oppenheimer MD

The AIMD has two common types, Born-Oppenheimer MD (BOMD) and Car-Parrinello MD (CPMD) [48]. The BOMD is based on Born-Oppenheimer approximation, which means that electrons are fast degrees of freedom and can be adapted to the motions of nuclei instantaneously, and thus the nuclei are moving on a "Born-Oppenheimer surface". The motions of nuclei are calculated by the classical method (Newton's equations); however, it is time-consuming to compute the states (wavefunctions) of electrons for every MD step. For CPMD, instead of ignoring the freedom of electrons, it couples the electronic degrees of freedom into the classical coordinates system by assigning electrons a fictitious mass, and thus forms a system of coupled equations of motion for both ions and electrons. The CPMD method is computationally efficient and fast, but the accuracy of CPMD depends on the choice of the fictitious electron mass, and the system is not guaranteed to propagate along the real ground-state trajectory.

2.4.3 Ensembles

The standard MD simulation method (based on Newton's equations of motion) preserves the total energy and volume of the system during the evolution. If the total number of atoms N is also kept constant, then the MD simulations are said to be performed in the microcanonical (NVE) ensemble. For large NVE systems, the fluctuations of temperature are small, and it may be considered approximately constant. There are situations in which the temperature must be kept constant. When N, V and T are constant, the system is called a canonical (NVT) ensemble. Keeping NVT constant is not natural in standard MD simulations. Special control techniques,

such as the Andersen [49] or Nosé-Hoover [50, 51] thermostat methods, are needed to maintain the average temperature constant.

CHAPTER 3

THEORETICAL AND COMPUTATIONAL BACKGROUND: PHONONS

In this chapter, we review the theoretical and computational background that is used in this work, with a focus on phonon theory.

Often designated as quasi-particles, phonons are collective excitations of atoms in crystals or molecules with certain energy and momentum. The phonon theory originates in lattice dynamics, and has been used in other fields such as molecular dynamics simulations.

3.1 Classical Lattice Dynamics Theory

To describe the dynamics of lattices, one method is to derive the equations of motion for atomic vibrations by Hamiltonian mechanics, in which one needs to obtain expressions for the system's potential and kinetic energies. The kinetic energy can be written as $T = \sum_i \frac{P_i^2}{2m_i}$, while the potential energy needs to be derived.

Atoms in crystals at finite temperature are not fixed in space and keep vibrating around their equilibrium positions in a potential that can be Taylor expanded as:

$$V(r) = V(r_0) + \sum_i \Phi_i u_i + \sum_{i,j} \sum_{\alpha,\beta} \Phi_{i\alpha,j\beta} u_{i\alpha} u_{j\beta} + \dots \tag{3.1}$$

where α, β are directions, i, j are atom indices, Φ_i are the restoring forces and vanish at the equilibrium positions, and $\Phi_{i\alpha,j\beta} = \frac{\partial^2 V}{\partial u_{i\alpha} \partial u_{j\beta}}$ are the second-order interatomic force constants (IFCs). If the IFCs of a higher order than the second are assumed to be zero (the harmonic approximation), and we let $V(r_0) = 0$ at equilibrium, Eq. 3.1 can be written as:

$$V(r) = \sum_{i,j} \sum_{\alpha,\beta} \Phi_{i\alpha,j\beta} u_{i\alpha} u_{j\beta} \tag{3.2}$$

With the potential energy expressed as Eq. 3.2, the Hamiltonian can be written as:

$$H = T + V = \sum_{i\alpha} \frac{P_{i\alpha}^2}{2m_i} + \frac{1}{2} \sum_{i\alpha,j\beta} \Phi_{i\alpha,j\beta} u_{i\alpha} u_{j\beta} \tag{3.3}$$

Using the Hamilton's equations, we can eventually derive the vibrational equations of motion:

$$m_i \ddot{u}_{i\alpha} = -\sum_{j\beta} \Phi_{i\alpha,j\beta} u_{j\beta} \tag{3.4}$$

and the dynamical equations:

$$\sum_{j,\beta} D_{i\alpha,j\beta}(q) \epsilon_{j\beta}(q) = \omega(q)^2 \epsilon_{i\alpha}(q) \tag{3.5}$$

where $D_{i\alpha,j\beta}(q)$ is the dynamical matrix defined as:

$$D_{i\alpha,j\beta}(q) = \frac{1}{\sqrt{m_i m_j}} \sum_R \Phi_{i\alpha,(j+R)\beta} e^{-iq\cdot(R+r_i-r_j)} \tag{3.6}$$

The dynamical matrix is symmetric and Hermitian, thus the eigenvalues ω^2 are real. In principle, D should also be semi-positive definite. The eigenvectors of the dynamical equation, $\epsilon_{i\alpha}(q)$, are called phonon polarization vectors. It should be noted that ϵ are unitless ratios, and they are conventionally normalized as

$$\epsilon_{i\alpha}(q) = \frac{\sqrt{m_i} u_{i\alpha}(q)}{\sqrt{\sum_{j=1}^{N} \sum_\beta m_j u_{j\beta}(q)^2}} \tag{3.7}$$

to show the vibrational amplitudes of coordinate i, α at wave vector q.

In ionic crystals, long-range macroscopic electric fields arise that are associated with long wave longitudinal optical (LO) phonons. The long-range nature of the Coulomb

interaction at $q \to 0$ causes the difference between LO phonons and transverse optical (TO) phonons called TO-LO splitting, which can be corrected by the following formula [52]:

$$D_{i\alpha,j\beta}(q \to 0) = D_{i\alpha,j\beta}(q = 0) + \frac{1}{\sqrt{m_i m_j}} \left(\frac{4\pi}{\Omega_0}\right) \frac{\left[\sum_\gamma q_\gamma Z^*_{i,\gamma\alpha}\right] \left[\sum_{\gamma'} q_{\gamma'} Z^*_{j,\gamma'\beta}\right]}{\sum_{\alpha\beta} q_\alpha \epsilon^\infty_{\alpha\beta} q_\beta} \tag{3.8}$$

Here Ω_0 is the unit cell volume, ϵ^∞ is the high-frequency static dielectric tensor, and Z^* is the Born effective charge, which is the coefficient of proportionality between a change in macroscopic polarization and atomic displacements under zero external field.

To obtain Φ and D, there are two main methods, lattice dynamics methods which are discussed in 3.2, and MD methods which are discussed in 3.4.2.

3.2 Harmonic Phonon Theory

As shown in Eq. 3.2, in this case the Taylor expansion is truncated at the second order, which means that the potential profile is parabolic within small displacements, and all orders higher than the second are neglected. A schematic comparison of harmonic and anharmonic potential can be found in Fig. 3.1. In order for the harmonic approximation to be valid, it is also naturally assumed that there are no interactions between phonons and other excitaions (quasi-particles).

Generally, two methods have been proposed for the phonon calculations in the harmonic regime, the finite displacement method (FDM, not to be confused with the finite difference method discussed in section 2.3.1) and density functional perturbation theory (DFPT). FDM calculates force constants in real-space and uses Eq. 3.6 to obtain

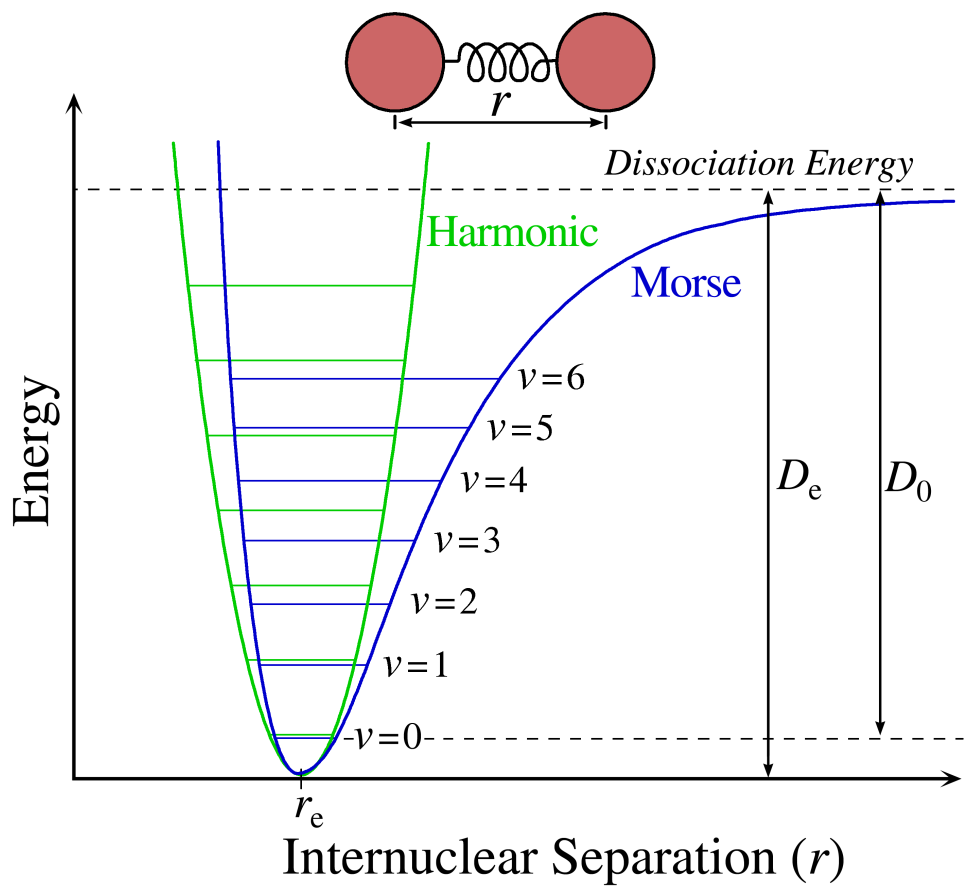

Figure 3.1 The harmonic & anharmonic potentials of an atom's vibration and its eigenvalues. Adapted from [53].

the dynamical matrix. Alternatively, DFPT, calculates the dynamical matrix directly in the reciprocal space. Both methods scale as $O(N^4)$, if we assume that DFT calculations scale as $O(N^3)$.

3.2.1 Implementation: FDM

In FDM, the force constant matrix is evaluated by numerically differentiating the forces on atoms with respect to small displacements (central differentials have been

applied to reduce the numerical errors):

$$\Phi_{i\alpha,j\beta} = \frac{\partial F_{j\beta}}{\partial u_{i\alpha}} = \frac{F_{j\beta}(r_{i\alpha} + u_{i\alpha}) - F_{j\beta}(r_{i\alpha} - u_{i\alpha})}{2u_{i\alpha}} + O(u_{i\alpha}^2) \tag{3.9}$$

where $F_{j\beta}$ is the force on atom j along the β direction after a small displacement $u_{i\alpha}$ of atom i, which can be accurately and easily calculated by the Hellmann-Feynman theorem. Alternatively, one may directly calculate force constants from the second derivatives of the potential energy, without calculating the forces explicitly. However, the energy-based method will require more computational cost as it needs more displacement configurations and higher accuracy in DFT calculations (due to the second derivatives) than the force-based method in Eq. 3.9.

3.2.2 Implementation: DFPT

DFPT, also called the linear response theory, is based on perturbation theory and provides an analytical formalism to calculate the second derivatives of the total energy with respect to the atomic coordinates. Two main formulations of DFPT are briefly introduced here.

3.2.2.1 Iterative formula based on the Green's function method

The iterative formula [54] is as follows:

$$\begin{aligned}
\frac{\partial E_{tot}}{\partial \lambda} &= \int \frac{\partial V_{loc}(r)}{\partial \lambda}\rho(r)d^3r + \frac{\partial U_{II}}{\partial \lambda} \rightarrow \\
\frac{\partial^2 E_{tot}}{\partial \mu \partial \lambda} &= \int \frac{\partial^2 V_{loc}(r)}{\partial \mu \partial \lambda}\rho(r)d^3r + \frac{\partial^2 U_{II}}{\partial \mu \partial \lambda} + \int \frac{\partial V_{loc}(r)}{\partial \lambda}\frac{\partial \rho(r)}{\partial \mu}d^3r \\
\frac{\partial \rho(r)}{\partial \mu} &= \sum_i \left(\frac{\partial \psi_i^*(r)}{\partial \mu}\psi_i(r) + \psi_i^* \frac{\partial \psi_i(r)}{\partial \mu} \right)
\end{aligned} \tag{3.10}$$

In the second equation in Eq. 3.10, the first term can be readily computed with numerical integration, and the second term involves only nuclei-nuclei interaction that is independent of the electronic states. Hence the third term is the most challenging one due to the response of the electron density with respect to the perturbation of atomic positions.

The wavefunctions obey the following equation:

$$[-\frac{1}{2}\nabla^2 + V_{KS}(r)]\psi_i(r) = \epsilon_i\psi_i(r) \tag{3.11}$$

where $V_{KS} = V_{loc}(r) + V_{Hartree}(r) + V_{XC}(r)$. We can expand these quantities in Taylor series:

$$\begin{aligned} V_{KS}(r,\mu) &= V_{KS}(r,\mu=0) + \mu\frac{\partial V_{KS}(r)}{\partial\mu} + \dots \\ \psi_i(r,\mu) &= \psi_i(r,\mu=0) + \mu\frac{\partial\psi_i(r)}{\partial\mu} + \dots \\ \epsilon_i(\mu) &= \epsilon_i(\mu=0) + \mu\frac{\partial\epsilon_i}{\partial\mu} + \dots \end{aligned} \tag{3.12}$$

Inserting these equations and keeping only the first order in μ we obtain:

$$[-\frac{1}{2}\nabla^2 + V_{KS}(r) - \epsilon_i]\frac{\partial\psi_i(r)}{\partial\mu} = -\frac{\partial V_{KS}(r)}{\partial\mu}\psi_i(r) + \frac{\partial\epsilon_i}{\partial\mu}\psi_i(r) \tag{3.13}$$

where $\frac{\partial V_{KS}}{\partial\mu} = \frac{\partial V_{loc}}{\partial\mu} + \frac{\partial V_{Hartree}}{\partial\mu} + \frac{\partial V_{XC}}{\partial\mu}$, and

$$\begin{aligned} \frac{\partial V_{Hartree}}{\partial\mu} &= \int \frac{1}{|r-r'|}\frac{\partial\rho(r')}{\partial\mu}d^3r' \\ \frac{\partial V_{XC}}{\partial\mu} &= \frac{dV_{XC}}{d\rho}\frac{\partial\rho(r)}{\partial\mu} \end{aligned} \tag{3.14}$$

depends self-consistently on the charge density induced by the perturbation. The

induced charge density depends only on $P_c \frac{\partial \psi_i}{\partial \mu}$ where $P_c = 1 - P_v$ is the projector on the conduction bands and $P_v = \sum_i |\psi_i\rangle \langle \psi_i|$ is the projector on the valence bands. In fact,

$$\begin{aligned}
\frac{\partial \rho(r)}{\partial \mu} &= \sum_i P_c \frac{\partial \psi_i^*(r)}{\partial \mu} \psi_i(r) + \psi_i(r)^* P_c \frac{\partial \psi_i(r)}{\partial \mu} \\
&+ \sum_i P_v \frac{\partial \psi_i^*(r)}{\partial \mu} \psi_i(r) + \psi_i(r)^* P_v \frac{\partial \psi_i(r)}{\partial \mu} \\
\frac{\partial \rho(r)}{\partial \mu} &= \sum_i P_c \frac{\partial \psi_i^*(r)}{\partial \mu} \psi_i(r) + \psi_i(r)^* P_c \frac{\partial \psi_i(r)}{\partial \mu} \\
&+ \sum_{ij} \psi_j^*(r) \psi_i(r) \left(\left\langle \frac{\partial \psi_i}{\partial \mu} \middle| \psi_j \right\rangle + \left\langle \psi_i \middle| \frac{\partial \psi_j}{\partial \mu} \right\rangle \right)
\end{aligned} \tag{3.15}$$

Therefore we can solve the self-consistent linear system:

$$[-\frac{1}{2}\nabla^2 + V_{KS}(r) - \epsilon_i] P_c \frac{\partial \psi_i(r)}{\partial \mu} = -P_c \frac{\partial V_{KS}(r)}{\partial \mu} \psi_i(r) \tag{3.16}$$

where

$$\frac{\partial \rho(r)}{\partial \mu} = \sum_i P_c \frac{\partial \psi_i^*(r)}{\partial \mu} \psi_i(r) + \psi_i(r)^* P_c \frac{\partial \psi_i(r)}{\partial \mu} \tag{3.17}$$

3.2.2.2 Variational formula based on the $(2n+1)$ theorem

The variational DFPT formula is based on the $(2n+1)$ theorem, which states that the $(2n+1)th$ derivative of the eigenenergy of a Hamiltonian may be determined with only a knowledge of the change in the eigenfunctions up to order n. Thus, the force constants, a.k.a., the second-order change in energy depends on the first-order change in the electron density. In analogy to the fact that DFT equations can be solved by minimizing the total energy, the DFPT problem can be solved by minimizing the second-order perturbation in the total energy, which gives the first-order changes in density, wavefunctions and potential [55, 56].

The electronic second-order energy, which is minimized in this approach, is:

$$E^{(2)} = \sum_{k,n} \left[\left\langle \phi_{k,n}^{(1)} \middle| H^{(0)} - \epsilon_{k,n}^{(0)} \middle| \phi_{k,n}^{(1)} \right\rangle + \left\langle \phi_{k,n}^{(1)} \middle| V^{(1)} \middle| \phi_{k,n}^{(0)} \right\rangle + \left\langle \phi_{k,n}^{(0)} \middle| V^{(1)} \middle| \phi_{k,n}^{(1)} \right\rangle \right] + \frac{1}{2} \int \frac{\delta^2 E_{XC}}{\delta n(r) \delta n(r')} n^{(1)}(r) n^{(1)}(r') + \sum_{k,n} \left\langle \phi_{k,n}^{(0)} \middle| V^{(2)} \middle| \phi_{k,n}^{(0)} \right\rangle \tag{3.18}$$

where the superscripts refer to the ground state (0), 1st and 2nd order changes, respectively. The dynamical matrix for a given q is then evaluated from the converged 1st order wavefunctions and densities.

3.2.3 FDM & DFPT: Connections and Differences

Both FDM and DFPT lead to the same solution. The advantage of the DFPT formalism is that the force constants matrix at a specific wave vector can be obtained through calculations that only use the primary unit cell. Therefore, this formalism is very efficient for systems with a small primary unit cell. For a large system, DFPT requires vast computational resources due to its scalability and inefficient parallelization. Another disadvantage of DFPT is that, for metallic systems, there are no clear-cut separations between the occupied and empty states unless the electronic temperature is zero, in which case the number of k points needed to correctly describe the effects of the Fermi surface would be very large. Special procedures must be used for metallic systems [57, 58]. This works mostly used FDM which will be discussed more in chapter 5.

3.3 Quasi-Harmonic Phonon Theory

The harmonic approximation is usually valid within small displacements, and may not be able to describe well phonon behavior at high temperatures. Also, the harmonic approximation assumes that the modes are vibrating independently and do not interact with each other, which can result in some unrealistic conclusions (such as no thermal expansion of solids, no dependencies of force constants on temperature or pressure, infinite phonon lifetime, no thermal equilibrium, etc.).

To overcome the limits of harmonic phonon theory's failure in explaining phonon's dependence on temperature (and volume), quasi-harmonic approximation (QHA) makes assumptions that phonons are dependent on crystal's volumes, but at a fixed volume, the harmonic approximation holds. QHA can be used to calculate volume-dependent thermal effects, such as thermal expansion.

3.3.1 Theory

The Helmholtz free energy at volume V and temperature T is given by the sum of the static energy and the vibrational term:

$$F(V,T) = E_{stat} + F_{vib}(\omega, T) \tag{3.19}$$

where E_{stat} is the energy from a static calculation and F_{vib} is the vibrational energy contributed by phonons:

$$F_{vib}(\omega, T) = \sum_{i=1}^{3N} \sum_{q} \left\{ \frac{1}{2}\hbar\omega_i(q) + k_B T \ln\left(1 - e^{\hbar\omega_i/k_B T}\right) \right\} \tag{3.20}$$

where $\omega_i(q)$ is the frequency of the normal mode i at each reciprocal space point q obtained from a lattice dynamics calculation with the harmonic approximation and T is the absolute temperature. In Eq. 3.20, the first term represents the zero-point energy at $T = 0$ and the second term arises due to the thermal excitation.

The Gibbs free energy is given by $G(P, T) = F(V, T) + PV$. Gibbs free energy is equal to the Helmholtz free energy at zero pressure, and, therefore, the equilibrium crystal structures at a given temperature T are obtained by minimizing the Helmholtz free energy with respect to the volume. The Gibbs free energy can best describe the first-order phase transitions in a system under constant pressure and temperature conditions.

3.3.2 Thermal Quantities

Some thermal quantities that can be derived with QHA are listed here:

1. The volumetric thermal expansion coefficient:

$$\alpha_V(T) = \frac{1}{V(T)} \left(\frac{\partial V(T)}{\partial T} \right)_P \tag{3.21}$$

2. The bulk modulus of the system:

$$K(T) = V(T) \left(\frac{\partial^2 F(V, T)}{\partial V^2} \right)_T \tag{3.22}$$

3. Grüneisen parameter:

$$\gamma_{qi} = - \left(\frac{\partial \ln \omega_i(q)}{\partial \ln V} \right)_{V=V_0} \tag{3.23}$$

where q is the phonon wave vector, and i is the band index.

4. The difference between constant-pressure and constant-volume specific heats:

$$C_P(T) - C_V(T) = \alpha_V^2(T)K(T)V(T)T \tag{3.24}$$

3.4 Anharmonic Phonon Theory

3.4.1 Phonon Scattering in Solids

3.4.1.1 Phonon Lifetime

The infinite phonon lifetime is only true under ideal conditions: perfect crystal and no phonon interactions with other (quasi-) particles. However, it is almost impossible for these conditions to be satisfied in the real world. The resultant finite phonon lifetime can be determined by using the Matthiessen's rule [59], assuming that only three mechanisms are contributing to phonon lifetime and they are independent:

$$\frac{1}{\tau} = \frac{1}{\tau_{electron}} + \frac{1}{\tau_{phonon}} + \frac{1}{\tau_{defect}} \tag{3.25}$$

where $\frac{1}{\tau}$ is the total scattering rate, $\frac{1}{\tau_{electron}}$ is the rate due to electron-phonon interactions, $\frac{1}{\tau_{phonon}}$ is from phonon-phonon interactions, and $\frac{1}{\tau_{defect}}$ is the scattering rate from defects.

Phonon linewidth, which is a property to describe the linewidth of phonon dispersion and thus the strength of anharmonicity, is related to the phonon lifetime by:

$$\Gamma(\omega) = \frac{1}{2\tau} \tag{3.26}$$

Phonon linewidth can also be experimentally measured by using neutron and

X-ray scattering techniques [60–62].

3.4.1.2 Electron-Phonon Interactions

With Born-Oppenheimer approximation made in DFT theory, one assumes that the motions of electrons and nuclei are nearly independent with small interactions, which can be treated as perturbations. The fundamental Hamiltonian for a system of nuclei and electrons can be written as:

$$H = H_n + H_e + H_{ep} \tag{3.27}$$

where H_{ep}, referred to as the electron-phonon interaction Hamiltonian, contains all the potential interaction terms involving the set of all-electron coordinates r (which include spins) and the set of all nuclear coordinates R.

Expanding the V_{KS} in Eq. 2.12,

$$\begin{aligned} V_{KS}(r) &= V_{ext}(r) + V_{Hartree}(r) + V_{XC}(r) \\ &= -\sum_I \frac{Z_I}{|r - R_I|} + \int \frac{n(r')dr'}{|r - r'|} + V_{XC}[n(r)] \end{aligned} \tag{3.28}$$

One can easily see that the Kohn-Sham SCF potential depends parametrically on the nuclear coordinates. Considering only one nucleus and one Cartesian direction (R with displacement u) for simplicity, the SCF potential can be expanded as:

$$V_{KS}(r, R) = V_{KS}(r, R_0) + \frac{\partial V_{KS}}{\partial R} u + \frac{1}{2} \frac{\partial^2 V_{KS}}{\partial R^2} u^2 + \dots \tag{3.29}$$

where the terms starting from the second one on the right-hand side lead to the H_{ep}. Subsequent expressions for energies, wavefunctions, and transition rates can be

derived using this expansion.

To quantitatively describes the probability of an electron scattered by a phonon, we define the electron-phonon matrix element, $g_\nu^{mn}(k,q)$, which can be expressed as:

$$g_\nu^{mn}(k,q) = \langle u_{m,k+q} | \Delta_{q,\nu} V_{KS} | u_{nk} \rangle = \left(\frac{\hbar}{2M\omega_{q\nu}} \right)^{1/2} \langle \psi_{m,k+q} | \frac{dV_{KS}}{du_{q\nu}} \cdot \hat{e}_{q\nu} | \psi_{n,k} \rangle \quad (3.30)$$

where M is the nucleus atomic mass, and q and k are wavevectors for the electron and the phonon, respectively. $\{m,n\}$, and ν are indexing the electronic bands and phonon modes, and $\omega_{q\nu}$ and $\hat{e}_{q\nu}$ are representing the eigenfrequencies and eigenvectors of the νth phonon modes at wavevector q. $\frac{dV_{KS}}{du_{q\nu}}$ describes the change of V_{KS} by the displacements $u_{q\nu}$ of nuclei.

The phonon linewidths can be obtained by integrating $g_\nu^{mn}(k,q)$ over the whole BZ:

$$\Gamma_{q\nu} = \frac{2\pi\omega_{q\nu}}{\Omega_{BZ}} \sum_{mn} \int d^3k |g_\nu^{mn}(k,q)|^2 \times \delta(\epsilon_{m,k+q} - \epsilon_F)\delta(\epsilon_{n,k} - \epsilon_F) \quad (3.31)$$

where $\epsilon_{n,k}$ is the Kohn-Sham energy at the given band index n and wavevector k, and ϵ_F is the Fermi energy.

The electron-phonon interactions lead to phonon-limited electron mobilities [63], phonon-assisted optical absorption [64], high-temperature superconductivity [65], etc. The conventional superconductivity is explained by the Cooper electron pair formation [66] due to electron-phonon coupling in the BCS theory [67]. Relevant properties such as the Eliashberg spectral function [68] and the resulting superconducting transition temperature [69] can also be derived.

3.4.1.3 Phonon-Phonon Interactions

The phonon-phonon interactions (PPIs) originate from the third- and higher-order terms in the Taylor expansion of the Hamiltonian [70]:

$$H = H_0 + I + H_2 + H_3 + \dots \tag{3.32}$$

with

$$\begin{aligned} I &= \frac{1}{2}\sum_{lk\alpha} m_k[\dot{u}_\alpha(lk)]^2 \\ H_2 &= \frac{1}{2}\sum_{lk\alpha}\sum_{l'k'\beta} \Phi_{\alpha\beta}(lk, l'k')u_\alpha(lk)u_\beta(l'k') \\ H_3 &= \frac{1}{6}\sum_{lk\alpha}\sum_{l'k'\beta}\sum_{l''k''\gamma} \Phi_{\alpha\beta\gamma}(lk, l'k', l''k'')u_\alpha(lk)u_\beta(l'k')u_\gamma(l''k'') \end{aligned} \tag{3.33}$$

where H_0, I, and H_n correspond to the constant potential, kinetic energy, and n-body crystal potential terms, respectively. $u(lk)$ is the atomic displacement of the kth atom in the lth unit cell, m_k is the mass of an atom of type k, and α, β and γ are the Cartesian directions. $\Phi_{\alpha\beta}$ and $\Phi_{\alpha\beta\gamma}$ denote the harmonic and cubic anharmonic force constants, respectively.

In the harmonic approximation phonon theory, there are no interactions of phonons, and in which case lattice waves can never equilibrate. With second quantization, the harmonic approximation only includes potential expansion up to the second-order and there are no cross-terms, while in higher-order expansions, cross terms will enable phonons to exchange energies with each other and equilibrate. The p-th order in Eq. 3.32 is representing a p-phonon process, and these are critical in thermal expansion in solids (when there are no thermal processes by electrons). Thermal transport in non-metal solids was usually considered to be governed by the three-phonon scattering

process, and the role of four-phonon and higher-order scattering processes is believed to be negligible.

For the three phonon process, the phonon linewidth can be written as:

$$\begin{aligned}\Gamma_\lambda(\omega) = \frac{18\pi}{\hbar^2} \sum_{\lambda',\lambda''} |\Phi_{-\lambda,\lambda',\lambda''}|^2 \{ & (n_{\lambda'} + n_{\lambda''} + 1)\delta(\omega - \omega_{\lambda'} - \omega_{\lambda''}) \\ & + (n_{\lambda'} - n_{\lambda''})[\delta(\omega + \omega_{\lambda'} - \omega_{\lambda''}) - \delta(\omega - \omega_{\lambda'} + \omega_{\lambda''})]\}\end{aligned} \tag{3.34}$$

where λ stands for (q, ν), and n_λ are the phonon occupations at the equilibrium,

$$n_\lambda = \frac{1}{\exp(\hbar\omega_\lambda / k_B T) - 1} \tag{3.35}$$

3.4.1.4 Phonon Scattering by Defects

In equilibrium, the atomic vibrations spread over most of the atoms in the system and the magnitude of the oscillation of any one atom is very small. When defects are present, they introduce vibrational modes that are distinct from bulk modes because they are spatially localized in the vicinity of the defect [71]; they involve oscillations of a small number of atoms in the immediate neighborhood of the defect. Light impurities produce high-frequency modes, while heavy impurities introduce low-frequency modes. Phonon scattering by defects dominates at low temperatures when the effects of PPIs decrease dramatically.

The defective crystals can be simulated by using the supercell method, but care must be taken regarding the supercell size and the distribution of the defects.

3.4.1.5 Other Phonon Scattering

In addition to the above mentioned scattering mechanisms, phonons can also be scattered by other (quasi-) particles/structures, like boundaries [72, 73], magnons [74, 75], isotopes [76, 77], dislocations [78, 79], etc.

3.4.2 Phonon Calculations from MD

The harmonic phonon theory (FDM and DFPT) can well describe phonon behaviors under harmonic and low-temperature conditions. At the same time, MD can simulate the evolution of a system at finite temperatures with phonon behaviors (including vibrations, couplings, and interactions with other particles, etc.) included incoherently. The following MD-based methods have been developed to explore temperature and anharmonic effects on phonons.

3.4.2.1 Phonon Power Spectrum

In MD simulations, atomic trajectories are generated from the classical equations of motions. Equilibrium properties are then estimated as time averages over the trajectories, which also contain information about the dynamics of the system, i.e., the phonon modes. In fact, the vibrational density of states, which exhibits peaks at the phonon frequencies, can in principle be computed by Fourier transforming the atomic velocity autocorrelation function (VACF) [30]:

$$g(\omega) = \int v(0) \cdot v(t) e^{-i\omega t} \tag{3.36}$$

One advantage of the phonon power spectrum is that no harmonic approximation is made, thus all anharmonic effects are included in the classical MD limit. However, it also suffers from three types of problems: 1) at low temperatures all the systems are harmonic and hence poorly ergodic; 2) the simulation time necessary to attain a frequency resolution of $\Delta\omega$ cannot be shorter than $\tau \sim 2\pi/\Delta\omega$, which is usually too long for AIMD simulations; 3) only phonon modes commensurate with supercell size can be accessed.

3.4.2.2 Green's Function-Based MD

Green's function-based molecular dynamics (GFMD) [23, 80, 81] is a method that can reduce the computational cost significantly while retaining numerical accuracy. It is based on the fluctuation-dissipation theorem [81], and takes the instantaneous positions of atoms in the equilibrated system and transforms them into reciprocal space to get the Green's function coefficients. After a certain number of measurements, the "time" average of the Green's function coefficients is evaluated and for a long enough simulation, it can be viewed as the "ensemble" average. The force constant matrices are then deduced, from which the dynamical matrices are constructed.

Considering an atom with mass m vibrating around its equilibrium position, and u being the displacement of the particle, we have:

$$\frac{1}{2}k\langle u^2\rangle = \frac{1}{2}m\langle v^2\rangle = \frac{1}{2}k_B T \tag{3.37}$$

where $\langle\rangle$ denotes the ensemble average, v is the velocity, and T is the temperature. We

can further derive that force constants can be determined by:

$$k = \frac{k_B T}{\langle u^2 \rangle} \tag{3.38}$$

This model is valid for real crystals with harmonic vibrations. However, it could still include anharmonic effects from finite temperature.

The Green's function defined by

$$G_{lk\alpha,l'k'\beta} = \langle u_{lk\alpha} u_{l'k'\beta} \rangle \tag{3.39}$$

is related to the force constant matrix as

$$G_{lk\alpha,l'k'\beta} = \frac{1}{k_B T} [\Phi^{-1}]_{lk\alpha,l'k'\beta} \tag{3.40}$$

i.e.,

$$\Phi = k_B T G^{-1} \tag{3.41}$$

It should be noted that, for crystals with Born-von Karman periodic conditions, it would be more convenient to assess the Green's function in reciprocal space rather than in real space [81].

In principle, the measurement can be carried out at any temperature under the melting point, as well as different pressures. It is therefore superior to the traditional lattice dynamics method which needs a quasi-harmonic procedure to take into account the temperature effect. Besides, with this method one does not need to work out the Hessian at all. Comparing to the method based on VACF, the GFMD method could yield directly the phonon dispersion in addition to the PDOS. Moreover, one does not

need to store a long trajectory so as to evaluate the time autocorrelations.

3.4.2.3 Temperature-Dependent Effective Potential Method

The temperature-dependent effective potential method (TDEP) [22, 82, 83] takes the effects of finite temperatures into accounts by fitting an effective potential function from a set of displacement-force pairs, instead of calculating IFCs by central-differencing potentials as in the FDM method. The displacement-force dataset of long atomic trajectories usually come from long-enough MD simulations in NVT/NVE ensembles. Since there are no assumptions made on the potential profile, the anharmonic effects are included naturally.

In NVT/NVE ensembles, a sufficiently large supercell is built with an optimized structure and MD simulations are performed. The displacement-force dataset extracted from the MD trajectories is used to fit an effective force constants matrix $(\tilde{\Phi}, 3N \times 3N)$ by minimizing the sum of differences between the fitted $(\tilde{F}(m)\Phi, 1 \times 3N)$ and the real forces $(F(m), 1 \times 3N)$ for all displacement configurations M, where $U(m)(1 \times 3N)$ is the vector composed of the m-th atomic displacements:

$$\tilde{\Phi} = \arg \min_{\Phi} \sum_{m=1}^{M} ||U(m)\Phi - F(m)||^2 \tag{3.42}$$

The TDEP method provides a consistent way to extract the best possible harmonic- or higher-order-potential energy surface at finite temperatures. It is designed to work even for strongly anharmonic systems where the traditional quasiharmonic approximation fails, and for thermal physics calculations.

CHAPTER 4

INELASTIC NEUTRON SCATTERING

In this chapter, we focus on neutron scattering and provide background to theoretical treatment, simulations, and experimental techniques.

Table 4.1 Some physical properties of neutrons [85].

Property	Value
Mass	1.675×10^{-27} kg
Electric charge	0
Spin	$\frac{1}{2}$
Magnetic moment	$-9.6623647(23) \times 10^{-27}$ J/T

4.1 Introduction to Neutron Scattering

Neutron scattering is a prevalent technique to study the structure and dynamics of atoms in materials, along with other methods such as X-ray scattering [27], Raman spectroscopy [26], or infrared spectroscopy [25]. Some unique advantages of neutron scattering [84] include the facts that they are non-destructive, sensitive to light atoms, and not restricted by selection rules. A summary of neutrons' physical properties is provided in table 4.1.

Neutrons can be produced from neutron-rich nuclei such as W, U, or Hg, by using the following two methods:

1. Reactor sources: using thermal neutrons to induce fission in a critical mass of a large fissile atomic nucleus (such as U-233, U-235, Pu-239) to produce high-energy (fast, or hot) neutrons.

2. Spallation sources: releasing neutrons from the target element by bombardment with energetic protons.

In general, reactors produce continuous neutron beams and spallation sources produce beams that are pulsed between 10 Hz and 60 Hz [86]. The energy spectra of

neutrons produced by reactors and spallation sources are different, with spallation sources producing more high-energy neutrons. Neutrons from reactors and spallation sources must be moderated before being used for scattering experiments.

In an INS experiment, we observe how the strength of neutron scattering varies with the energy and momentum transfers. The energy range of interest for molecular vibration is typically between 16 and 4000 cm^{-1}.

4.2 Neutron Scattering: Theory and Simulations

4.2.1 Scattering Theory

Only basic nuclei scattering theory is introduced here, and a more detailed introduction can be found in [30, 85].

From the aspect of neutron energy transfer, there are mainly three types of neutron scattering: 1) Elastic neutron scattering, which has no energy transfer between neurons and samples. It is the most probable event with a very intense line in the spectra around 0. 2) Quasi-elastic neutron scattering (QENS), which has a relatively small energy transfer between neutrons and samples. QENS has been commonly used in studying solid-state diffusion, slow motions in crystals, etc. 3) Inelastic neutron scattering (INS), which has an energy transfer between the neutrons and the samples. This thesis will only involve INS.

From the aspect of the wave-particle duality, neutron scattering can be categorized into coherent and incoherent scattering. When interacting with a sample, the wave-like representation of the neutron will simultaneously be scattered by multiple atoms; those scattered neutrons will keep in-phase and the coherence of incident neutrons is

kept. The resulting interference effects can be experimentally observed by diffraction experiments. On the other hand, the particle representation of the neutron will interact with atoms separately, with random phases and the scattering intensity is effectively a sum of scattering intensities from each nucleus.

4.2.1.1 Scattering Cross Sections

Cross sections are the key concepts in scattering experiments. In a normal neutron experiment, a beam of monoenergetic neutrons falls on a sample and is scattered onto a detect. The neutrons may be scattered or absorbed by atoms, but here we only focus on the scattering process. The neutrons undergo transitions from the initial states to the final states. If the initial neutron has the momentum k_i and energy E_i, and the final states has the momentum k_f and energy E_f, the partial differential cross-section is defined by:

$$\frac{\mathrm{d}^2\sigma}{\mathrm{d}\Omega \mathrm{d}E} = \frac{N_0}{\Phi \mathrm{d}\Omega \mathrm{d}E} \tag{4.1}$$

where Φ is the flux of the incident neutrons, N_0 is the number of neutrons scattered per second into a small solid angle $\mathrm{d}\Omega$ in the direction θ, ϕ with final energy between E and $E + \mathrm{d}E$.

The total cross section can be divided into coherent and incoherent parts:

$$\sigma = \sigma_{coh} + \sigma_{inc} \tag{4.2}$$

in which $\sigma_{coh} = 4\pi(\bar{b})^2, \sigma_{inc} = 4\pi(\bar{b^2} - (\bar{b})^2)$, and b is the impact parameter (perpendicular offset of the trajectory of the incoming neutron).

By employing Fermi's golden rule (which describes the transition rate from one state to another) and the Fermi pseudopotential (which describes the short-ranged

interatomic scattering potential), one can obtain an analytical formula for the scattering cross-sections of crystals:

$$\frac{\mathrm{d}^2\sigma}{\mathrm{d}\Omega\mathrm{d}E} = \frac{k_f}{k_i}\frac{1}{2\pi\hbar}\sum_{j,j'} b_j b_{j'} \int_{-\infty}^{\infty} \langle \exp[-iQ\cdot R_{j'}(0)]\exp[iQ\cdot R_j(t)]\rangle \exp(-i\omega t)\mathrm{d}t \tag{4.3}$$

where

$$Q = k_i - k_f \tag{4.4}$$

is the momentum transfer to the sample, and

$$\hbar\omega = E_i - E_f \tag{4.5}$$

is the energy transfer to the sample. The coherent and incoherent parts can be written as:

$$\begin{aligned}\left(\frac{\mathrm{d}^2\sigma}{\mathrm{d}\Omega\mathrm{d}E}\right)_{coh} &= \frac{\sigma_{coh}}{4\pi}\frac{k_f}{k_i}\frac{1}{2\pi\hbar}\sum_{jj'}\int_{-\infty}^{\infty}\langle \exp[-iQ\cdot R_{j'}(0)]\exp[iQ\cdot R_j(t)]\rangle \exp(-i\omega t)\mathrm{d}t \\ \left(\frac{\mathrm{d}^2\sigma}{\mathrm{d}\Omega\mathrm{d}E}\right)_{inc} &= \frac{\sigma_{inc}}{4\pi}\frac{k_f}{k_i}\frac{1}{2\pi\hbar}\sum_{j}\int_{-\infty}^{\infty}\langle \exp[-iQ\cdot R_j(0)]\exp[iQ\cdot R_j(t)]\rangle \exp(-i\omega t)\mathrm{d}t\end{aligned} \tag{4.6}$$

4.2.1.2 Scattering Function

Though cross-sections are key concepts in scattering theory, in scattering experiments, a more convenient quantity which is directly related to the observed intensities, is the "scattering function":

$$\begin{aligned}S(Q,\omega)_{coh} &= \frac{4\pi}{\sigma_{coh}}\frac{k_i}{k_f}\left(\frac{\mathrm{d}^2\sigma}{\mathrm{d}\Omega\mathrm{d}E}\right)_{coh} \\ S(Q,\omega)_{inc} &= \frac{4\pi}{\sigma_{inc}}\frac{k_i}{k_f}\left(\frac{\mathrm{d}^2\sigma}{\mathrm{d}\Omega\mathrm{d}E}\right)_{inc}\end{aligned} \tag{4.7}$$

A different way to interpret S is to derive it from the time-dependent pair-correlation function $G(r,t)$ and the self time-dependent pair-correlation function $G_s(r,t)$,

$$\begin{aligned} S(Q,\omega)_{coh} &= \frac{1}{2\pi\hbar}\iint G(r,t)\exp(i(Qr-\omega t))\mathrm{d}r\mathrm{d}t \\ S(Q,\omega)_{inc} &= \frac{1}{2\pi\hbar}\iint G_s(r,t)\exp(i(Qr-\omega t))\mathrm{d}r\mathrm{d}t \end{aligned} \tag{4.8}$$

The scattering function refelcts the structures and dynamics of the sample.

4.2.2 Simulations: the OCLIMAX Software

The OCLIMAX code [84, 87] is a well-known program dedicated to neutron nuclei scattering simulation, which includes full calculations of INS spectra with coherent/incoherent effects and temperature dependence for various INS instruments and arbitrary trajectories in the momentum and energy (Q,ω) space. It also supports simulation of INS from single crystals and powder samples, calculations for combinations and overtones, and phonon wing calculations for single molecules. With phonon frequencies and polarization vectors calculated by DFT codes (RMG, VASP, etc.), OCLIMAX can compute the scattering function $S(Q,\omega)$ that can be directly compared with experimentally measured spectra.

It should be noted that in OCLIMAX, the higher-order excitations greater than the first (multi-phonon) are iteratively calculated by convolution:

$$S_n(\omega) = \int_{-\infty}^{\infty} S_1(\omega-\omega')S_{n-1}(\omega')\mathrm{d}\omega' \tag{4.9}$$

4.3 Neutron Spectrometers

The aim of neutron scattering experiments is to measure the scattering function $S(Q,\omega)$, which requires the knowledge of both momentum and energy transfers between the sample and neutrons defined in Eq. 4.4 and Eq. 4.5..

For INS spectroscopy, there are three main types of spectrometers in use: (i) triple axis, which directly probes the energy and momentum transfer by selecting the wavelengths of neutrons before and after hitting the sample, (ii) instruments that fix the final energy which are known as indirect geometry instruments, and (iii) those that fix the incident energy which are known as direct geometry instruments. The last two types are also known as Time-of-flight (TOF) spectrometers. Brief introduction will be given to the indirect geometry instrument used in this work, called VISION.

4.3.1 Indirect Geometry: VISION

Instruments that work with any fixed final energy are conventionally known as indirect geometry instruments. However, we shall limit our consideration to those spectrometers with low final energies. The incident neutron beam, however, is "white" which means it has neutrons of various wavelengths. A simple formula for the trajectory can be derived in the low final energy case.

Starting from Eq. 4.4, we have:

$$Q^2 = k_i^2 + k_f^2 - 2k_i k_f \cos\theta \tag{4.10}$$

where θ is the angle between k_i and k_f. In the limit $k_i \gg k_f$, Eq. 4.10 reduces to

$$Q^2 = k_i^2 \tag{4.11}$$

Thus

$$E = Q^2/2m = 16.7Q^2 \tag{4.12}$$

with energy in cm^{-1} and Q in Å^{-1}. A typical trajectory in (Q, ω) space is displayed in Fig. 4.1.

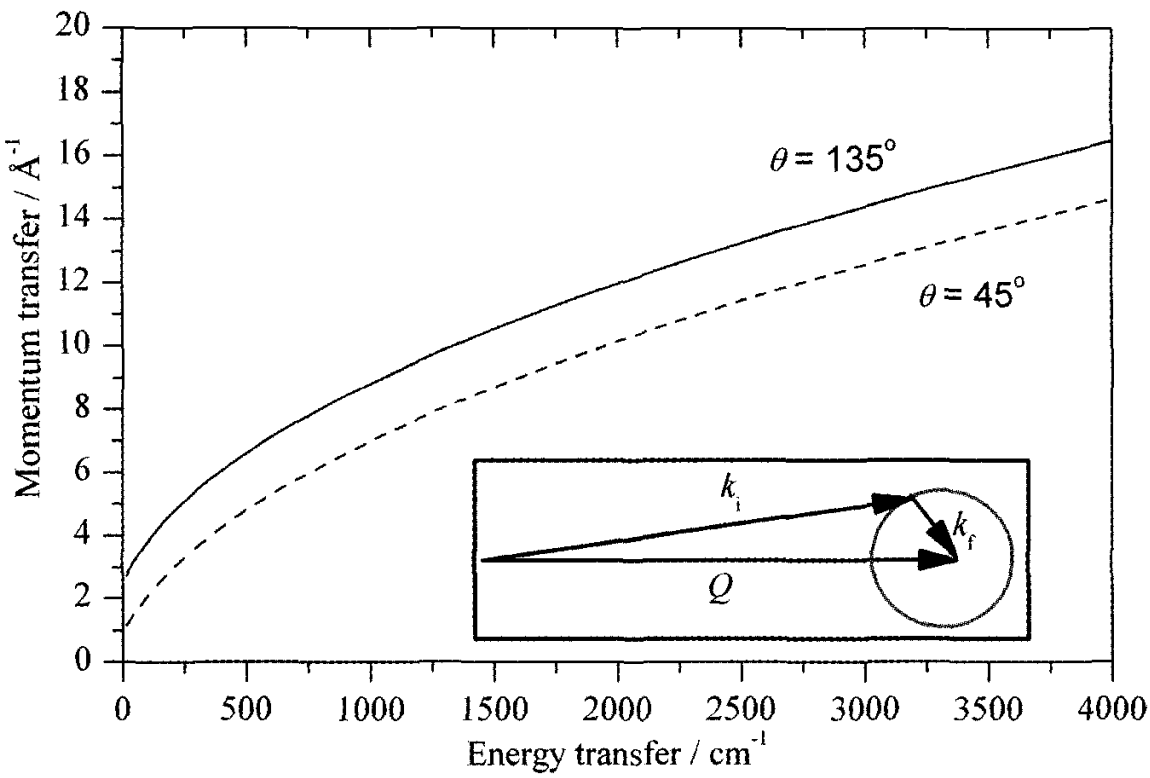

Figure 4.1 The trajectory map (Q, ω) of an INS spectrometer with a low fixed final energy for two scattering angles: 45 and 135. The inset shows the scattering triangle for the case where $k_i \gg k_f$. Adapted from [30].

The VISION spectrometer, located at Spallation Neutron Source, Oak Ridge National Laboratory, is the highest resolution broadband INS spectrometer in the world. It is also the world's first high-throughput INS instrument, with integrated modeling capability that helps to interpret the INS spectra. Its overall count rate in the inelastic signal is three orders of magnitude greater than that of similar spectrometers currently available. It measures vibrational spectra in a broad energy range (1 meV to 1000 meV). It records structural information using diffraction detectors in the backscattering position simultaneously with inelastic neutron scattering. The applications of VISION include studies on hydrogenous and non-hydrogenous materials, molecular vibrations and phonon density of states, crystalline and disordered materials, powders, nanomaterials, porous materials and surfaces (e.g., catalysis), etc.

CHAPTER 5

LARGE-SCALE PHONON CALCULATIONS USING THE REAL-SPACE MULTIGRID METHOD

In this chapter, we describe the methodology and implementation of phonon calculations for large-scale systems with the RMG code.

5.1 Abstract

Phonons are fundamental to understanding the dynamical and thermal properties of materials. However, first-principles phonon calculations are usually limited to moderate-size systems due to their high computational requirements. We implemented the finite displacement method (FDM) in the highly parallel real-space multigrid (RMG) suite of codes to study phonon properties. RMG scales from desktops to clusters and supercomputers containing thousands of nodes, fully supports graphics processing units (GPUs), including multiple GPUs per node, and is very suitable for large-scale electronic structure calculations. It is used as the core computational kernel to calculate the force constants matrix with FDM. By comparing with other widely used density functional theory packages and experimental data from inelastic neutron scattering, we demonstrate that RMG is very accurate in calculating forces at small displacements from equilibrium positions. The calculated phonon band structures and vibrational spectra for a variety of different systems are in very good agreement with plane-wave-based density functional theory codes, Quantum ESPRESSO, CASTEP and VASP, and these results have been validated comparing with inelastic neutron scattering experimental data measured at the VISION spectrometer at the Spallation Neutron Source.

5.2 Introduction

Vibrational spectroscopy and phonon band structures play central roles in studies of lattice dynamics and thermal conductivity [88], vibrational modes are routinely used as fingerprints of chemical species and configuration of adsorbed molecules in

solids, etc. In the past few decades, several different methods have been developed to perform phonon calculations, and they have achieved significant success. Due to the continuing development and implementation of theory for phonon calculations within the framework of density functional theory (DFT) as well as the fast development of highperformance computers, researchers are now able to calculate phonon band structures of many materials accurately, at an affordable computational cost and in a reasonable time. However, most procedures are only applicable to systems with a moderate number of atoms, due to the $O(N^4)$ scalability in the first-principles phonon calculations, where N is the number of atoms in the system.

In phonon calculations within DFT, the most challenging and time-consuming part is to build the force constant matrix accurately. There are two common schemes to calculate the force constant matrix. The linear response theory, also called density functional perturbation theory (DFPT) [20, 57], is one of the most popular methods. It provides an analytical formalism to calculate the second derivatives of total energy with respect to the atomic coordinates. The DFPT equations can be solved iteratively [57] or variationally [20]. Both methods lead to the same solution and have $O(N^4)$ scalability. The advantage of the DFPT formalism is that the force constant matrix at a specific wave vector can be obtained by calculations using only the primary unit cell. Therefore, this formalism is very efficient for systems with a small primary unit cell. For a large system, DFPT requires vast computational resources due to its scalability and inefficient parallelization.

Another scheme to calculate the force constant matrix is the finite displacement method (FDM), in which the force constant matrix is evaluated by numerically differentiating the Hellmann-Feynman forces on atoms. We will discuss this method in detail in Section 5.3. Although this method also scales as $O(N^4)$, its natural parallelization

over different displacement configurations makes it suitable for large systems. Since the force constants are calculated directly in real space, a supercell is needed when the primary unit cell is so small that the effects from periodic images cannot be neglected. Furthermore, the force constant matrix is only exact at the wave vectors that are commensurate with the supercell. In fact, the force constant matrix at other wave vectors is an interpolation from those at the commensurate wave vectors [89]. FDM is also straightforward to employ in any DFT code that can calculate the forces accurately. In this paper, we implement this method in our real-space multigrid (RMG) suite of DFT codes [38, 43]. RMG uses real-space meshes to represent the wave functions, the charge density, and the ionic pseudopotentials. The real-space formulation is advantageous for efficient parallelization via domain decomposition because each processor can be assigned a given region of space. The multigrid technique is used to accelerate the convergence by attenuating errors on successively coarser grids, at which even long-wavelength errors become oscillatory and, thus, are rapidly eliminated. RMG implements both norm-conserving and ultrasoft pseudopotentials [40]. RMG utilizes a mixed programming mode, using a message passing interface (MPI) for parallelization between nodes, while on-node parallelization is handled via OpenMP and C++11 threads. For Nvidia graphics processing unit (GPU) accelerators, Cuda-managed memory is employed for data transfer between central processing units and GPUs, while Cublas and Cusolver libraries are extensively used for GPU acceleration. Due to the extensive parallelization and excellent scaling, RMG is particularly suitable for very large electronic structure calculations and can handle several thousand atoms in a unit cell.

To validate the accuracy of RMG for phonon calculations, RMG results below are compared to those obtained using traditional plane-wave-based DFT codes, Quantum

ESPRESSO, VASP, and CASTEP. It is shown that all of the DFT codes generate very similar results that compare equally well with experimental data.

An open-source phonon package for pre- and post-processing of FDM calculations, Phonopy [88], is used to prepare the displacement configurations, extract the force constant matrix, and calculate the phonon properties for all codes except CASTEP.

Molecular dynamics (MD) can also be used to calculate the vibrational spectrum. The phonon density of states is given by the Fourier transform of the velocity-velocity autocorrelation function [30]

$$g(\omega) = \int_{-\infty}^{\infty} \boldsymbol{v}(0) \cdot \boldsymbol{v}(t) \exp(-i\omega t) \mathrm{d}t \tag{5.1}$$

Since the harmonic approximation is not employed, anharmonic effects are included in the classical molecular dynamics limit. The phonon dispersion can also be obtained from MD by evaluating the lattice Green's function from atomic displacements during the simulation [81]. Recently, MD was employed to study temperature effects on phonon spectra by the temperature-dependent effective potential method (TDEP) [22, 83]. Similarly to the FDM, TDEP requires MD to be performed in a supercell that is large enough to eliminate periodic image effects. It uses fitting and symmetry analysis to extract the force constant matrix and, optionally, anharmonic higher-order terms in free-energy expansion, from MD data. A disadvantage is that a long-time MD simulation is required to obtain a converged vibrational spectrum. ALAMODE [90] is an open-source package that implements the TDEP method and aims mainly at first-principles calculations for anharmonic systems and evaluation of thermal properties.

Turning to the experiment, vibrational properties can be obtained from diffuse

X-ray scattering [27], infrared spectroscopy [25], Raman spectroscopy [26], and inelastic neutron scattering (INS) [30, 31]. In this paper, we compare the calculated results to INS spectra [31] measured by the VISION spectrometer at the Spallation Neutron Source in the Oak Ridge National Laboratory (ORNL). Compared with other spectroscopy techniques, neutron scattering has advantages of wideband coverage of full phonon spectra with no selection rules to obey and the special capability of capturing hydrogen dynamics because of the proton's large cross-section for neutron scattering. INS spectra measure the intensity variation with energy and the momentum transfer between neutrons and phonons. The INS spectra usually focus on energy transfer. The theoretical intensity spectra can be computed by the OCLIMAX [84, 87] software based on vibrational modes obtained from the RMG or other codes.

5.3 Methodology

At a finite temperature, all atoms in a crystal or molecule vibrate with small displacements around their equilibrium positions. The system's total energy can be Taylor-expanded in terms of powers of the displacements. The linear term in the Taylor expansion is zero, because at equilibrium, the first derivatives of the total energy, i.e., the forces, are zero on all of the atoms. In the harmonic approximation, all of the powers of displacements larger than two are neglected, and the total energy can be written as

$$E_{tot}(r) = E_{tot}(r_0) + \frac{1}{2} \sum_{i\alpha,j\beta} \phi_{i\alpha,j\beta} u^{i\alpha} u^{j\beta} \tag{5.2}$$

where $u^{i\alpha}$ is the displacement of atom i along the α direction, $\phi_{i\alpha,j\beta}$ is the second derivative of the total energy with respect to atomic positions at equilibrium and is an

element of the force constant matrix. Eigenmodes of the dynamical matrix $D_{i\alpha,j\beta}(\boldsymbol{q})$ can be determined by solving the equation

$$\sum_{j,\beta} D_{i\alpha,j\beta}(\boldsymbol{q}) e_{j,\beta} = \omega^2(\boldsymbol{q}) e_{i,\alpha} \tag{5.3}$$

where ω is the frequencies and $e_{i,\alpha}$ is the components of the polarization vectors of phonons.

For a crystal with periodic boundary conditions, the dynamical matrix can be represented in the reciprocal space

$$D_{i\alpha,j\beta}(\boldsymbol{q}) = \frac{1}{\sqrt{m_i m_j}} \sum_R \phi_{i,\alpha,j+R,\beta} \exp[iq(R + r_i - r_j)] \tag{5.4}$$

where q is the wave vector in the first Brillouin zone, R is the lattice vector, and r_i and r_j are the atomic positions in the primitive cell.

If the system is in a stable state under the harmonic assumption, the force constant matrix is positive definite and the eigenvalues w_j^2 are positive. Eigenvalues with negative frequencies usually indicate that the system has not attained the state with the minimum energy, *i.e.*, the structure is dynamically unstable, and could further indicate the possibility of phase transition [88] or certain physical rules are not satisfied due to numerical errors (*e.g.*, the acoustic sum rule to be discussed below), or even that the harmonic approximation is not applicable, in which case the system can alternatively be analyzed using the MD method [91].

Focusing on the FDM, we evaluate the interatomic force constant by using the

following formula

$$\phi_{i\alpha,j\beta} = \frac{\partial^2 E}{\partial r_{i\alpha}\partial r_{j\beta}} = \frac{\partial F_{j\beta}}{\partial r_{i\alpha}} = \frac{F_{j\beta}(r_{i\alpha}+u_{i\alpha}) - F_{j\beta}(r_{i\alpha}-u_{i\alpha})}{2u_{i\alpha}} \tag{5.5}$$

where $F_{j\beta}$ is the force on atom j along the β direction after a small displacement $u_{i\alpha}$ of atom i, which can be accurately and easily calculated by the Hellmann-Feynman theorem as shown in Eq. 5.6, where $\hat{H}$ is the Hamiltonian operator and ψ is the wavefunction of H.

$$F_{j\beta} = -\frac{\partial E}{\partial u_{j\beta}} = -\langle\psi|\frac{\mathrm{d}\hat{H}}{\mathrm{d}u_{j\beta}}|\psi\rangle \tag{5.6}$$

Alternatively, one may directly calculate force constants from the second derivative of the total energy, without calculating forces explicitly. However, the energy-based method will require more computational cost as it needs more displacement configurations and higher accuracy in DFT calculations (due to the second derivatives) than the force-based method in Eq. 5.5.

The advantage of the FDM can be clearly seen from the above formula. Without a new algorithm, any DFT code can be used to calculate the force constant matrix by evaluating the forces at appropriate displacement configurations. In the real space, the interatomic force constants decay quickly to zero with distance. In our implementation, a force constant is set to zero when the distance between two atoms is larger than the cutoff radius R_C. R_C, thus, varies for different systems and also depends on the desired accuracy. For a system with periodic boundary conditions, the primitive unit cell may not be large enough to calculate all of the non-negligible force constants with a finite displacement configuration. In this case, one must choose a supercell, which will contain the sphere described by the cutoff radius.

For a system with a primitive unit cell containing N atoms, we need to calculate

forces in a supercell by perturbing each atom in the primitive unit cell. For each atom, two displacements are required to get accurate force constants. In total, $6N$ different displacement configurations need to be considered to extract the force constant matrix. The resulting matrix in the real space has dimensions $3N \times 3NM$, where M is the number of primitive unit cells in the supercell.

Symmetry operation can be used to reduce the number of displacement configurations. If the atoms i, j transform to their equivalent atoms is, js under a symmetry operation S, the force constants between these two pairs of atoms satisfy the following relation [92]

$$\Phi_{is,js} = S \cdot \Phi_{i,j} \cdot S^{-1} \tag{5.7}$$

Mathematically, the force constant matrix should satisfy two rules. The first is the symmetry of the matrix

$$\Phi_{i\alpha,j\beta} = \Phi_{j\beta,i\alpha} \tag{5.8}$$

because the second derivative operators commute in Eq. 5.5. The second is the acoustic sum rule (ASR)

$$\sum_{i,j} \Phi_{i\alpha,j\beta} = 0 \tag{5.9}$$

which is the result of translational invariance.

In calculations, the interatomic force constants are extracted from total energy and force calculations with different atomic displacements and are set to zero when the distance between two atoms is larger than the cutoff radius R_C. Therefore, these two rules are broken due to numerical errors. The symmetry rule can be restored by averaging the off-diagonal elements. The ASR can be imposed in three possible ways. The first one is to subtract the corresponding fraction of the sum residuals from the

diagonal elements $\Phi_{i\alpha,j\beta}$ only, the second one is to adjust each nonzero element by the same amount, and the third one is to adjust the nonzero elements proportionally to their magnitudes. We will use the first option because it usually outperforms the other two options [18]. When the ASR is imposed, the symmetry rule may be broken again. Therefore, we iteratively impose these two rules until both conditions are satisfied.

From Eq. 5.5, the most time-consuming parts of the FDM phonon calculations are the self-consistent calculations for all atomic displacement configurations. An interface code between Phonopy and RMG has been developed. The workflow is as follows. First, the atomic structure of the system is optimized with RMG using the primary unit cell. Second, a supercell is determined by the cutoff radius of the force constants. Phonopy is used to set up the displacement configurations by taking into consideration the crystal symmetry of the system. Third, the forces on atoms at each displacement configuration are calculated by RMG. Fourth, the force constant matrix is constructed by Phonopy and selfconsistently adjusted to satisfy the two rules discussed above. The phonon band structure and the vibrational spectrum are then calculated. For Quantum ESPRESSO and VASP, the interfaces to Phonopy already exist and have been used in the same workflow.

A different way to extract the force constant matrix is by performing long-enough MD simulations in NVT/NVE ensembles. The displacement-force dataset from the MD trajectories is used to extract the force constant matrix by the open-source package ALAMODE. The anharmonic effects can also be included if needed. We have also written an interface between ALAMODE and RMG. The workflow is the same as RMG-Phonopy's in the first step. Then, a sufficiently large supercell is built with the optimized structure and MD simulations are performed by RMG in NVT/NVE ensembles. The displacement-force dataset extracted from the MD trajectories is used

to fit the effective force constant matrix $(\tilde{\Phi}, 3N \times 3N)$ by ALAMODE via minimizing the sum of differences between the fitted $(\tilde{F}(m) = U(m)\Phi, 1 \times 3N)$ and the real forces $(F(m), 1 \times 3N)$ for all displacement configurations M [90], where $U(m)(1 \times 3N)$ is the vector composed of the mth atomic displacements

$$\tilde{\Phi} = argmin \sum_{m=1}^{M} ||U(m)\Phi - F(m)||^2 \tag{5.10}$$

5.4 Results and Discussion

Phonon calculations have been performed on four systems with increasingly larger unit cell sizes: silicon (Si), zirconium- (II) hydride (ZrH_2), carbazole ($C_{48}H_{36}N_4$), and zeolitic imidazolate frameworks (ZIF)-8 ($C_{96}H_{120}N_{48}Zn_{12}$). Since the force constants are calculated by finite displacements in our implementation, highly accurate total energy and force calculations need to be performed. To validate the accuracy of the RMG, the calculated phonon band structures and/or vibrational spectra are compared with the results obtained using other DFT packages, such as Quantum ESPRESSO (QE) [93], VASP [42, 94], and CASTEP [95]. Different from the RMG method, in which the wave functions are represented on a realspace grid, the other three packages use plane waves to represent the wave functions. In the examples discussed below, for all of the supercell calculations, the small displacements are set to 0.01 Å and only the Γ point is used for Brillouin sampling, because the supercell must be large enough to eliminate the periodic image effect in the force constants.

5.4.1 Silicon

Silicon crystallizes in the diamond structure and has very high symmetry. Its primary unit cell has only two atoms, and its physical properties are well known. Therefore, silicon is a very good candidate to benchmark the accuracy of phonon calculations with RMG. Here, we use a supercell consisting of $2 \times 2 \times 2$ cubic cells to perform the FDM calculations. Figure 5.1 shows the phonon band structures calculated with RMG-Phonopy and QE-Phonopy. The same norm-conserving pseudopotentials were used for both RMG and QE. The real-space grid spacing was 0.17 Å, and the planewave cutoff was 40.0 Ry. The perfect agreement between the two sets of results shows that the real-space method (RMG) performs as accurately as the plane-wave based method.

5.4.2 Zirconium(II) Hydride

Zirconium alloys with hydrogen are of great interest to researchers for their promising potential to store hydrogen atoms as well as their applications in nuclear reactors and neutron scattering science [96, 97]. Zirconium hydride has different crystalline phases depending on hydrogen concentration. At a very low hydrogen concentration, the most stable structure is the metallic phase α-Zirconium with the hcp structure. As the hydrogen concentration increases, its crystal structure transitions to the face-centered cubic (δ-Zr) and then the face-centered tetragonal (ϵ-Zr). Here, we focus on the high-concentration ϵ-Zr phase, ZrH_2, which contains the most H. It has the bodycentered tetragonal (bct) structure with the space group of I4/mmm and $c/a = 1.2639$.

The supercell for the displacement configurations contains $3 \times 3 \times 2$ primary unit cells and 108 atoms. The valence electron configuration of Zr was set to 5s4d.

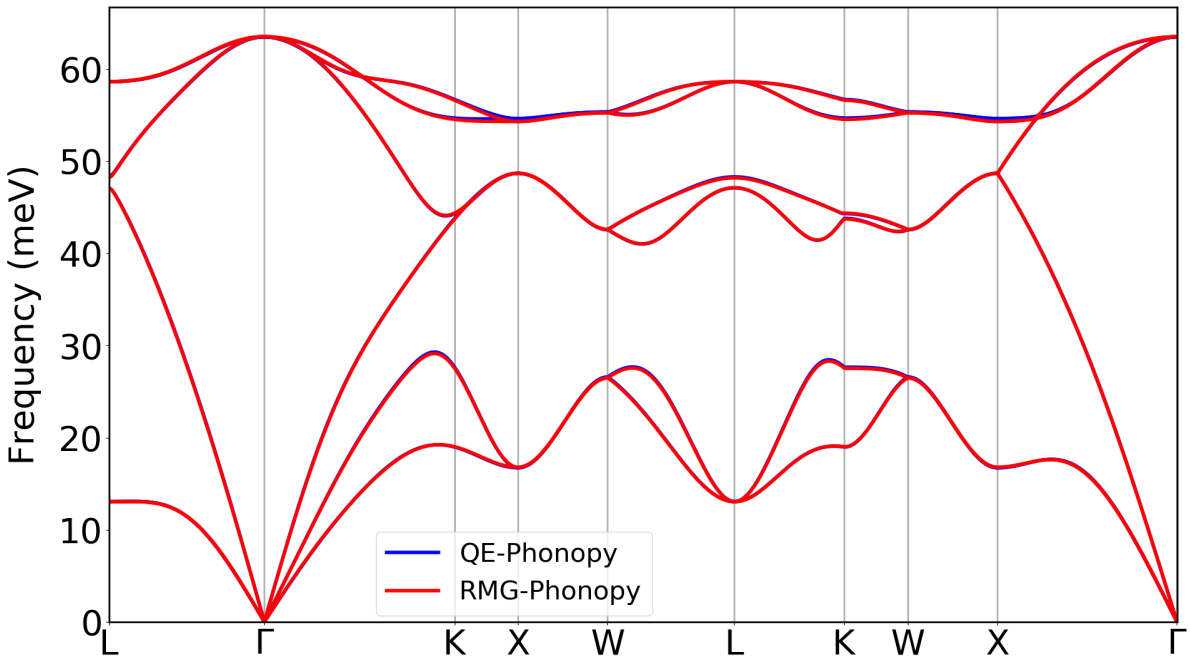

Figure 5.1 Phonon dispersions of crystalline silicon calculated by QE-Phonopy (blue) and RMG-Phonopy (red). The results are nearly identical, and the two curves fall on top of each other.

Figure 5.2 shows the phonon band structures calculated by RMG and QE, which are also in excellent agreement with each other. The grid spacing of 0.111 Å is used in RMG, and the plane-wave cutoff of 80 Ry for wave functions is used in QE.

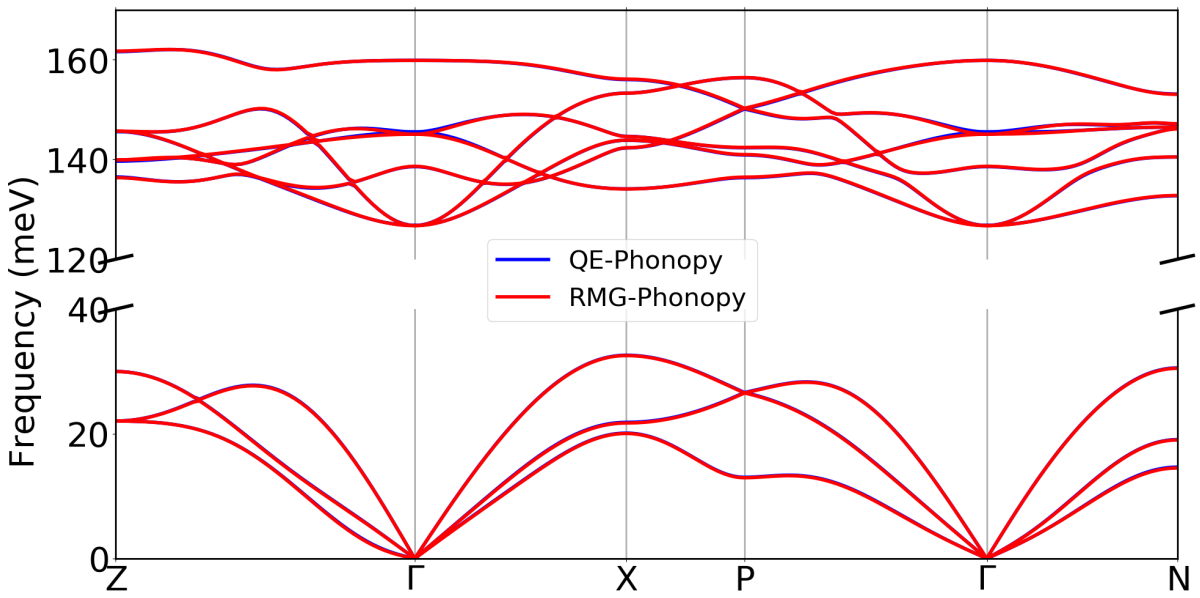

Figure 5.2 Phonon dispersions of ZrH_2 calculated by RMG-Phonopy (red) and QE-Phonopy (blue).

Figure 5.3 shows the calculated vibrational spectra compared to the results of neutron scattering experiments performed with VISION. The intensities from theory are normalized to the experimental spectrum. The FDM results from RMG and QE are very similar and agree equally well with the experimental data. The calculated one-phonon scattering spectra around 150 meV are in good agreement with the experimental data, while there are some discrepancies between the theory and experiment when two or more phonons are emitted. For the sharp peaks marked by arrows in the experimental data, the significantly decreasing interpeak spacing strongly suggests

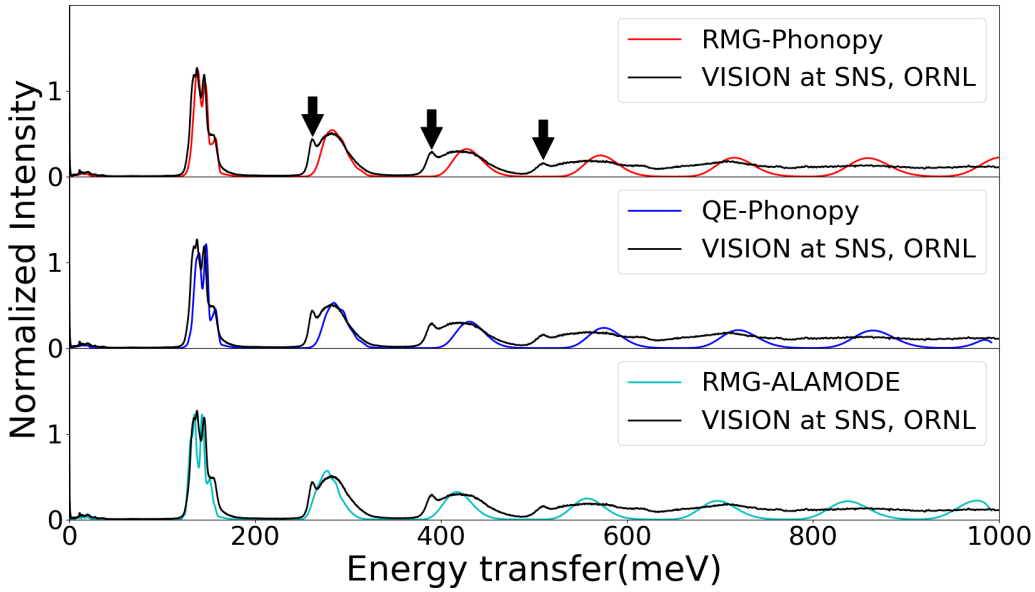

Figure 5.3 Vibrational spectra from RMG-Phonopy (red), QEPhonopy (blue), RMG-ALAMODE (cyan), and VISION's experimental data (black) at 5 K for ZrH_2. Overtone peaks, which correspond to multiple phonon scattering events, are generated by the convolution of the DFT-calculated fundamental peaks by the OCLIMAX software. The peaks below 200 meV are from onephonon scattering events, while those above 200 meV result from the scattering of two or more phonons. Extra sharp peaks marked by black arrows might be due to anharmonic effects.

anharmonic effects. Kolesnikov et al. attributed it to boundstate multiphonons [98]. Since our current calculations are based on the harmonic approximation, we are not able to include anharmonicity in the multiphonon scattering spectrum.

The bottom panel in Figure 5.3 shows the phonon spectrum computed from molecular dynamics using RMG and ALAMODE. There is a slight improvement over the RMG-Phonopy results, confirming that the extraction of force constants from molecular dynamics is practical for these systems. While thermal and anharmonic effects are quite small for these materials, the RMG-ALAMODE procedure can also be used for phases that would not be stable at 0 K and would, thus, exhibit negative

phonon modes if the FDM was used.

5.4.3 Carbazole

Carbazole is an aromatic heterocyclic organic compound. It consists of two six-membered benzene rings and one five-membered nitrogen-containing ring. Polycarbazole can potentially be used as a blue light emitter [99]. In crystalline carbazole, four carbazole molecules form an orthorhombic structure with lattice constants of $5.725 \times 7.772 \times 19.182$ Å^3.

In our calculations, the atomic structure is optimized using a Brillouin Zone sampling mesh of $3 \times 3 \times 1$, which reduces to four irreducible k-points. The maximum residual force is set to be 0.05 mHa/Bohr so that the force constants can be calculated accurately by FDM. The supercell for displacement configurations includes $3 \times 3 \times 1$ primitive unit cells with 792 atoms in total. The same norm-conserving pseudopotentials with the Perdew-Burke-Ernzerhof (PBE) exchange-correlation functional are used in QE and RMG, while projector-augmented waves [41, 42] and norm-conserving pseudopotentials are used in VASP and CASTEP, respectively. The grid spacing in RMG is 0.159 Å, while the plane-wave cutoffs are 40 Ry, 800 eV, and 800 eV in QE, VASP, and CASTEP, respectively.

In Figure 5.4, we show normalized intensity comparisons between different codes and VISION's measurements. Overall, there is a good agreement between all of the different codes and the experiment, although some discrepancies exist at various energy ranges. At 35 meV, VASP and CASTEP show one peak, while RMG and QE show two peaks with a small splitting. At 55 meV, the results from RMG and QE agree well with each other and also with VASP but have a few meV shift compared to the results from

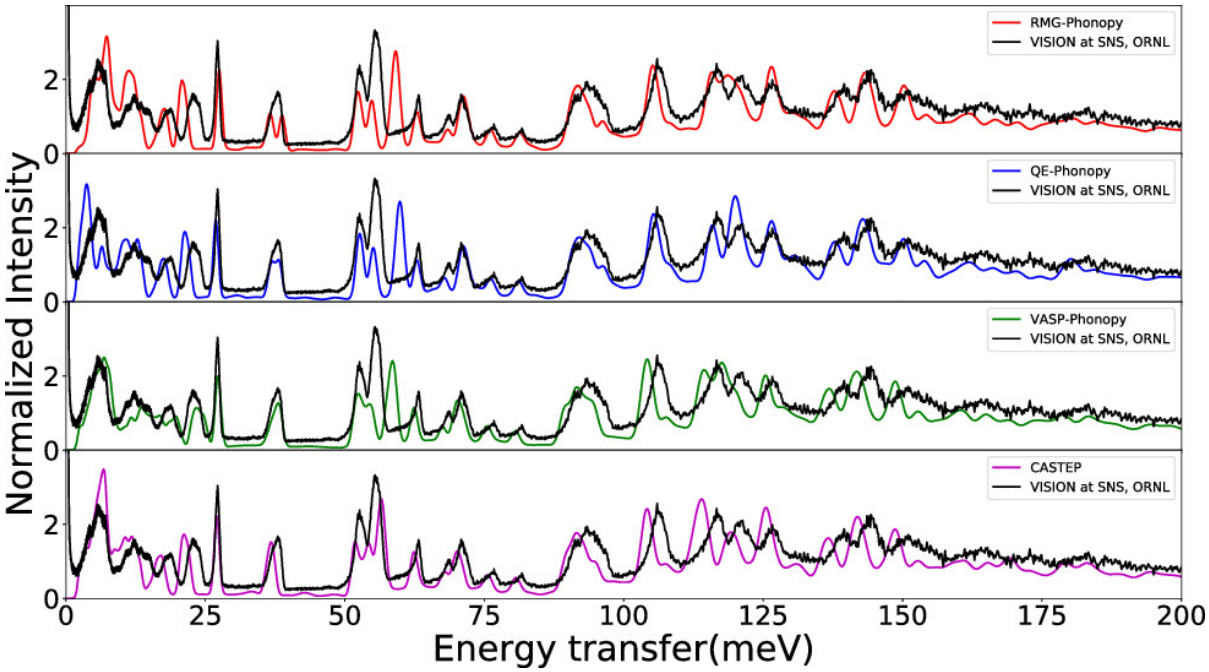

Figure 5.4 Normalized intensity comparisons between RMG-Phonopy (red), QE-Phonopy (blue), VASP-Phonopy (green), CASTEP (magenta), and experimental data (black) at 5 K for carbazole.

CASTEP. These subtle differences may result from different implementations used in different codes, e.g., in filtering pseudopotentials, the numerical approximations for the Laplacian and gradient operators, etc.

5.4.4 ZIF-8

Zeolitic imidazolate frameworks (ZIFs) are metal-organic frameworks that are topologically isomorphic with zeolites. They have wide-ranging applications in carbon capture due to their robust porosity, resistance to thermal changes, and chemical stability. Among all of the ZIFs, ZIF-8 ($C_{96}H_{120}N_{48}Zn_{12}$) has been further investigated for applications in supercapacitors and as a catalyst, e.g., to reduce CO_2 [100].

The crystal structure of the ZIF-8 is a simple cubic with I-43m space group symmetry. There are 276 atoms in the unit cell. The lattice constant is 16.992 Å and the Γ point is sufficient to sample the Brillouin Zone. For the scalarrelativistic Zn pseudopotential, 3d and 4s electrons were treated as valence. The PBE functional is used, and the forces are converged until the maximum residual force is smaller than 0.1 mHa/Bohr. The RMG grid spacing was 0.132 Å, and the plane-wave cutoffs were 80 Ry.

In Figure 5.5, the vibrational spectra calculated by RMG and QE are shown together with VISION's experimental results. The calculated spectra agree with each other very well except for discrepancies at very low energies. The simulated results are also in very good agreement with the experimental results.

5.5 Summary and Conclusions

In summary, we have shown that the open-source real-space multigrid (RMG) suite of codes can provide accurate total energies and forces that can be used to obtain phonon

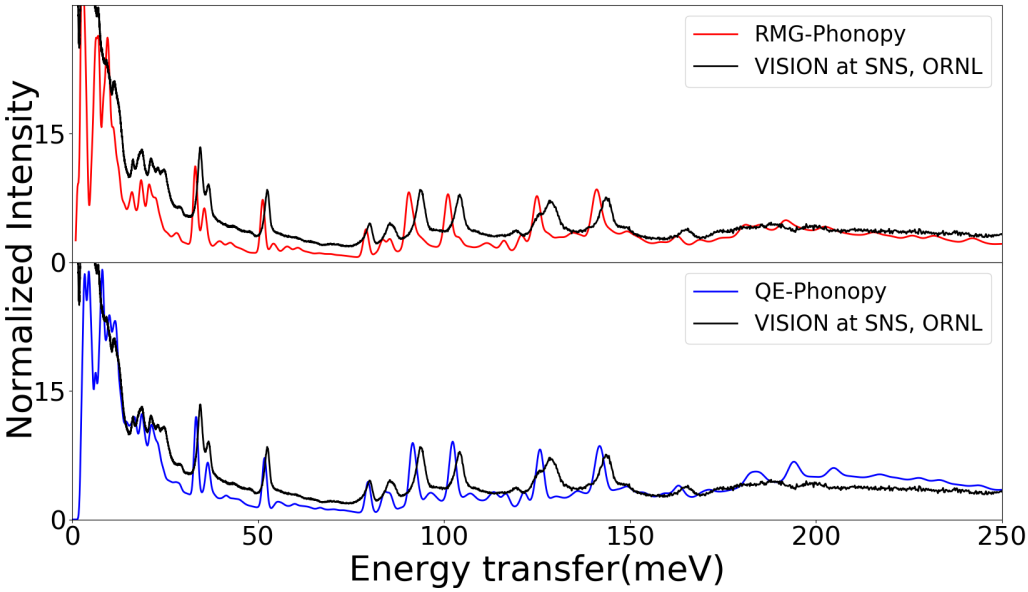

Figure 5.5 Comparisons of low-frequency vibrational intensities among RMG-Phonopy (red), QE-Phonopy (blue), and experimental data (black) at 5 K for ZIF-8.

spectra in very good agreement with plane-wave-based codes and experiment. An interface to Phonopy open-source phonon calculations package has been developed, which allows for easy calculation of vibrational properties of a large range of materials using RMG as the DFT computational kernel. We have also developed an RMG interface to the ALAMODE software for extraction of force constants from ab initio molecular dynamics via the temperature-dependent effective potential method to facilitate extraction of vibrational properties at finite temperatures and for anharmonic crystals. Since RMG is highly scalable on supercomputers and clusters and also offers scalable GPU support, it can be used in the future for very large-scale phonon calculations.

CHAPTER 6

STUDY OF ANHARMONICITY IN ZIRCONIUM HYDRIDES USING INELASTIC NEUTRON SCATTERING AND *AB INITIO* COMPUTER MODELING

In this chapter, we explore the phonon anharmonicity in zirconium hydrides by using DFT and INS.

6.1 Abstract

The anharmonic phenomena in Zirconium Hydrides and Deuterides, including ϵ-ZrH_2, γ-ZrH, and γ-ZrD, have been investigated from aspects of inelastic neutron scattering (INS) and lattice dynamics calculations within the framework of density functional theory (DFT). The observed multiple sharp peaks below harmonic multi-phonon bands in the experimental spectra of all three materials did not show up in the simulated INS spectra based on the harmonic approximation, indicating the existence of strong anharmonicity in those materials and the necessity of further explanations. We present a detailed study on the anharmonicity of zirconium hydrides/deuterides by exploring the 2D potential energy surface of hydrogen/deuterium atoms, and solving the corresponding 2D single-particle Schrödinger equation to get the eigenfrequencies. The obtained results well describe the experimental INS spectra and show harmonic behavior in the fundamental modes and strong anharmonicity at higher energies.

6.2 Introduction

Metal hydrides have been studied extensively during the past decades. In particular, there are special interests for their properties and applications in various areas, including hydrogen storage, utilization in nuclear reactors as neutron moderator [101] and fuel rod cladding materials [102] due to their low thermal neutron absorption cross-section and good mechanical properties, and also in the design of new types of actinide hydride fuels [103]. Therefore, numerous experimental and theoretical investigations on their structures and phonon properties have been conducted and reported in publications since the 1950s. It is well known that zirconium hydrides

have a complex phase diagram as a function of temperature, hydrogen content, and pressure [104–106]. Different phases such as ζ-$ZrH_{0.5}$ [107], γ-ZrH, δ-$ZrH_{1.5}$, ϵ-ZrH_2 have been identified. A stoichiometric γ-ZrH (face-centered orthorhombic metal sublattice) can be prepared by special temperature treatment [106]. Of those phases, this study focuses on γ-ZrH in Cccm space group, and ϵ-ZrH_2 in I4/mmm space group. Though the phase diagram has been determined, some hydrides' structures, stabilities, or formation mechanisms are still unknown [108].

The optical phonon properties of zirconium hydride were first analyzed using inelastic neutron scattering (INS) by Andresen et al. in 1957 [49]. Yamanaka [109] studied the thermal and mechanical properties of zirconium hydrides. Based on first-principles calculations, mechanical properties and thermodynamical properties of zirconium hydrides have also been broadly studied. Early studies by Ackland found that for ϵ-ZrH_2, bistable crystal structures exist with minimal energy difference [110]. The subsequent studies found that one of the bistable structures may be unstable or metastable. Elsasser found that for the center of the Brillouin zone (Gamma point) of ZrH_2, the potential energy profiles for hydrogen is a parabola up to about 300 meV and deviates at higher energies [111]. Besides theoretical studies, INS spectroscopy has also been employed to measure the vibrational spectra of ϵ-ZrH_2. The split peaks of multi-phonon events were observed in 1983 by Ikeda [112], yet was not explained. Kolesnikov et al. later attributed those split peaks below multi-phonon events in γ-ZrH and γ-ZrD to the bound multi-phonon states [98, 113].

Those experiments and calculations revealed that hydrogen vibrations in zirconium hydrides are highly anharmonic. Though phonon theory and techniques have been well developed, most of them are based on harmonic situations with a limited focus beyond that point. Phonon density of states (PDOS) with full consideration of

anharmonicity can be extracted from molecular dynamics (MD) simulations by the velocity autocorrelation function (VACF); however, only frequencies information can be obtained in this case, which is insufficient for further phonon analysis. Recently, the temperature-dependent effective potential (TDEP) method has been developed to address the anharmonicity problem by the MD method and taking temperature effects into consideration [22, 83]. However, these approaches are incapable of building directly comparable results with our broadband INS data for zirconium hydrides. Thus, an alternative technique is needed to address the problem. Besides, with a simple structure and large volume of experimental and simulation data, zirconium hydrides are excellent candidates to directly and unambiguously assess the quality of our anharmonic analysis.

Based on the considerations above, we present a qualitative and semiquantitative analysis that accounts for the effects observed in the INS spectra of zirconium hydrides by systematically investigating the potential energy surface (PES) of these materials using the density functional theory (DFT) and quantum theory. We sample PES in 2D planes due to considerations of the balance of practicality and accuracy. In this work, we successfully combined DFT and direct solutions of Schrödinger equations with INS spectra calculations. This work will hopefully improve our understanding of the mechanical and thermal properties of zirconium hydrides and can be applied to other metal hydride systems. The isotope effects were also investigated by checking the γ-ZrD system.

6.3 Methods

Multiple *ab initio* simulation packages within the framework of DFT have been employed to carry out first-principles calculations in this work, including the Vienna *ab initio* simulation package (VASP) [94, 114], and the Real-space Multi-Grid code (RMG) [38, 43, 115]. VASP is a plane-wave based DFT package with the implementation of multiple pseudopotentials. In all our VASP calculations, the electron-ion interaction and exchange-correlation functional were described by the projector-augmented wave (PAW) method [42] and the generalized gradient approximation (GGA) [116] with the parametrization of Perdew-Burke-Ernzerhof (PBE) [36], respectively. First-order Methfessel-Paxton scheme [117] with a smearing width of 0.05 eV was employed to integrate total energy in the Brillouin Zone (BZ), and the energy cutoff in the plane-wave functions was set to be 600 eV. Valence electron configuration in zirconium was carefully chosen as $4s^2 4p^6 4d^2 5s^2$ to include semi-core states, and in hydrogen was $1s^1$. The self-consistent convergence of the total energy calculation is 10^{-8} eV. RMG is an electronic structure calculation code based on the real-space method, implementing ultrasoft pseudopotential and norm-conserving pseudopotential. The RMG phonon methodology has been recently developed [24], and it is well suited for large-scale phonon calculations. In all RMG calculations, the real-space grid spacing was set to 0.15 Å, and norm-conserving pseudopotential with exchange-correlation described by PBE functional was used. Valence electrons for Zr were $4d^2 5s^2$. The convergence criteria for the root mean squared (RMS) change in the total potential energy per step was set as 10^{-7}, and a Fermi Dirac occupation type with electron temperature as 0.05 eV was used in energy integration.

The phonon dispersions of ZrH_x (ZrH_x means one of ϵ-ZrH_2, γ-ZrH, and γ-ZrD)

were calculated using the Phonopy package [88] employing the forces calculated by both VASP and RMG packages. Phonopy is an open-source package with interfaces to many commonly used DFT codes, including VASP, with built-in features such as phonon calculations, thermal physics calculations, etc. The maximum residual force in geometry optimization was 1 meV/Å. $2 \times 2 \times 2$ supercells of ZrH_x containing 96 (for ϵ-ZrH_2) or 64 (for γ-ZrH and γ-ZrD) atoms have been used for phonon calculations in the finite displacement method (FDM) with small atomic displacements of 0.01 Å in supercells. A Gamma centered $5 \times 5 \times 5$ k-mesh for ϵ-ZrH_2, $11 \times 11 \times 11$ for γ-ZrH and γ-ZrD was used to integrate total energy. K-mesh and energy cutoff have been tested to be converged with respect to total energy ranging up to 1 meV/atom in RMG and VASP. The phonon properties computed by the Phonopy package was used to simulate the INS spectra [30] by the OCLIMAX software [84, 87], a program aiming at simulating INS spectra based on vibrational normal modes with the capability of including coherent effects and temperature effects. A $31 \times 31 \times 31$ uniformly sampled k-mesh in the BZ was used to represent vibrational modes for our OCLIMAX calculations.

The frozen phonon calculations and potential surface sampling calculations were done with the VASP package.

To validate simulation results, experimental INS spectra for ϵ-ZrH_2 have been measured at the VISION spectrometer [118] at Spallation Neutron Source (SNS) in the Oak Ridge National Laboratory (ORNL), and INS spectra for γ-ZrH and γ-ZrD were measured previously [98, 113] at the TFXA spectrometer [119] at ISIS in the Rutherford Appleton Laboratory, UK. INS can measure the intensity of neutrons' direct interaction with nuclei with respect to both energy transfer and momentum transfer, with advantages of broad bandwidth, no selection rules, nondestructive

probe, and more importantly, INS simulations are straightforward. Thus, INS becomes a perfect technique to be combined with theoretical analysis.

6.4 Results and discussion

6.4.1 Atomic structures and phonon properties of ZrH_x

The crystal unit cells of ZrH_x and their phonon properties are shown in Fig. 6.1. The lattice vectors (a, b, c) used in our simulations for ϵ-ZrH_2 [120], γ-ZrH(γ-ZrD) [98] are (4.97728, 4.97728, 4.449) and (4.549, 4.618, 4.965) in Å, respectively. Note that phonon properties (especially optical modes) are sensitive to lattice parameters; thus, no geometry optimization is performed on the lattice vectors of these three materials to better compare to experiments. The phonon dispersions and phonon density of states (PDOS) for all three samples were calculated by DFT. Note that large phonon band gaps exist between high energy modes and low energy modes for all materials.

Fig. 6.2 shows the experimental INS spectra for ZrH_x, and Fig. 6.3 shows simulated INS spectra for ϵ-ZrH_2 with RMG/VASP+OCLIMAX along with VISION data. In Fig. 6.2, within the frequency region under 1000 meV, multiple peaks representing phonon excitations are observed in all materials. Focusing on ϵ-ZrH_2, the peaks at energies lower than 30 meV correspond to lattice modes of heavy Zr atoms in the crystals. The peaks at around 150 meV are corresponding to single phonon excitations of H atoms from the ground state to their first excited states (fundamental excitations). All higher energy peaks are overtones and combinations, corresponding to multi-phonon events excited from the ground state to the states higher than the first.

The INS spectra simulated from VASP and RMG for ϵ-ZrH_2 show excellent agree-

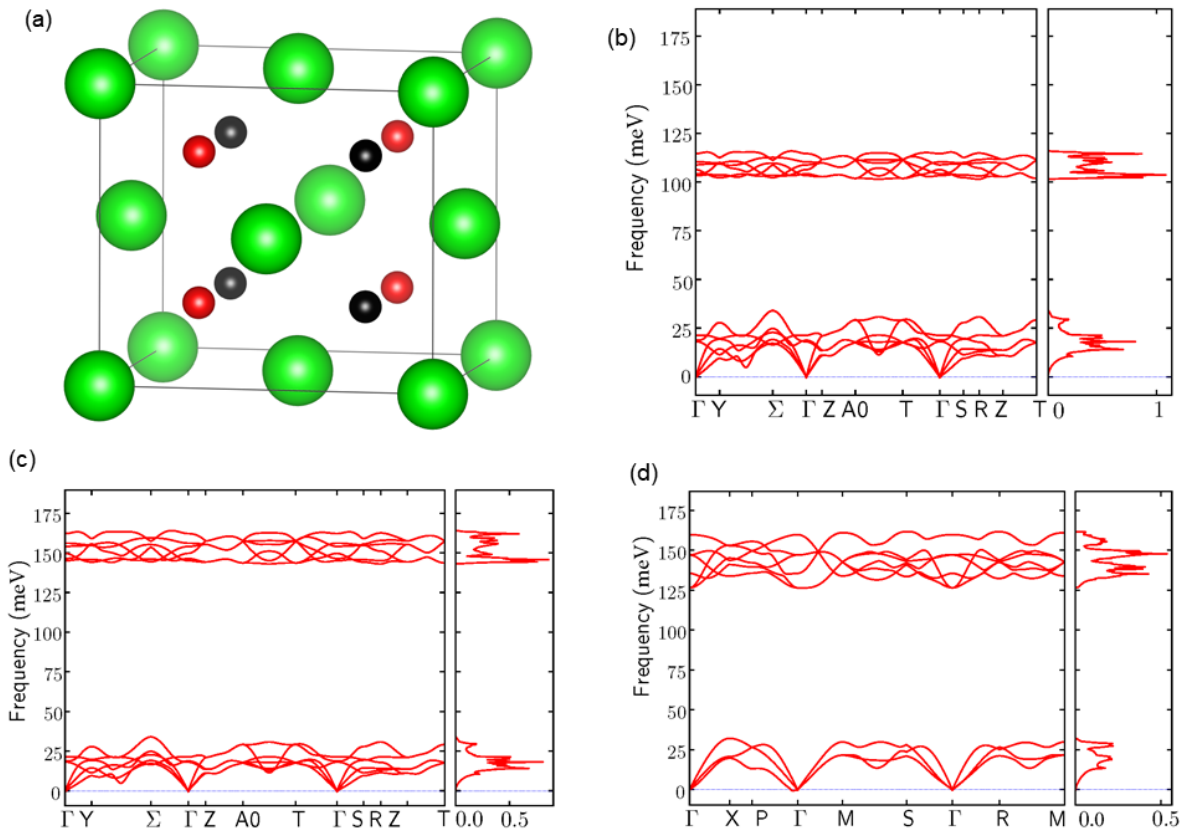

Figure 6.1 (a) Crystal unit cells for ϵ-ZrH_2 (space group I4/mmm), γ-ZrH and γ-ZrD (both are of space group Cccm), where H atoms in red exist in all structures, and H atoms in black only exist in ϵ-ZrH_2. Note that in calculations, lattice constants of ϵ-ZrH_2 and γ-ZrD(H) are different. Color scheme: Zr, green; H, red/black. Figures are drawn using the VESTA program [121]. (b), (c) and (d) are calculated phonon dispersions and PDOS for γ-ZrD, γ-ZrH and ϵ-ZrH_2, respectively. The BZ paths and notation are adopted from [122].

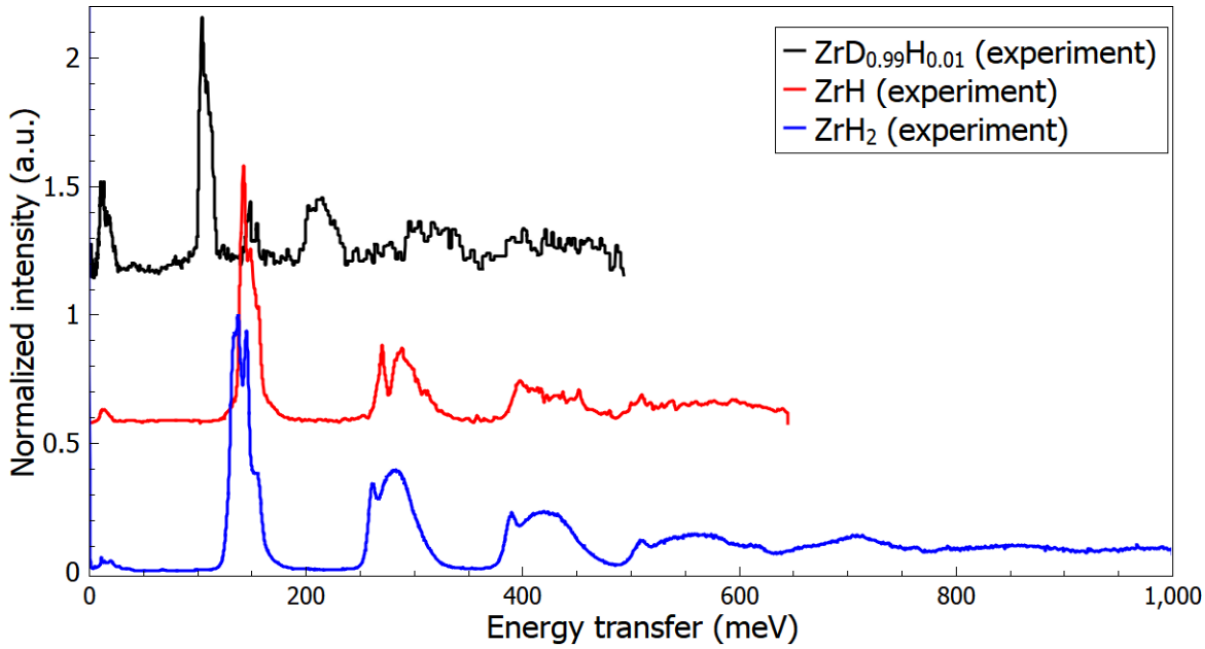

Figure 6.2 The INS spectra for ϵ-ZrH_2 measured with the VISION instrument at 5K (blue), γ-ZrH (red) at 4.5K and γ-ZrD (black) at 30K measured with the TFXA spectrometer. Spectra have been normalized to the same maximum value of the fundamental peaks for comparison purposes. Note that γ-ZrD sample has been contaminated by $\sim$1 at.% H, and also contained α- and δ-phases [98], with the actual ratio of Zr atoms in the different phases as $0.718(\alpha\text{-}ZrD_{0.001})+0.269(\gamma\text{-}ZrD_{0.98})+0.013(\delta\text{-}ZrD_{1.2})$, which results in extra peaks at $\sim$140 meV and higher intensity of the lattice modes (<30 meV) compared to the expected spectrum for pure γ-ZrD. Figures are drawn using the Mantid program [123].

ments with the experimental data at energies below 200 meV (see Fig. 6.3). However, discrepancies exist between the experimental data and the simulated INS spectra in the higher energy range. Overtone peaks at around 260 meV, 390 meV, and 510 meV exist only in the experimental data, suggesting the harmonic approximation is good for fundamental peaks but gets failing on higher energy excitations, and anharmonic effects need to be considered at higher energy. It should be noted that for γ-ZrH and γ-ZrD, similar split peaks were also observed in the experimental data (see Fig. 6.2).

The purpose of this work is to present a combined study regarding the anharmonicity of ZrH_x by using first-principles calculations and neutron techniques.

6.4.2 Harmonic approximation: frozen phonon method

Frozen phonon calculations were performed to explore the hydrogen potential energy profiles in ϵ-ZrH_2 as it usually captures the anharmonicity (if there is). The sampling directions of potential energy profiles were along the phonon polarization vectors, and the sampling displacements of H were chosen to be up to 1.0 Å with a step of 0.1 Å. Also, to reduce the computational cost, six low-frequency lattice modes (smaller than 30 meV) were not included in our frozen phonon calculations.

Our results show that all modes can be well fitted to parabolas, suggesting no anharmonic effects can be seen within displacement of 1.0 Å (which corresponds to energy range as high as few eVs) along the polarization directions, the frozen phonon method does not work in this case.

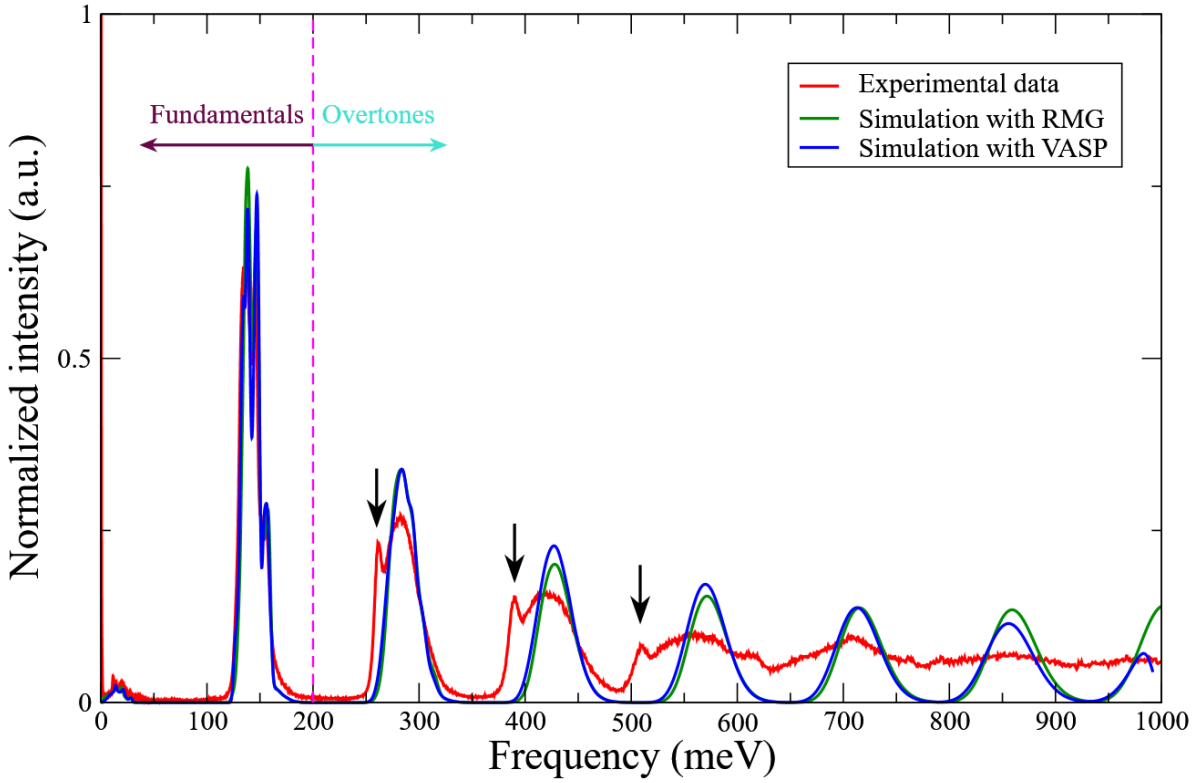

Figure 6.3 VISION INS spectrum (red) at 5K and simulated spectra with RMG (green) and VASP (blue) at 0K of ϵ-ZrH_2. Spectra are normalized with respect to their area under the fundamental spectra curve. Black arrows are marking peaks resulted from anharmonic effect (split peaks). The simulated data assumes the harmonic approximation.

6.4.3 A direct method: mapping eigenfrequencies from Schrödinger equations with simulated INS spectra

To obtain the phonon frequencies, an intuitive and accurate way is to solve the many-body Schrodinger equation representing the vibrations of all atoms directly. The Schrödinger equation may be easily solved for single-particle; however, it becomes impossible to solve as the system size significantly increases. Thus, we will try to simplify the complex many-body problem in two steps.

First, separate vibrations of H/D from vibrations of Zr. The justifications of this separation come from: 1) PDOS comparison between γ-ZrH and γ-ZrD as shown in Fig. 6.4. The high energy modes of γ-ZrD are scaled by a factor of $\sqrt{2}$ in energy, and $1/\sqrt{2}$ in intensity. The calculated PDOS in Fig. 6.4 shows that the low energy modes of γ-ZrD and γ-ZrH are almost identical (the theoretical ratio is 1.005 if Zr and H/D move in-phase), while the high energy modes differ by a factor of $\sqrt{2}$ (which is close to the frequency ratio $\omega_H/\omega_D = \sqrt{m_D/m_H} = 1.4136$ if we assume the H/D and the Zr are almost independent oscillators. In the harmonic approximation, the frequency of an oscillator with mass m is $\omega \propto \sqrt{k/m}$ where k is the force constant and m is the mass of the particle.), suggesting that Zr and H are almost independent oscillators. Olsson et al. draw similar conclusions on ϵ-ZrH_2 and ϵ-ZrD_2 [124]; 2) the charge densities of Zr and H in ϵ-ZrH_2 have near-spherical distribution with slight deformations, which indicates the Zr-H bonds and their couplings are weak [125]; 3) the mean square displacement (MSD) of Zr is much smaller than H/D's, as calculated by [30] at 0K:

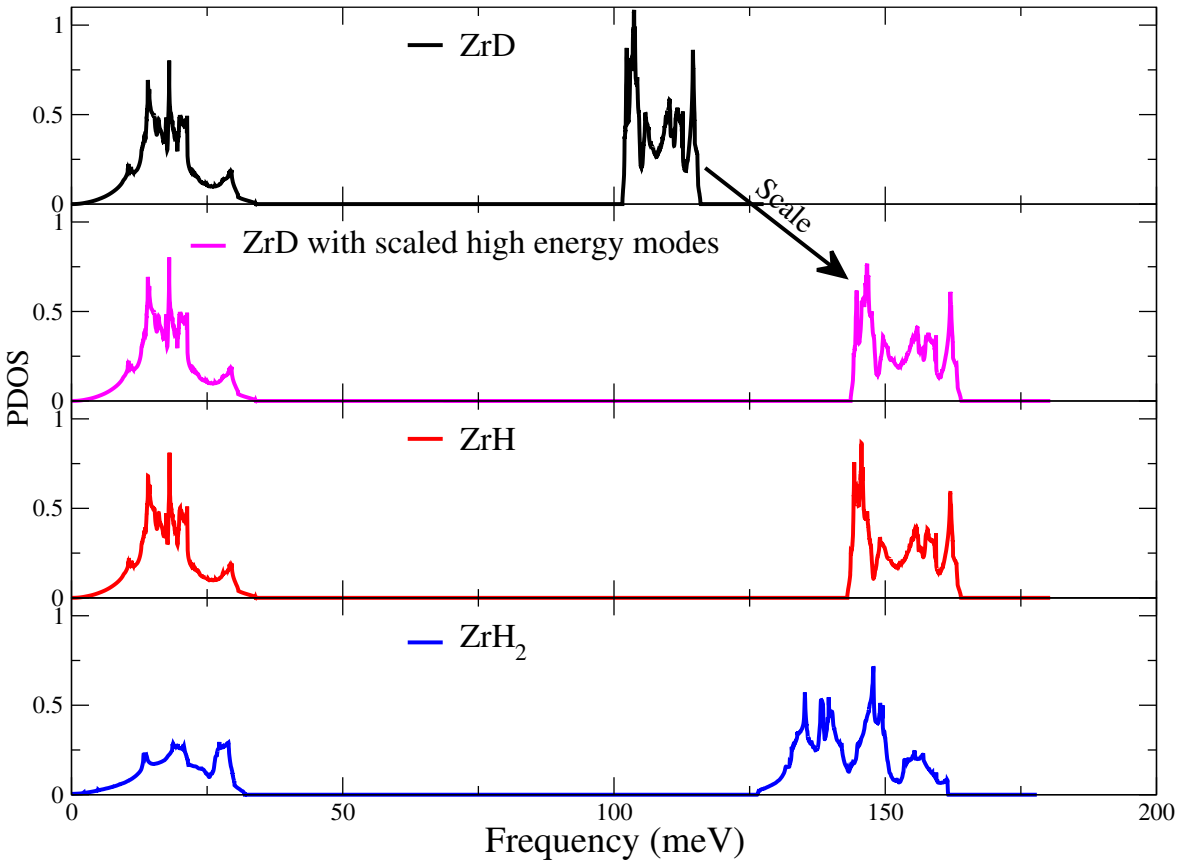

Figure 6.4 PDOS comparisons between γ-ZrD (black) and scaled high energy modes of γ-ZrD (magenta), γ-ZrH (red), and ϵ-ZrH_2 (blue). The high energy modes of γ-ZrD are scaled by a factor of $\sqrt{2}$ in energy, and $1/\sqrt{2}$ in intensity to obey DOS properties, which are represented by the black arrow. Low energy modes are almost identical between γ-ZrH and γ-ZrD, while high energy modes are nearly identical after scaled.

Table 6.1 Calculated MSD (and $\sqrt{MSD}$ in brackets) of Zr at (0, 0, 0), H/D at $(3/4, 1/4, 3/4)$ for ZrH_x in different energy range, units are in $Å^2$ for MSD and Å for $\sqrt{MSD}$. In γ-ZrH(γ-ZrD), MSD(Zr) varies slightly at different Zr positions (within 3%).

Property \ Energy Range	< 60 meV	> 60 meV
ϵ-ZrH_2		
MSD(H)	0.0019 (0.0436)	0.0433 (0.2082)
MSD(Zr)	0.0041 (0.0642)	0.00000396 (0.00199)
$\frac{MSD(H)}{MSD(Zr)}$	0.46 (0.68)	10934.34 (104.62)
γ-ZrH		
MSD(H)	0.0024 (0.0490)	0.0407 (0.2019)
MSD(Zr)	0.0044 (0.0663)	0.00000236 (0.00154)
$\frac{MSD(H)}{MSD(Zr)}$	0.55 (0.74)	17245.76 (131.10)
γ-ZrD		
MSD(D)	0.0024 (0.0490)	0.0286 (0.1690)
MSD(Zr)	0.0044 (0.0663)	0.000006738 (0.0025954)
$\frac{MSD(D)}{MSD(Zr)}$	0.55 (0.74)	4244.58 (65.12)

$$\boldsymbol{u}_l^2 = \frac{2.09}{m_l} \sum_q w_q \sum_\nu \frac{|\boldsymbol{\epsilon}_l(q,\nu)|^2}{\omega_{q,\nu}} \tag{6.1}$$

where l is the atomic index, ν is the index of normal mode, q is the index of points in BZ, m_l is lth atom's mass in atomic units, $\omega_{q,\nu}$ is the vibrational frequency in the unit of meV, $\epsilon_l(q,\nu)$ is lth atom's polarization vector of νth mode at point q, and w_q is the normalized weight of point q. Three lowest energy acoustic modes are not included in our calculations. The MSD is calculated within the low energy range (<60 meV) and the high energy range (> 60 meV), respectively. The results are listed in Tab. 6.1:

In the low energy range less than 60 meV, Zr and H/D atoms move with comparable amplitudes. However, in the energy range greater than 60 meV, the larger

ratio of $\sqrt{MSD(H)/MSD(Zr)}$ is indicating that H/D atoms are moving with larger amplitudes than Zr atoms at the same frequency.

Thus, it can be concluded that the vibrations of H/D can be viewed as fast degrees of freedom that are decoupled from the dynamics of Zr atoms.

Second, per conclusions in the first step, the Hamiltonian of a single H/D atom is:

$$\mathbf{H} = -\frac{\hbar^2}{2m}\boldsymbol{\nabla}^2 + V(\mathbf{r}) \tag{6.2}$$

where $\boldsymbol{\nabla}^2$ is the Laplacian operator on the H/D atom's wavefunctions, and $V(\mathbf{r})$ is the potential energy at position $\mathbf{r}$ (a set of $V(\mathbf{r})$ constitute the potential energy surface, PES). In our calculations, $V(\mathbf{r})$ are the DFT sampled potential energies of the H/D atom with substitution of its energy at the equilibrium position $\mathbf{r}_0 : V(\mathbf{r}) = E_{DFT}(\mathbf{r}) - E_{DFT}(\mathbf{r}_0)$. For the sake of simplicity and to present a simpler, yet robust explanation of the anharmonic effects, we use a 2D representation of $V(\mathbf{r})$ and thus $\mathbf{H}$. The 2D PES samplings provide a qualitative and semi-quantitative explanation of the anharmonicity in ZrH_x.

By checking the structure of ϵ-ZrH_2, we decided to sample the (112) plane (shifted so that the equilibrium position of the H atom is included in the plane) as this is one of the planes with the highest symmetry. The plane was sampled at a mesh density of 100 points per direction (mesh grid spacing around 0.005 Å, 10, 000 mesh grids totally). Based on the sampled grid, a finer grid with a dimension of $1200 \times 1600 = 1,920,000$ was generated using a linear interpolation method to build the Hamiltonian matrix according to Eq. 6.2. A similar scheme has been applied to γ-ZrH and γ-ZrD. A view of the plane and the sampled PES is shown in Fig. 6.5.

After solving the corresponding single-particle Schrödinger equation of H/D

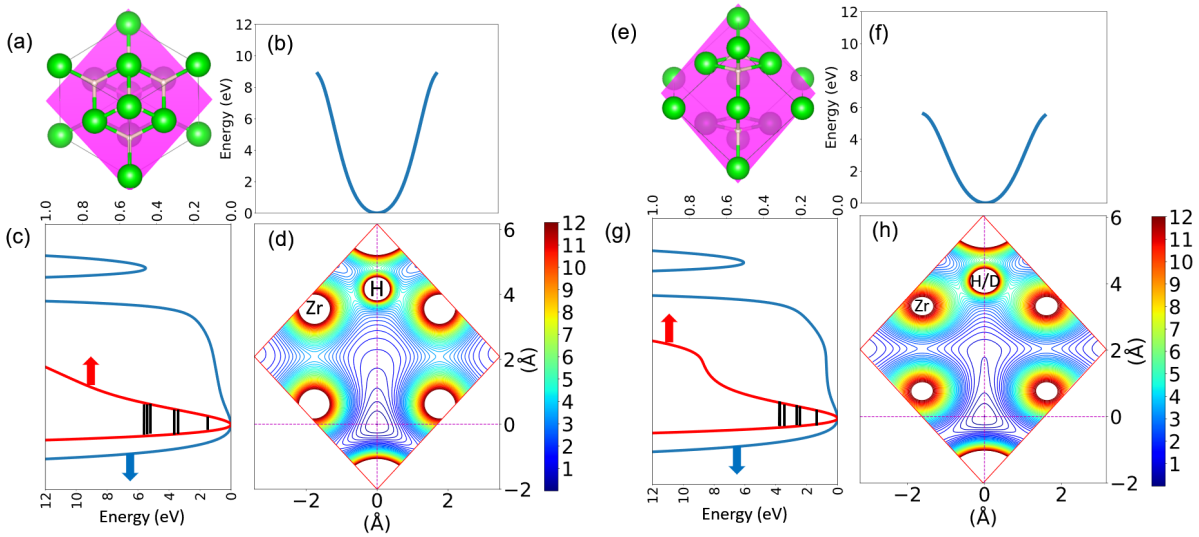

Figure 6.5 Crystal unit cells with sampling plane, contour plots and sectional views (blue curves) of PES for ZrH_x. (a)(b)(c)(d): plane (112) of ϵ-ZrH_2; (e)(f)(g)(h): plane (-112) of γ-ZrH and γ-ZrD. Color scheme: Zr, green; H, white; sampling plane: pink. The energy range within (0, 12) eV with 50 levels are used in contour plots, with minimum energies of 0 are all located at (0, 0). Red lines in (c) and (g) are enlarged plots in vertical directions within the energy range of (0, 1) eV, and black lines are indicating the first six eigenfrequencies (see Fig. **??**) from Schrödinger equations of ϵ-ZrH_2 and γ-ZrD, respectively.

atom, the eigenfrequencies and wavefunctions which represent the energy states of atoms in the PES can be displayed, as plotted in Fig. **??**. The three materials' eigenfrequencies have also been plotted in Fig. A.2 in the supplemental material A, and direct comparisons between eigenfrequencies and experimental spectra can be found in Fig. 6.6. It can be seen that the anharmonic peaks in experimental spectra can be reasonably described by eigenfrequencies from solving the 2D Schrödinger equation for the first few overtones (black dashed lines), and the discrepancies become larger at high energy levels. For example, in the case of ϵ-ZrH_2, the eigenfrequencies at around 264, 384, 493 meV are below the harmonic multi-phonon bands in magenta lines, and thus indicating the existence of anharmonicity. The eigenfrequency at 264 meV agrees well with the experimental value, yet the larger eigenfrequencies at 384 and 493 meV have around 6 and 17 meV's differences with experimental values, respectively, and the discrepancies are increasing at larger eigenfrequencies. Note that in (c), the ZrD sample was contaminated with H, and thus introduced the extra low-frequency peaks, e.g., at around 140 meV.

The eigenfrequencies from the Schrödinger equation include phonon properties in real space (PES). However, they are for the Gamma point only (BZ center) in reciprocal space, and it loses the information of phonon properties in other points. On the other hand, simulated INS spectra from DFT can sample the whole BZ (with fine enough grids) and include phonon information over the whole reciprocal space within the harmonic approximation. In order to qualitatively incorporate the anharmonicity into this model and to better compare experimental spectra and simulated spectra with the incorporated anharmonicity, we convolute the resulting anharmonic spectra at the center of the BZ from the Schrödinger equation, with the corresponding overtones calculated by DFT within the harmonic approximation. The change thus introduced to

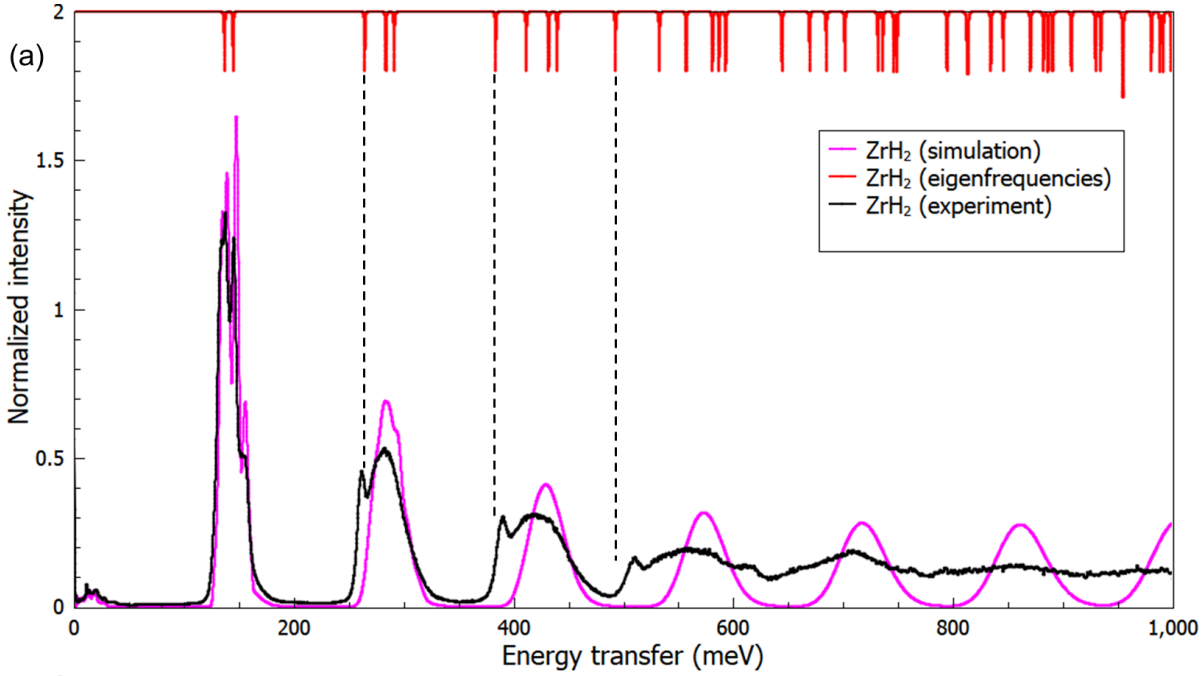
(a)
Normalized intensity
Energy transfer (meV)
ZrH₂ (simulation)
ZrH₂ (eigenfrequencies)
ZrH₂ (experiment)
0
0.5
1
1.5
2
0
200
400
600
800
1,000

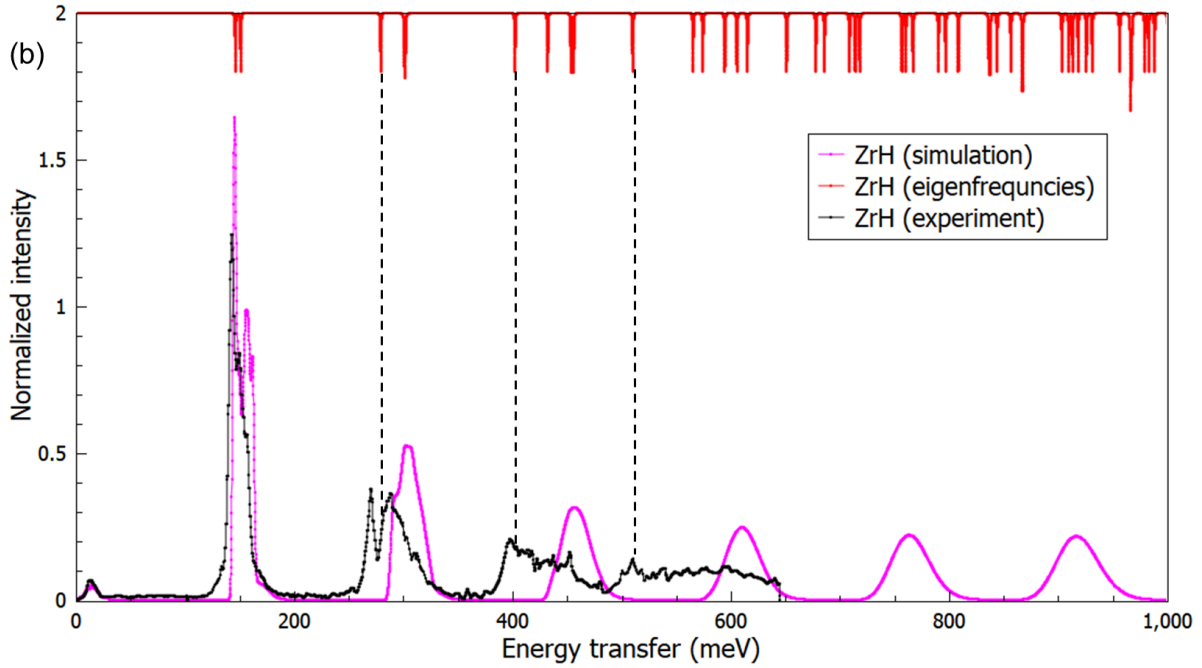
(b)
Normalized intensity
Energy transfer (meV)
ZrH (simulation)
ZrH (eigenfrequncies)
ZrH (experiment)
0
0.5
1
1.5
2
0
200
400
600
800
1,000

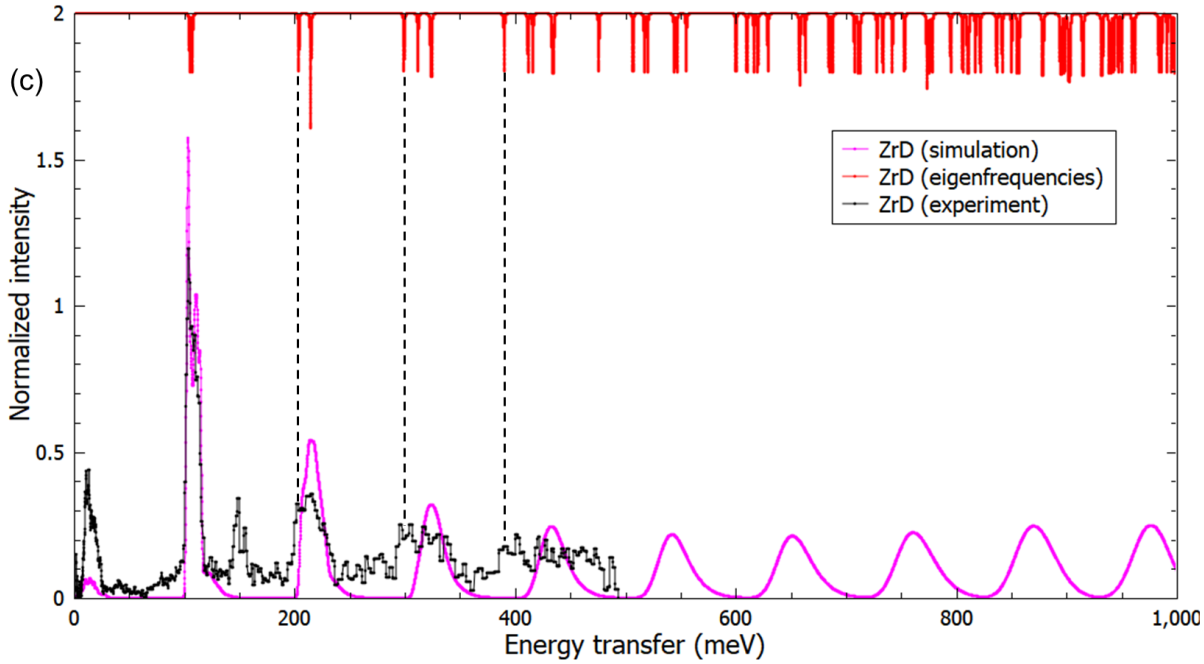

Figure 6.6 Comparisons between eigenfrequencies from Schrödinger equations and experimental INS spectra for: (a) ϵ-ZrH_2, (b) γ-ZrH, (c) γ-ZrD. Eigenfrequencies from Schrödinger equations are in red lines, experimental INS spectra are in black solid lines, simulated INS spectra are in magenta lines, and the black dashed lines are for eye guidance of comparisons between eigenfrequencies and anharmonic peaks for the first to third overtones.

the peak positions is a valid approximation, because the eigenvalues are very sensitive to small changes in the dynamical matrix, while the eigenvectors are not that sensitive to these changes and reflect the symmetry of the system [30].

$$S_{adjusted}(n) = S_n * \{\omega_1, \omega_2, \ldots, \omega_m\} = \frac{1}{m}\sum_{i=1}^{m} S_n(\omega_n - \omega_i) \tag{6.3}$$

$$S_{adjusted} = \sum_{n=1}^{N} S_{adjusted}(n) \tag{6.4}$$

The basic idea is, for each quantum event, to convolute the simulated spectra by DFT with eigenfrequencies from the Schrödinger equation as shown in Eq. 6.3, where n is the index of the quantum event, $\omega_i (i = 1 \ldots m)$ is the ith eigenfrequency of the 2D Schrödinger equation for quantum event n, S_n are the simulated spectra for quantum event n, ω_n is the "center of mass" (which is calculated by averaging spectra's energy transfer weighted by their intensity) of S_n, and $S_n(\omega_n - \omega_i)$ is a replica of but shifted by the difference between ω_n and $\omega_n = i$, $S_{adjusted}(n)$ are the final adjusted spectra to be compared with experimental data for this quantum event. The adjusted spectra for each quantum event are summarized to be the total adjusted spectra as shown in Eq. 6.4. A schematical representation of the convolution procedure is plotted in Fig. 6.7, and the adjusted results of ZrH_x are shown in Fig. 6.8. It should be noted that the convolution process here does not have physical meanings, and it is mostly for comparison purposes.

It can be seen that with the convolution process mentioned above, the original simulated peaks are mostly all broadened, and show better agreements with the experimental INS spectra. In the cases of γ-ZrH and γ-ZrD, we can see significant improvements in the peaks' positions, as both the original and the adjusted simulated

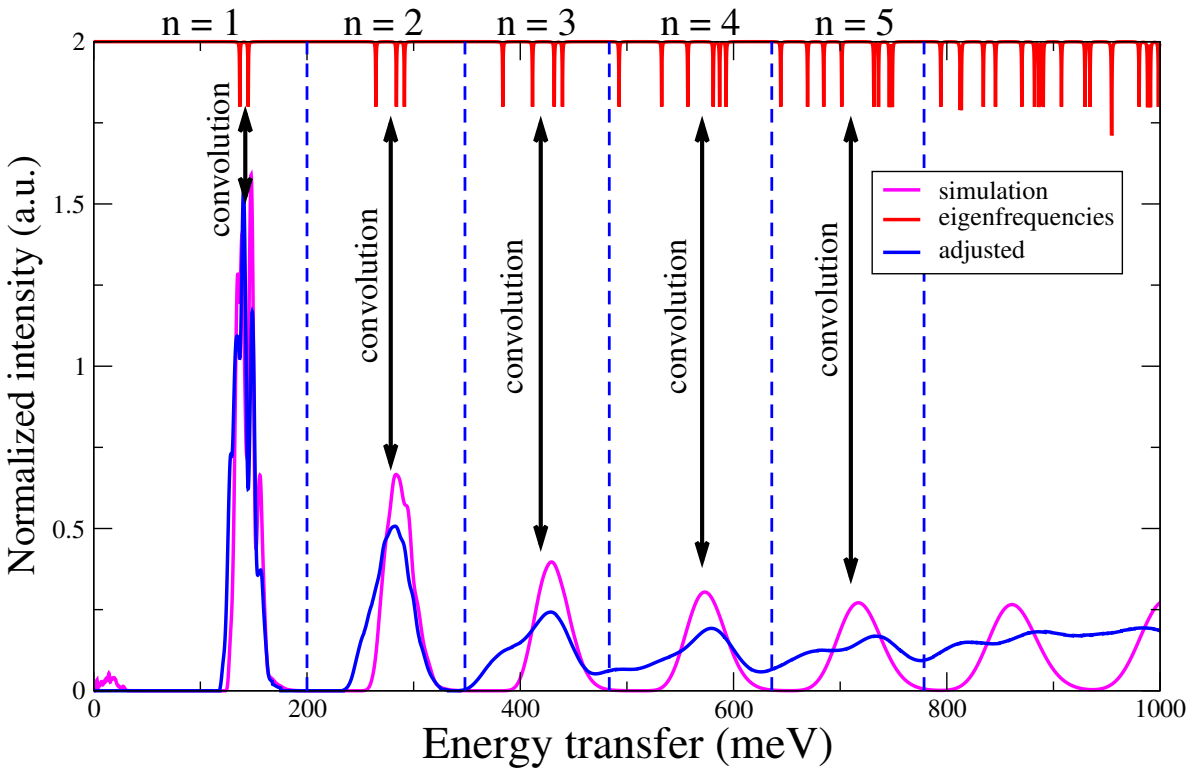

Figure 6.7 A schematic figure showing the convolution procedure. The convolution procedure was done within each individual quantum event indexed by n. Magenta lines are indicating simulation results, red are results from direct solutions from the Schrödinger equation, and blue lines are adjusted results after convolution between simulations and eigenfrequencies.

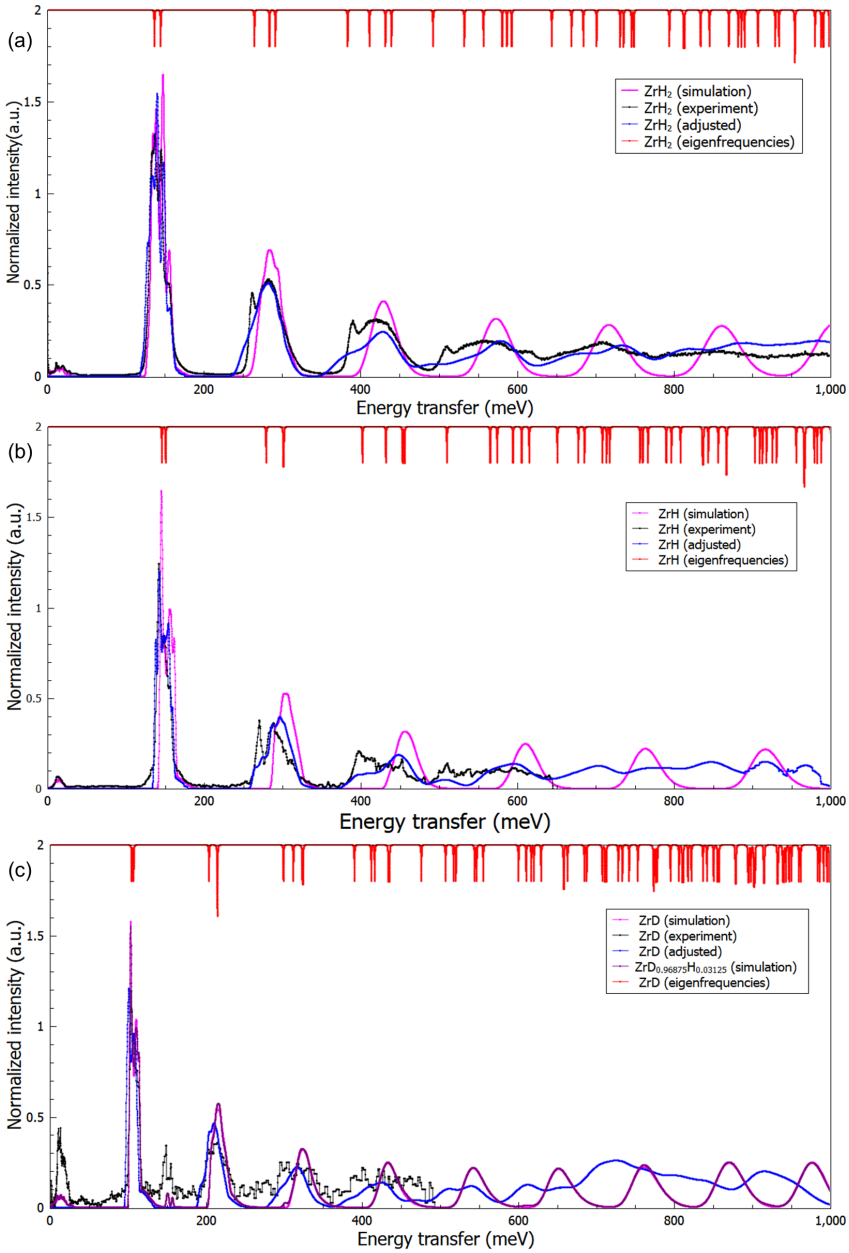

Figure 6.8 INS spectra for: (a) ϵ-ZrH_2, (b) γ-ZrH, (c) γ-ZrD. Eigenfrequencies from Schrödinger equations are in red lines, experimental INS spectra are in black lines, simulated INS spectra are in magenta lines, blue lines represent adjusted spectra after convolution, and purple lines in (c) are simulated spectra of contaminated γ-ZrD. Spectra are normalized with respect to their area under the fundamental spectra curve. The ratio of neutron scattering cross-section of H and D is 82.02/7.64=10.74, and m(D)/m(H)=2, therefore fundamental modes intensities ratio of 3% H to 97% D should be $\sim$10.74*2*0.03/0.97=0.66 (without corrections for the Debye-Waller factor). Note that in (c), the simulation spectra of ZrD and $ZrD_{0.96875}H_{0.03125}$ are almost on top of each other.

spectra have close shifts in energy transfer on multiple peaks. Since the γ-ZrD sample was contaminated with H, H atoms of concentration 3.125 at.% (1 in 32 D atoms in the simulation box was substituted by H atom) were also added to the pure γ-ZrD in our simulations. The calculation well reproduces the splitting of the hydrogen local mode peak at $\sim$150 meV into two peaks (double and single degenerate, according to the symmetry of the H position), and the absence of dispersion due to disorder of the H atoms in the lattice (random defects). Notice that the relative higher intensity of low energy modes in experimental γ-$ZrD_{0.99}H_{0.01}$ than simulated low energy modes of γ-$ZrD_{0.96875}H_{0.03125}$ is mostly due to contributed low energy modes by α-Zr [98].

Note, that the exact knowledge of vibrational dynamics of different Zr-H materials is important not only from the point of view fundamental physics and chemistry but also for practical applications in the nuclear field such as critical safety studies. Therefore the obtained results on dynamics of ZrH_x materials in the current study, which describes the anharmonicity of the INS spectra at energies above 300 meV, can be very useful for criticality and neutron transport simulations of the reactors containing Zr-H materials at anticipated operational temperatures up to 1200 (at which the first overtone level in Zr-H is $\sim$10% populated).

6.5 Conclusion

The anharmonicity phenomena in ϵ-ZrH_2, γ-ZrH, and γ-ZrD have been identified and thoroughly studied with techniques from both DFT and INS. The anharmonicity is not apparent on the fundamental vibrations, and it becomes evident at higher energies. This effect is not appreciable around room temperature. However, ZrH_x has been considered as a neutron moderator material for nuclear reactors; in this

case, the anharmonic effects cannot be ignored since neutron with high energies will scatter from the hydrogen atoms and will experience deviations from the scattering kernel predictions based on the harmonic approximation. While the harmonic model failed to capture the real potential energy surface and to explain the split peaks shown in experimental INS spectra, results by convoluting eigenfrequencies of the 2D Schrödinger equation with simulated INS spectra give a good description of the anharmonicity in these materials. By using the proposed convolution process in this article, one can see obvious anharmonic shifts of the overtones in the adjusted INS spectra which are in agreement with the experimental data. The method proposed here, combining DFT and OCLIMAX, is a possible way to explain anharmonicity in materials beyond harmonic phonon theories. This work could shed light on further studies on phonon calculations on the anharmonic systems like TiH_x, PdH_x, and other metal-hydrogen systems.

CHAPTER 7

THEORETICAL STUDY OF ALKALI-METAL HYDRIDES AT HIGH PRESSURES: A CASE OF NAH SUPPORTED BY INELASTIC NEUTRON SCATTERING (INS) EXPERIMENTS AT 1 AND 2 GPA

In this chapter, we describe high pressure induced effects in alkali hydrides, by using the DFT and INS techniques.

7.1 Abstract

Pressure-induced effects in alkali hydrides are investigated using a plane-wave density functional theory method. For the first time, we have measured the inelastic neutrons scattering (INS) spectra of NaH at pressures 1 and 2 GPa and used it to validate INS simulated from the firstprinciples calculations using both local density approximation (LDA) and the generalized gradient approximation (GGA). We found that LDA describes lattice dynamics better compared to the GGA. Thermodynamic properties such as lattice parameters, bulk modulus, and their derivatives are calculated using full lattice dynamics theory within the quasi-harmonic approximation (QHA) for all alkali hydrides. Anharmonic effects are investigated for NaH from the molecular dynamics trajectories and are negligible at given temperature and pressures. We have shown that the phase-change pressures obtained from the equal Gibbs free-energy conditions for two phases compare well with the available experimental data and is the accurate phase-change criterion. This study corroborates INS as an important complementary tool in benchmarking first-principles calculations.

7.2 Introduction

Alkali-metal hydrides ([Li-Cs]H), the simplest hydrides, have been studied extensively both experimentally [126, 127] as well as theoretically [128–130]. These metal hydrides adopt NaCl-type rocksalt (B1) structure at ambient temperature and pressure and undergo a structural phase transition from B1 to CsCl-type structure (B2) at high pressures depending on a cation size. For LiH, different theoretical studies predict contradicting phase-change pressures [131, 132]. For NaH and KH, phase change takes

place at much lower pressures than the one of LiH that are experimentally attainable despite being highly reactive to the atmospheric gases. RbH and CsH show the phase transition at very low pressures as shown by some theoretical studies [128, 130]. Despite considerable theoretical studies, it is desirable to investigate high-pressure phases of these hydrides with different theoretical and experimental techniques for a better understanding of their atomic, electronic, and structural properties.

Inelastic neutron scattering (INS) spectroscopy is a useful tool to probe hydrogen motions in the hydrogen containing systems and has a simple theoretical description, which can be simulated from the normal modes obtained by the lattice dynamics calculation under the harmonic approximation [30, 87]. Recently, we have shown that these normal modes are sensitive to the functional used in the calculation and must be carefully benchmarked for the accurate spectral assignment [133]. To study the thermodynamic properties at finite temperature and pressure and to improve the spectral prediction, the partial anharmonic effect can be incorporated within the quasiharmonic approximation (QHA). Barrera et al. [129] and Yu et al. [134] have shown the inadequacy of static approximation and the importance of finite-temperature effect in the thermodynamic properties of alkali-metal hydrides.

In this work, to our knowledge, for the first time, we have carried out inelastic neutron scattering (INS) experiments on NaH at pressures 1 and 2 GPa and the spectra are compared to the simulated spectra from lattice dynamics calculations with both local density approximation (LDA) and generalized gradient approximation (GGA) within the quasi-harmonic limit. The calculations are carried out to remaining alkali hydrides, and the thermodynamic properties such as lattice parameters, bulk modulus, and its derivatives at different temperatures are probed. We have compared the phonon dispersion for NaH at different pressures calculated from the molecular dynamics

trajectories to the one obtained from the lattice dynamics calculation to investigate the anharmonic effect. We have highlighted the importance of quasi-harmonic approach in the lattice dynamics calculation to study the temperature effect as well as in dynamical properties such as lattice constants, bulk modulus, and its derivatives at different temperature and pressures states. This study opens up an avenue in validating the high-pressure calculations with higher theoretical level of accuracy using INS.

The rest of this paper is organized as follows. In Methodology 7.3, we describe the methodology for the current work. In Results and discussion 7.4, we present the results. The conclusions are given in Conclusions 7.5.

7.3 Methodology

In lattice dynamics calculation, Helmholtz free energy at volume V and temperature T is given by the sum of static energy and the vibrational term [129, 134, 135]

$$F(V,T) = E_{stat} + F_{vib}(\omega, T) \tag{7.1}$$

where E_{stat} is the static contribution from the internal energy and F_{vib} is the vibrational contribution to the free energy is given by

$$F_{vib}(\omega, T) = \sum_{j=1}^{3N} \sum_{q} \left(\frac{1}{2}\hbar\omega_j(q) + kT \ln\left(1 - e^{\hbar\omega_j/kT}\right) \right) \tag{7.2}$$

where $\omega_j(q)$ is the normal mode j for each reciprocal space point q obtained from the lattice dynamics calculation with harmonic approximation and T is the absolute temperature [136]. In Eq. 7.2, the first term represents zero-point energy at $T = 0$ and

the second term arises due to the thermal excitation. Gibbs free energy is given by

$$G(P,T) = F(V,T) + PV \tag{7.3}$$

Gibbs free energy is equal to the Helmholtz free energy at zero pressure, and, therefore, the equilibrium crystal structures at a given temperature T are obtained by minimizing the Helmholtz free energy with respect to the volume. The phasetransition pressure from NaCl-type to CsCl-type phase is the one at which both the phases have the same Gibbs free energy.

To determine the structural properties at a certain temperature, calculated Helmholtz free energies are fitted to the Birch third-order equation of state, which is given by [134, 137]

$$\begin{aligned} F(V,T) = F(V_0) &+ \frac{9}{10} B_0 V_0 [(V0/V)^{2/3} - 1]^2 \\ &+ \frac{9}{16} B_0 V_0 (V_0' - 4)[(V0/V)^{2/3} - 1]^3 + O([(V0/V)^{2/3} - 1]^4) \end{aligned} \tag{7.4}$$

where B_0 is the bulk modulus and B_0' is its pressure derivative at the equilibrium volume V_0.

The intensity of an inelastic neutron scattering (INS) band is given by [30, 129, 133]

$$S_l(Q, n\omega_v) = \sigma_l \cdot \frac{[(Q \cdot u_{l,v})^2]^n}{n!} exp\left[- \left(Q \cdot \sum_v u_{l,v} \right)^2 \right] \tag{7.5}$$

where σ_l is the scattering cross-section of atom l, $u_{l,v}$ is the atomic displacement amplitude of the atom l in a mode v, and ω_v is the frequency of that mode. Q is the magnitude of momentum transfer and n is the order of vibrational excitation. Detail

information about the INS and its derivation can be found in ref [30], INS spectra are simulated from the Oclimax software [84], which is the latest version of aClimax code [87].

Born effective charge (Z^*) is the change in polarization produced by the isolated atomic displacement under the condition of zero macroscopic electric field. Detail explanation of Born effective charge and its comparison with other dynamical and static charges can be found in refs [20, 138]. For the NaCl-type rocksalt structure of alkali hydrides, magnitudes of Z^* for metal and hydrogen are equal and are opposite in sign due to symmetry. LO-TO splitting, the splitting of the longitudinal optical mode and transverse optical mode at Brillouin zone (BZ) center, is the direct consequence of Born effective charge [20].

First-principles calculation of lattice dynamics is carried out using a plane-wave density functional theory code CASTEP [139]. Exchange-correlation energy is approximated by local density approximation (LDA) and generalized gradient approximation (GGA) using the Perdew-Burke-Ernzerhof parametrization [140]. The energy cut-off of 1200 eV is taken with the 19 × 19 × 19 Monkhorst-Pack grid for the electronic sampling of the Brillouin zone (BZ). The normal modes are calculated by the density functional perturbation theory [57] with a coarse qpoint grid of 9 × 9 × 9 to sample the BZ and a fine q-point mesh of 33 × 33 × 33 for the Fourier interpolation in the entire BZ.

As for finite-temperature phonon calculations, we employed the temperature-dependent effective potential method [22], as implemented in the ALAMODE package [90]. To calculate interatomic force constants (IFCs), 10 000 molecular dynamics (MD) steps with a time step of 1 fs were performed by CASTEP in the NVT ensemble at 500 K, and the forcedisplacement datasets were extracted from the last 7000 steps. The IFCs were calculated by considering all interactions in a 3 × 3 × 3 supercell, which are

used to obtain the dynamical matrix and phonon dispersions. An Ewald summation technique-based longitudinal optical and transverse optical (LO-TO) splitting [141] was also included whenever necessary in phonon calculations by ALAMODE. The Born effective charges required for the calculations of LO-TO splitting are obtained from the CASTEP calculations.

7.4 Results and Discussion

7.4.1 Inelastic Neutron Spectroscopy (INS)

Equilibrium volumes are obtained from the Birch third-order equation of state fit of static energy E_{stat} and Helmholtz free energy $F(V,T)$ at 5 K, and different volumes as shown in Figure 7.1. The minimum energy positions are shown by arrows. Lattice expansion at 5 K is mainly due to the contribution from zeropoint energy, with a very little thermal contribution.

INS spectra of NaH at zero pressure, 1 and 2 GPa, are measured at the VISION spectrometer at Spallation Neutron Source (SNS). The experimental pressures are applied using the CuBe pressure cell. Experimental INS spectra of NaH at zero pressure and 5 K temperature compared to the simulated spectra from the linear response lattice dynamics calculations using LDA for the equilibrium structures from the static energy minimum and the free-energy minimum at 5 K are shown in Figure 7.2. These spectra are simulated from the latest version of the OClimax software [84] and exhibit the shift in modes to the lower-frequency region by the incorporation of zero-point energy and thermal contribution. This reproduces some parts of experimental spectra, thereby, revealing the importance of vibrational contribution in the study of thermo-

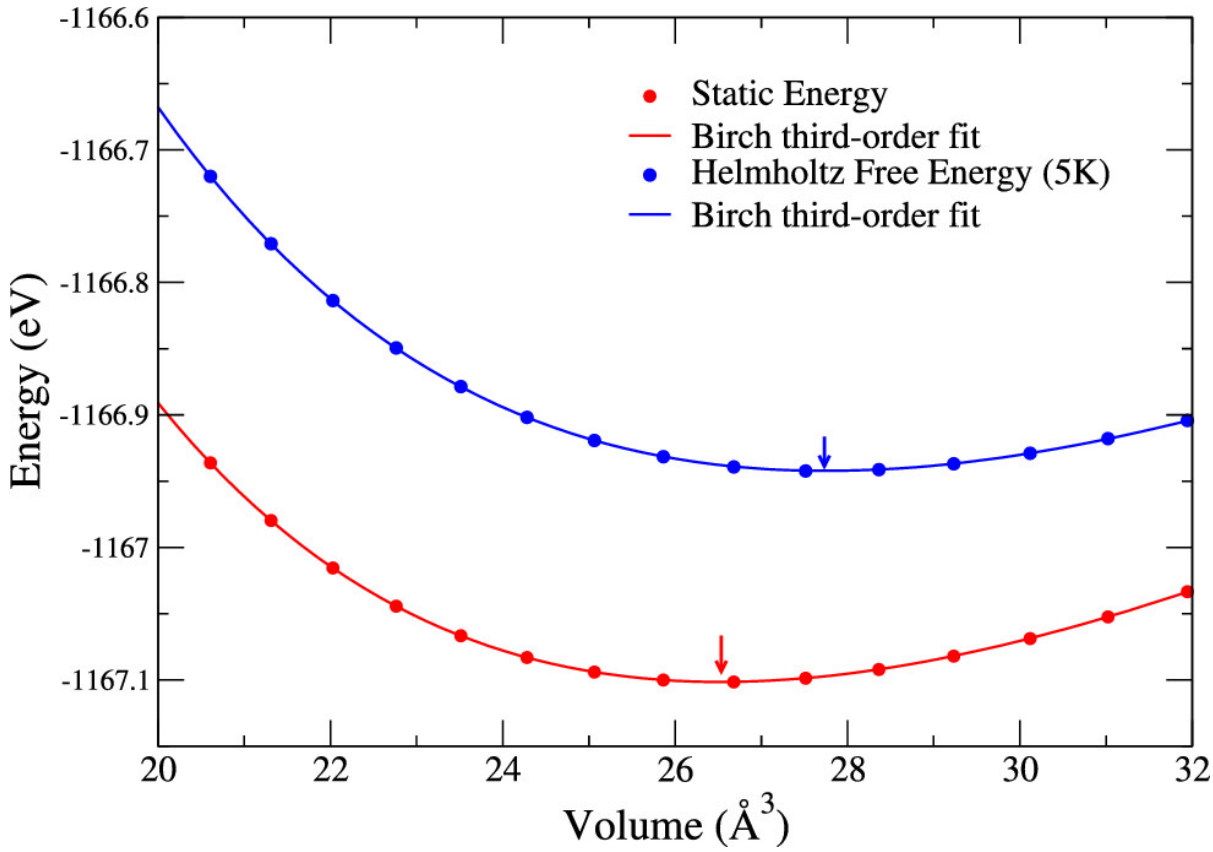

Figure 7.1 Variation of Helmholtz free energy at 5 K and the density functional theory (DFT) static energy for NaCl-type structure of NaH with volume using LDA. Corresponding minimum energies are shown by the respective arrows.

dynamical properties. This result is consistent with the previous work by Barrera et al., where the simulated spectra for alkali hydrides including QHA compare well with the experimental spectra [129]. All of the contributions above 1000 cm^{-1} are due to the overtones and combinations.

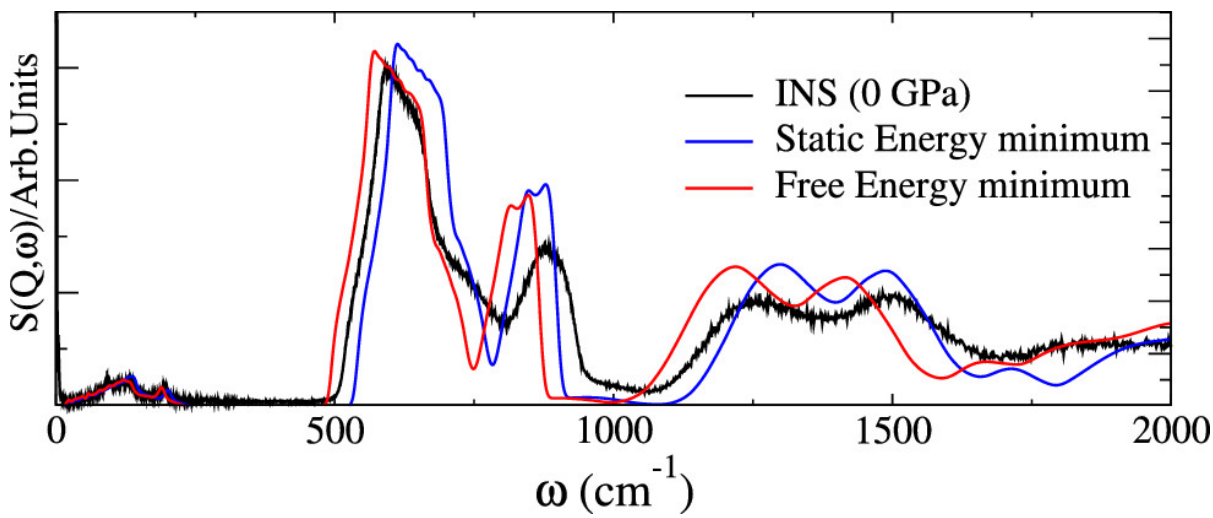

Figure 7.2 Inelastic neutron scattering (INS) spectrum of NaH at 0 GPa pressure (black) at temperature 5 K measured at a VISION spectrometer at Spallation Neutron Source (SNS). Simulated INS spectra for NaCl-type structure of NaH at the static energy equilibrium structure (blue) and free-energy equilibrium structure at 5 K (red) using DFT under LDA.

INS spectra for NaH at 1 and 2 GPa pressures measured at VISION are shown on the top panel of Figure 7.3. The lowenergy peaks below 500 cm^{-1} in the experimental spectra are dominated by the signals from the CuBe pressure cell and are truncated. To our knowledge, this is the first time such highpressure experimental spectra have been measured using neutron spectroscopy. There is clearly a blue-shift of the peak around 600 cm^{-1}, and also its overtones are shifted. INS at experimental pressures are simulated with both LDA and GGA under QHA. The middle panel in Figure 7.3 shows the simulated INS for the equilibrium structures using LDA-DFT for lattice dynamics

calculations under QHA at experimental pressures 0, 1, and 2 GPa, while the lowest panel is the one obtained from the GGA-DFT lattice dynamics calculations. The arrow at the top panel shows the starting of the main peak around 600 cm^{-1} for experimental spectra. Clearly, spectra obtained from the LDA with thermal contribution match well with the experiments, including the peak positions for all three pressure conditions. We have estimated the shifts ($\Delta\omega$ (cm^{-1})) in two major peaks in the experimental spectra and the simulated spectra using both LDA and GGA relative to the zero-pressure spectra, which are shown in Table 7.1. The first peak in the experimental spectra is shifted by 27.45 and 51.03 cm^{-1} with respect to the zero-pressure spectra when the pressure is increased from 1 to 2 GPa, respectively, with a ratio of 1.86. This shift is comparable to the calculated spectra from DFT-LDA with 33.93 cm^{-1} for 1 GPa and 66.15 cm^{-1} for 2 GPa with ratios of 1.95 and 48.15 cm^{-1} for 1 GPa and 80.5 cm^{-1} for 2 GPa for DFT-GGA with a ratio of 1.67. This shows the first peak shift due to pressure obtained from LDA compares well with the experiment compared to GGA calculations. For the second peak, the shifts are 29.74 and 57.13 cm^{-1} from 1 to 2 GPa with a ratio of 0.52 for the experimental spectra compared to 26.91 and 53.03 cm^{-1} with a ratio of 0.51 for the calculated spectra from LDA and 36.66 and 61.62 cm^{-1} with a ratio of 0.59 for GGA. This supports the study by Barrera et al. [129] and shows that lattice dynamics with LDA and thermal contribution describes the system better than GGA, both at the equilibrium and increased pressure conditions. We have successfully used the high-pressure experimental INS spectra in benchmarking the DFT functionals.

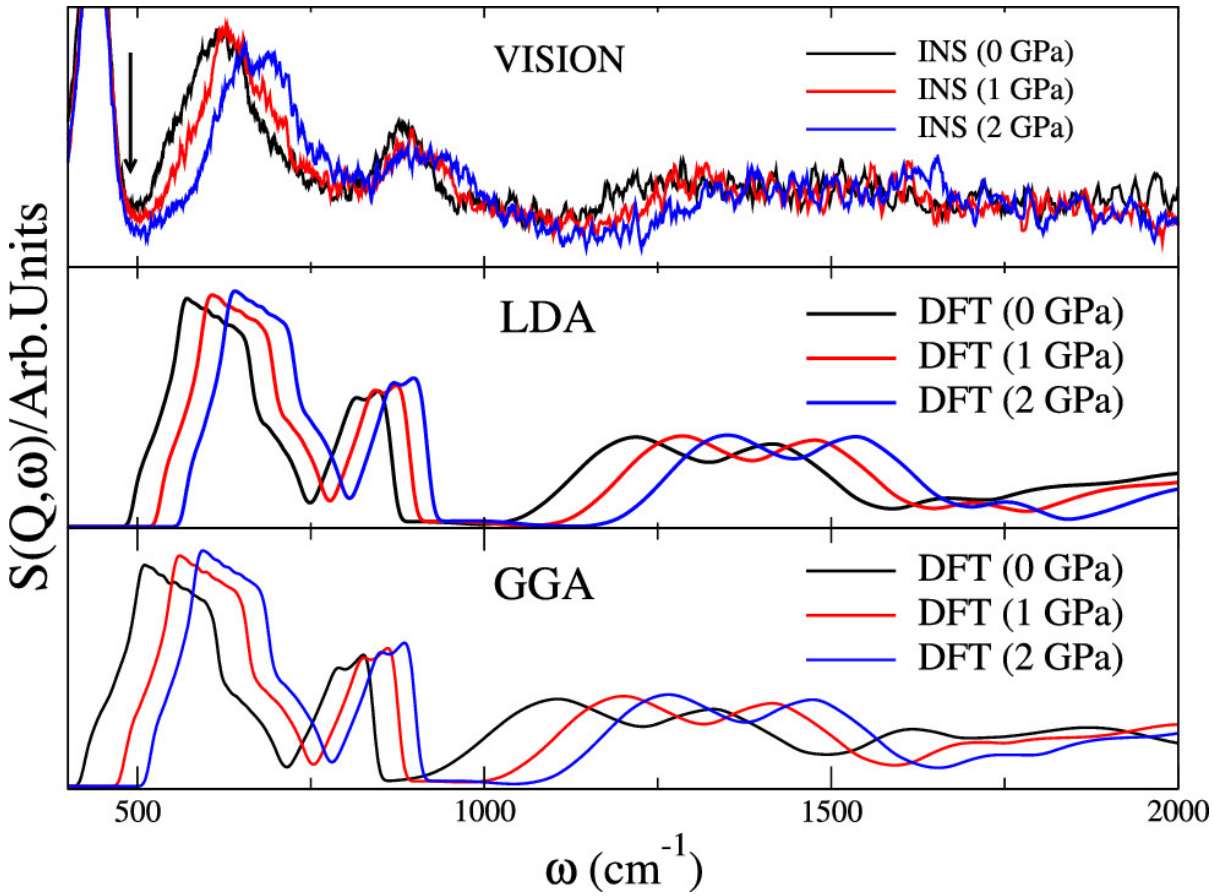

Figure 7.3 Inelastic neutron scattering (INS) spectrum of NaH at pressures 0, 1, and 2 GPa and temperature 5 K from the VISION spectrometer at Spallation Neutrons Source (SNS). Arrows show the shift in starting positions of peaks around 500 cm^{-1}. The region below 500 cm^{-1}, shown by the arrow, is dominated by the background peaks from the CuBe sample holder can. (Middle panel) Simulated INS for the NaCl-type structure of NaH at 5 K using DFT under GGA at experimental pressures. (Lowest panel) Simulated INS for the NaCltype structure of NaH at 5 K using DFT under LDA. Black: equilibrium volume, red: 1 GPa and blue: 2 GPa.

Table 7.1 Shift in First and Second Peak Positions for 1 and 2 GPa Relative to Zero Pressure (0 GPa)

Pressure	1 GPa	2 GPa	ratio (2:1 GPa)
First Peak Shift $\Delta\omega(cm^{-1})$			
expt	27.45	51.03	1.86
LDA	33.93	66.15	1.95
GGA	48.15	80.5	1.67
Second Peak Shift $\Delta\omega(cm^{-1})$			
expt	29.74	57.13	0.52
LDA	26.91	53.03	0.51
GGA	36.66	61.62	0.59

7.4.2 Phase Change with Pressure and Thermodynamic Properties

To estimate the phase-transition pressure at 298 K, we calculated the Gibbs free energy for both B1 (NaCl-type) and B2 (CsCl-type) phases and the pressure at which Gibbs free energy is the same for both the phases gives the phase-change pressure (PCP). Figure 7.4 shows the variation of Gibbs free energy with pressure for both the phases of NaH using LDA and GGA. The difference in Gibbs free energy (ΔG) for two phases is plotted in the insets. Phase-change pressures of NaH calculated from LDA and GGA at 298 K are 29.26 and 30.81 GPa at volume fractions of V/V_0 = 0.61 and 0.57, respectively. These values are in a very good agreement with the experimental values obtained from a diamond anvilcell high-pressure experiment for NaH, which are 29.30 GPA for PCP and V/V_0 = 0.61 for volume fraction at PCP [126, 142]. Our results are better compared to 32 and 37 GPa from other theoretical studies [130, 143]. The discrepancy in theoretical results from different methods calls for an experimental data necessary for benchmarking these calculations, and our study shows that INS spectroscopy can be a suitable alternative for benchmarking theoretical calculations.

Table 7.2 Phase-Change Pressure (PCP) and Volume Fraction (V/V_0) at the Phase Change for Alkali Hydrides from Lattice Dynamics Calculations. V_0 is the Equilibrium Volume

	NaH (LDA)	NaH(GGA)	KH (LDA)	RbH (LDA)
PCP (GPa)	29.26 (29.30 [126])	30.81 (29.30 [126])	3.27 (4.00 [126])	0.64 (2.20 [126])
$V/V0$	0.61	0.57	0.86	0.96

This again supports that LDA gives better results compared to GGA for the lattice dynamics calculations. We have used the same technique to calculate the phase-change pressures for KH and RbH from lattice dynamics calculations using LDA, which are shown in Figure 7.5. The calculated PCP for KH is 3.27 GPa, which compares well with the experimental value of 4.0 GPa [126, 142]. For RbH, the calculated value is 0.64, which is lower than the experimental value of 2.2 GPa [126, 142]. Because of the huge variations in the theoretical results of LiH and CsH, we limit our calculations to the middle three hydrides in the series. These results are shown in Table 7.2.

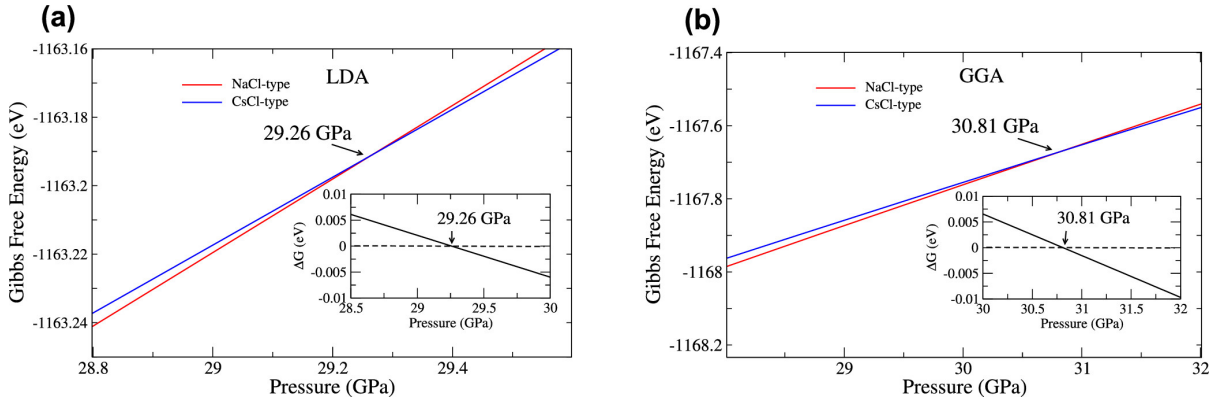

Figure 7.4 Gibbs Free energy as a function of pressure for NaCl-type and CsCl-type structures of NaH using LDA and GGA at 298 K. (a) NaH for calculations using LDA and (b) NaH for calculations using GGA.

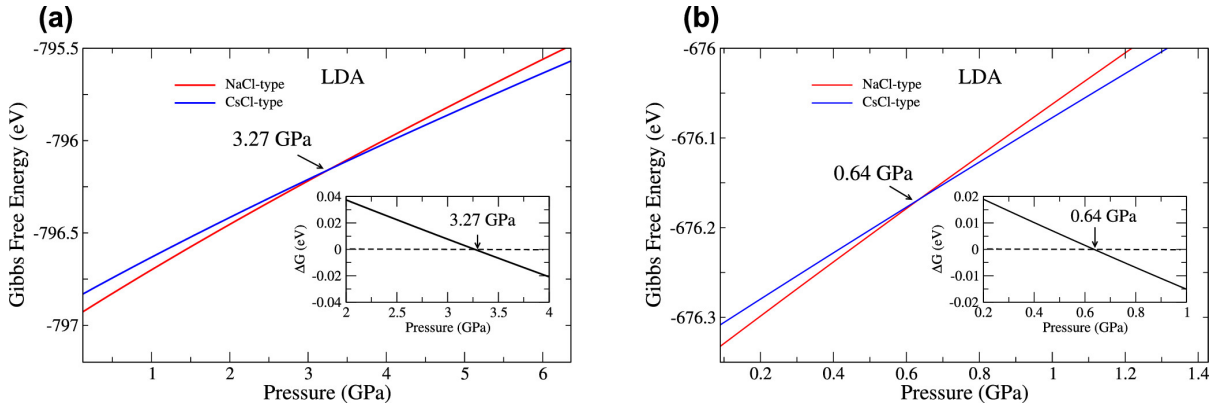

Figure 7.5 Gibbs Free energy as a function of pressure for NaCl-type and CsCl-type structures of KH and RbH using LDA at 298 K. (a) KH and (b) RbH.

PV equation of state for the B1 phase of NaH at 5 K is shown in Figure 7.6. The phase-change volume and pressure are shown by a broken line and the experimental pressure region is enlarged in the inset with arrows 1, 2, and 3 showing zeropressure, 1 and 2 GPa pressure regions, respectively. INS for regions 1, 2, and 3 are experimentally measured and calculated, as discussed above. We have calculated the lattice parameters, bulk modulus and its derivatives for all five alkali hydrides, which are shown in Table 7.3. For NaH, the lattice constants (a) at 298 K obtained from the lattice dynamics calculations using LDA and GGA are 4.843 and 4.990 Å, respectively, compared to the experimental value 4.89 Å [144], showing that the result from LDA is better than the one from GGA. Lattice constants without thermal contribution, that is from the equilibrium volume corresponding to static energy minimum, are underestimated to 4.738 and 4.869 Å for LDA and GGA, respectively. For LiH, KH, RbH, and CsH, the lattice constants obtained from lattice dynamics calculations at 298 K are 4.002, 5.564, 5.831, and 6.205 Å, respectively, compared to the experimental values of 4.084 [145], 5.704 [146], 6.037 [147],27 and 6.388 Å [148] respectively.

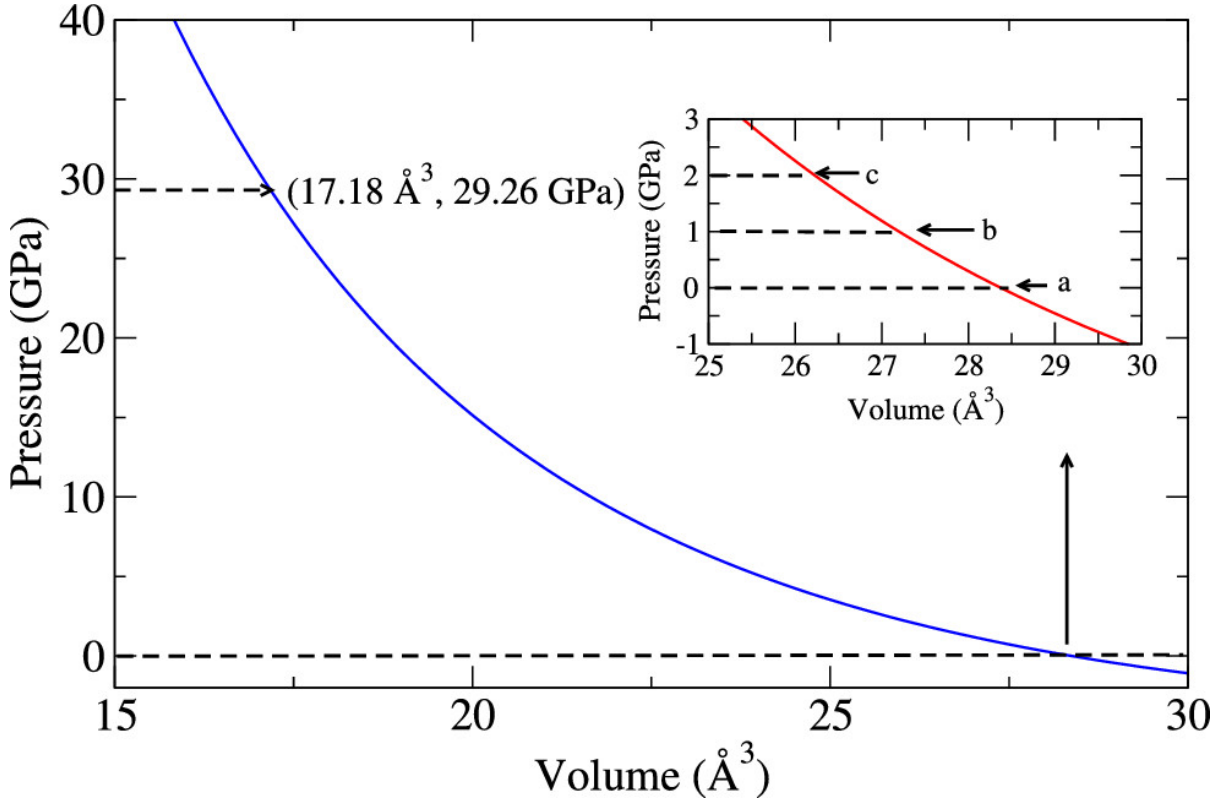

Figure 7.6 Equation of state for the NaCl-type structure of NaH at 298 K. Phase-change volume is shown in the small bracket. The experimental regions are shown in the inset by the arrows where inelastic neutrons scattering (INS) are simulated using the Oclimax software. "a" represents the equilibrium region with zero pressure, "b" and "c" are low-pressure regions with pressures 1 and 2 GPa, respectively.

Table 7.3 Equilibrium Lattice Constant (a), the Bulk Modulus (B_0) and its First Derivative (B_0') for Alkali Hydrides from the Lattice Dynamics Calculations compared to Experimental and Theoretical Results

	LiH (LDA)	NaH (LDA)	NaH(GGA)	KH (LDA)	RbH (LDA)	CsH (LDA)
			a (Å)			
QHA 298 K	4.002	4.843	4.990	5.564	5.831	6.205
QHA 298 K [129]	4.038	4.855	4.976	5.581	5.907	6.219
QHA 300 K [134]	4.009	4.780	4.948			
static	3.901	4.734	4.867	5.456	5.727	6.101
static [129]	3.938	4.738	4.869	5.469	5.793	6.105
experiment	4.084 [145]	4.89	4.89	5.704	6.037	6.388
B_0 (GPA) at 298 K	31.42	21.46	17.68	14.07	11.63	9.83
experiment	32.20	19.40 ± 2.0	19.40 ± 2.0	15.6 ± 1.5	10.0 ± 1.0	7.6 ± 0.8
B_0' at 298 K	3.59	3.97	4.01	4.36	4.39	3.71
	3.76, 3.81	3.75	3.50			

Table 7.3 shows a comparison of calculated lattice constants with experiments and other theoretical results. Bulk modulus (B_0) and their derivative (B_0') for all alkali hydrides are obtained from the Birch third-order equation of state fit. For the B1 phase of NaH, bulk moduli (B_0) at 298 K from LDA and GGA are, respectively, 21.46 and 17.68 GPa, compared to the experimental value of 19.40 ± 2.0 GPa [127]. The calculated first derivatives of bulk modulus (B_0') from LDA and GGA are 3.97 and 4.01, respectively. These values are close to 3.75 and 3.50 obtained from the other theoretical calculation [130]. B_0 and B_0' for other alkali hydrides from LDA lattice dynamics calculations are reported in Table 7.3.

7.4.3 Phonon Dispersion and Born Charges

Phonon dispersion for the B1 phase of NaH from lattice dynamics calculation with LDA (solid lines) compared to the one from molecular dynamics trajectories (broken lines) is shown in Figure 7.7. For the equilibrium volume (V_0) at 5 K (Figure 7.7a), phonon modes are stable. We have calculated phonon dispersion for experimental pressures of 1 GPa (Figure 7.7b) and 2 GPa (Figure 7.7c) and compared with the one from the finite-temperature phonon calculations using molecular dynamics (MD) trajectories (broken lines), which show negligible anharmonic effect for the given temperature (500 K) and pressures. It is important to note that the 500 K temperature for MD is chosen to incorporate the distinct anharmonic effect in the calculations. On decreasing the volume to the phase-change value $V = 0.61V_0$, the transverse acoustic (TA) branch becomes unstable at the zone boundary (1/2, 0, 1/2), as shown in Figure 7.7d, while the transverse optical (TO), longitudinal optical (LO), and the longitudinal acoustic (LA) phonon modes shift to higher frequencies. This instability of the TA

mode indicates the structural instability and the phase change.

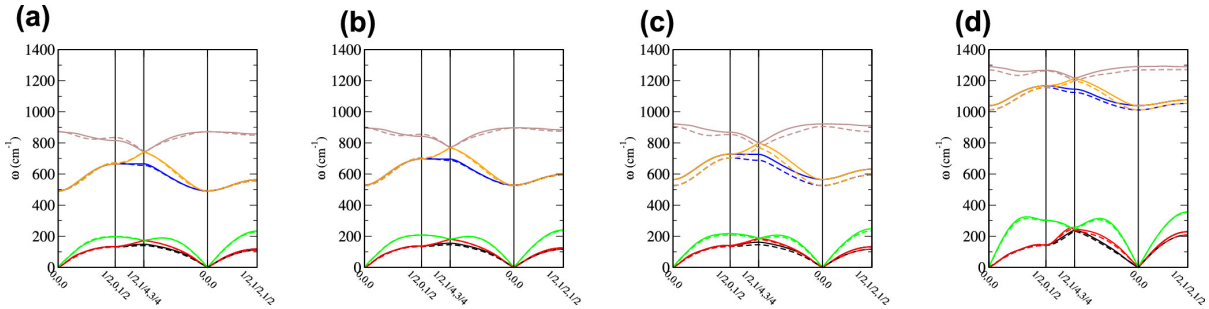

Figure 7.7 Phonon dispersion of NaH at different pressures. Solid lines are from the lattice dynamics calculations and the broken lines are from the finite-temperature phonon calculations from the MD trajectories. (a) NaH at V_0 (equilibrium volume), (b) NaH at V/V_0 = 0.96 (1 GPa), (c) NaH at V/V_0 = 0.92 (2 GPa) and (d) NaH at V/V_0 = 0.61 (PCP).

We have calculated the phonon dispersion for NaH using LDA at pressures just before and after the TA acoustic mode softens to zero at the zone boundary (1/2, 0, 1/2), which are shown in Figure 7.8. The softening to negative frequencies occurs at a volume ratio of V/V_0 = 0.46 and a pressure of 81.55 GPa, which is much higher than the phase-change pressure. Other alkali hydrides show a similar type of phonon softening at higher pressures. Zhang et al. have estimated the volume change for phonon softening to zero frequency for NaH as 0.44 V_0 at a pressure of 90 GPa [128] and estimated it as a phasechange pressure. Our results conclude that the pressure at which phonon softens to zero provides an inaccurate estimate to the phase-change pressure, and the lattice dynamics calculations incorporating zero-point energy and thermal effect are essential for the correct thermodynamic description of the phase-change behavior. In other words, the criterion to determine the relative stability of the phases is their Gibbs free energy and not the phonon softening.

It has been established that the effective charges, such as Szigeti effective charge

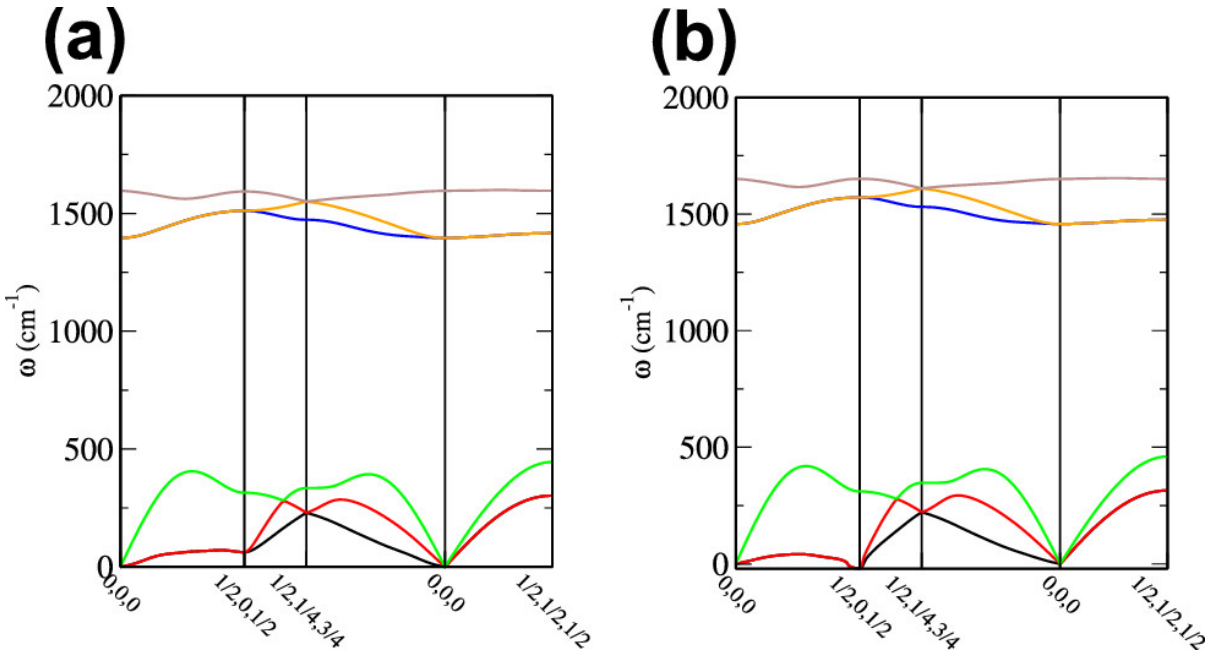

Figure 7.8 Phonon dispersion of NaH at volumes before and after phonon softening to zero. (a) NaH at V/V_0 = 0.48 (P = 71.76 GPa) and (b) NaH at V/V_0 = 0.46 (P = 81.55 GPa).

[149], are fundamental in the LO-TO splitting. To investigate the effect of Born effective charges (Z^*) on LO-TO splitting at different pressures, we have calculated the Born effective charges (Z^*) at different pressures for NaH, which is shown in Table 7.4. For the equilibrium volume at 5 K (0 K), 1, 2 GPa and phase-change volume (PCP), the charges are 0.997, 0.986, 0.975, and 0.838, respectively. We have calculated the LO-TO gap ($\Delta\omega$) for all four pressures, which are shown in Table 7.4. As expected, both the Born charges and LO-TO gap decrease with pressure.

7.5 Summary and Conclusions

In this study, we have carried out the inelastic neutron spectroscopy (INS) experiments of NaH at 1 and 2 GPa pressures and benchmarked the results obtained from ab initio

Table 7.4 Calculated Born Effective Charges and LO-TO Gap for NaH at Different Pressures

NaH (LDA)			
	born charge (Z^*)	LO-TO gap ($\Delta\omega(cm^{-1})$)	V/V_0
0 GPa	0.997	377.464	1.00
1 GPa	0.986	368.885	0.96
2 GPa	0.975	354.588	0.92
PCP (29.26 GPa)	0.838	248.780	0.61

plane-wave pseudopotential lattice dynamics calculations using different functionals. We have found that the results of lattice dynamics calculations from LDA agree better with the experiments compared to that from GGA. Based on experimental results and theoretical calculations, we have successfully investigated various thermodynamical properties. We have reported the calculated lattice constants, bulk modulus, and its derivatives for all alkali hydrides and compared them with experimental results and other theoretical works. We have shown that the phonon softening to negative frequencies is insufficient to predict the phase-change pressure, and both the zero-point energy and the thermal contributions to static energy are essential for its accurate prediction. We have demonstrated that the criteria for the relative stability of the phases are their Gibbs free energy. We have successfully shown that the INS spectroscopy can be a useful tool in benchmarking results from different theoretical methods, including the high-pressure conditions, as well as in benchmarking DFT functionals.

CHAPTER 8

SUMMARY AND OUTLOOK

This dissertation describes vibrational spectroscopy studies of multiple complex materials, including alkali hydrides, zirconium hydrides, etc., by combining various simulation methods including DFT, MD, and lattice dynamics procedures, with the experimental technique INS. Several research problems, including large-scale and anharmonic phonon calculation methodologies, anharmonicity of zirconium hydrides, and high-pressure induced phase change effects in alkali hydrides have been studied or addressed.

In chapter 5, we have implemented the phonon calculations methodology for large-scale systems based on lattice dynamics methods and anharmonic systems based on MD methods with the real-space multigrid DFT code RMG, and have validated our implementations by comparing phonon dispersions and/or INS spectra from RMG with results from other DFT codes and INS experiments. Potential applications

of this work include studies of defects/boundaries effects in crystals, or phonon calculations for low-symmetry structures, when system sizes can be very large or high computing power is required; and in studies of thermal physics, material stability and phase transitions, when anharmonicity plays an important role. Possible extensions of this work include integration of compressive sensing in MD simulations [150] to estimate anharmonic IFCs with only non-negligible contributions, thus to reduce the computational cost and avoid the overfitting issue.

In chapter 6, by sampling 2D potential energy surfaces using DFT, we have successfully confirmed that the anharmonicity in zirconium hydrides comes from the deviations of potential energy surfaces from parabolas in certain directions. By solving the corresponding 2D Schrödinger equations, the phonon frequencies can well predict anharmonic peaks beyond the harmonic approximation with reasonable accuracy. This work could shed light on the phonon studies in systems like TiH_x, PdH_x, and other metal-hydrogen systems sharing similar anharmonic phonon beharviors with zirconium hydrides. One possible direction to extend this work is to sample potential energy surfaces and solve the Schrödinger equations in 3D space to obtain more accurate phonons, but more powerful computing resources would be necessary.

In chapter 7, our work on sodium hydrides has demonstrated that phonon softening is not sufficient to predict the phase-change pressure, and the criteria for the relative stabilities of phases require incorporations of thermal contributions of phonons into the Gibbs free energy. We also found that LDA performs better than GGA under high pressure for this system.

BIBLIOGRAPHY

[1] Viljas, J. & Heikkilä, T. "Electron-phonon heat transfer in monolayer and bilayer graphene". *Physical Review B* **81**.24 (2010), p. 245404.

[2] Klitsner, T. et al. "Phonon radiative heat transfer and surface scattering". *Physical Review B* **38**.11 (1988), p. 7576.

[3] Peterson, R. "Direct simulation of phonon-mediated heat transfer in a Debye crystal" (1994).

[4] Snyder, G. J. & Toberer, E. S. "Complex thermoelectric materials". *materials for sustainable energy: a collection of peer-reviewed research and review articles from Nature Publishing Group*. World Scientific, 2011, pp. 101–110.

[5] Boukai, A. I. et al. "Silicon nanowires as efficient thermoelectric materials". *Nature* **451**.7175 (2008), pp. 168–171.

[6] Dresselhaus, M. S. et al. "New directions for low-dimensional thermoelectric materials". *Advanced materials* **19**.8 (2007), pp. 1043–1053.

[7] Oura, K. et al. *Surface science: an introduction*. Springer Science & Business Media, 2013.

[8] Szeftel, J. "Surface phonon dispersion, using electron energy loss spectroscopy". *Surface Science* **152** (1985), pp. 797–810.

[9] Li, N. et al. "Colloquium: Phononics: Manipulating heat flow with electronic analogs and beyond". *Reviews of Modern Physics* **84**.3 (2012), p. 1045.

[10] Maldovan, M. "Sound and heat revolutions in phononics". *Nature* **503**.7475 (2013), p. 209.

[11] Ruskov, R. & Tahan, C. "Coherent phonons as a new element of quantum computing and devices". *Journal of Physics: Conference Series*. Vol. 398. 1. IOP Publishing. 2012, p. 012011.

[12] Macridin, A. et al. "Electron-Phonon Systems on a Universal Quantum Computer". *Physical review letters* **121**.11 (2018), p. 110504.

[13] Born, M. & Huang, K. "Dynamical theory of crystal lattices Oxford University Press". *London, New York* (1954).

[14] Parr, R. G. "Density functional theory of atoms and molecules". *Horizons of Quantum Chemistry*. Springer, 1980, pp. 5–15.

[15] Runge, E. & Gross, E. K. "Density-functional theory for time-dependent systems". *Physical Review Letters* **52**.12 (1984), p. 997.

[16] Kresse, G et al. "Ab initio force constant approach to phonon dispersion relations of diamond and graphite". *EPL (Europhysics Letters)* **32**.9 (1995), p. 729.

[17] Parlinski, K et al. "First-principles determination of the soft mode in cubic ZrO 2". *Physical Review Letters* **78**.21 (1997), p. 4063.

[18] Ackland, G. et al. "Practical methods in ab initio lattice dynamics". *Journal of Physics: Condensed Matter* **9**.37 (1997), p. 7861.

[19] Giannozzi, P. et al. "Ab initio calculation of phonon dispersions in semiconductors". *Physical Review B* **43**.9 (1991), p. 7231.

[20] Gonze, X. & Lee, C. "Dynamical matrices, Born effective charges, dielectric permittivity tensors, and interatomic force constants from density-functional perturbation theory". *Physical Review B* **55**.16 (1997), p. 10355.

[21] Gaskell, T. "Velocity autocorrelation function and diffusion coefficient in a liquid". *Journal of Physics C: Solid State Physics* **4**.12 (1971), p. 1466.

[22] Hellman, O. et al. "Lattice dynamics of anharmonic solids from first principles". *Physical Review B* **84**.18 (2011), p. 180301.

[23] Kong, L. T. et al. "An improved version of the Green's function molecular dynamics method". *Computer Physics Communications* **182**.2 (2011), pp. 540–541.

[24] Zhang, J. et al. "Large-Scale Phonon Calculations Using the Real-Space Multigrid Method". *Journal of chemical theory and computation* **15**.12 (2019), pp. 6859–6864.

[25] Stuart, B. "Infrared spectroscopy". *Kirk-Othmer Encyclopedia of Chemical Technology* (2000), pp. 1–18.

[26] Long, D. A. & Long, D. *Raman spectroscopy*. Vol. 276. McGraw-Hill New York, 1977.

[27] Dederichs, P. "The theory of diffuse X-ray scattering and its application to the study of point defects and their clusters". *Journal of Physics F: Metal Physics* **3**.2 (1973), p. 471.

[28] Hillier, J. & Baker, R. "Microanalysis by means of electrons". *Journal of Applied Physics* **15**.9 (1944), pp. 663–675.

[29] Benedek, G. et al. *Helium atom scattering from surfaces*. Vol. 27. Springer Science & Business Media, 2013.

[30] Mitchell, P. C. H. *Vibrational spectroscopy with neutrons: with applications in chemistry, biology, materials science and catalysis*. Vol. 3. World Scientific, 2005.

[31] Parker, S. F. et al. "Vibrational spectroscopy with neutrons: recent developments". *Spectrochimica Acta Part A: Molecular and Biomolecular Spectroscopy* **190** (2018), pp. 518–523.

[32] Hohenberg, P & Kohn, W. "Density Functional Theory (DFT)". *Phys. Rev* **136** (1964), B864.

[33] Kohn, W. & Sham, L. J. "Self-consistent equations including exchange and correlation effects". *Physical review* **140**.4A (1965), A1133.

[34] Ceperley, D. & Alder, B. "Phys. Rev. Lett. 45, 566 (1980)". *J. Perdew and A. Zunger, Phys. Rev. B* **23** (1981), p. 5048.

[35] Perdew, J. P. & Zunger, A. "Self-interaction correction to density-functional approximations for many-electron systems". *Physical Review B* **23**.10 (1981), p. 5048.

[36] Perdew, J. P. et al. "Generalized gradient approximation made simple". *Physical review letters* **77**.18 (1996), p. 3865.

[37] Briggs, E. et al. "Large-scale electronic-structure calculations with multigrid acceleration". *Physical Review B* **52**.8 (1995), R5471.

[38] Briggs, E. et al. "Real-space multigrid-based approach to large-scale electronic structure calculations". *Physical Review B* **54**.20 (1996), p. 14362.

[39] Hamann, D. et al. "Norm-conserving pseudopotentials". *Physical Review Letters* **43**.20 (1979), p. 1494.

[40] Vanderbilt, D. "Soft self-consistent pseudopotentials in a generalized eigenvalue formalism". *Physical review B* **41**.11 (1990), p. 7892.

[41] Blöchl, P. E. "Projector augmented-wave method". *Physical review B* **50**.24 (1994), p. 17953.

[42] Kresse, G. & Joubert, D. "From ultrasoft pseudopotentials to the projector augmented-wave method". *Physical review b* **59**.3 (1999), p. 1758.

[43] Hodak, M. et al. "Implementation of ultrasoft pseudopotentials in large-scale grid-based electronic structure calculations". *Physical Review B* **76**.8 (2007), p. 085108.

[44] Chelikowsky, J. R. et al. "Finite-difference-pseudopotential method: Electronic structure calculations without a basis". *Physical review letters* **72**.8 (1994), p. 1240.

[45] Daw, M. S. & Baskes, M. I. "Embedded-atom method: Derivation and application to impurities, surfaces, and other defects in metals". *Physical Review B* **29**.12 (1984), p. 6443.

[46] Van Duin, A. C. et al. "ReaxFF: a reactive force field for hydrocarbons". *The Journal of Physical Chemistry A* **105**.41 (2001), pp. 9396–9409.

[47] Feynman, R. P. "Forces in molecules". *Physical Review* **56**.4 (1939), p. 340.

[48] Car, R. & Parrinello, M. "Unified approach for molecular dynamics and density-functional theory". *Physical review letters* **55**.22 (1985), p. 2471.

[49] Andersen, H. C. "Molecular dynamics simulations at constant pressure and/or temperature". *The Journal of chemical physics* **72**.4 (1980), pp. 2384–2393.

[50] Nosé, S. "A unified formulation of the constant temperature molecular dynamics methods". *The Journal of chemical physics* **81**.1 (1984), pp. 511–519.

[51] Hoover, W. G. "Canonical dynamics: Equilibrium phase-space distributions". *Physical review A* **31**.3 (1985), p. 1695.

[52] Pick, R. M. et al. "Microscopic theory of force constants in the adiabatic approximation". *Physical Review B* **1**.2 (1970), p. 910.

[53] Wikipedia contributors. *Morse potential*. [Online; accessed 4-April-2020]. 2020.

[54] Baroni, S. et al. "Green's-function approach to linear response in solids". *Physical Review Letters* **58**.18 (1987), p. 1861.

[55] Gonze, X. et al. "Dielectric tensor, effective charges, and phonons in α-quartz by variational density-functional perturbation theory". *Physical Review Letters* **68**.24 (1992), p. 3603.

[56] Gonze, X. "First-principles responses of solids to atomic displacements and homogeneous electric fields: Implementation of a conjugate-gradient algorithm". *Physical Review B* **55**.16 (1997), p. 10337.

[57] Baroni, S. et al. "Phonons and related crystal properties from density-functional perturbation theory". *Reviews of Modern Physics* **73**.2 (2001), p. 515.

[58] Shang, H. et al. "Lattice dynamics calculations based on density-functional perturbation theory in real space". *Computer Physics Communications* **215** (2017), pp. 26–46.

[59] Fon, W et al. "Phonon scattering mechanisms in suspended nanostructures from 4 to 40 K". *Physical review B* **66**.4 (2002), p. 045302.

[60] Li, C. W. et al. "Orbitally driven giant phonon anharmonicity in SnSe". *Nature Physics* **11**.12 (2015), p. 1063.

[61] Budai, J. D. et al. "Metallization of vanadium dioxide driven by large phonon entropy". *Nature* **515**.7528 (2014), p. 535.

[62] Li, F. et al. "High-resolution phonon energy shift measurements with the inelastic neutron spin echo technique". *Journal of Applied Crystallography* **52**.4 (2019).

[63] Kaasbjerg, K. et al. "Phonon-limited mobility in n-type single-layer MoS 2 from first principles". *Physical Review B* **85**.11 (2012), p. 115317.

[64] Noffsinger, J. et al. "Phonon-assisted optical absorption in silicon from first principles". *Physical review letters* **108**.16 (2012), p. 167402.

[65] Yildirim, T et al. "Giant anharmonicity and nonlinear electron-phonon coupling in MgB 2: a combined first-principles calculation and neutron scattering study". *Physical review letters* **87**.3 (2001), p. 037001.

[66] Cooper, L. N. "Bound electron pairs in a degenerate Fermi gas". *Physical Review* **104**.4 (1956), p. 1189.

[67] Bardeen, J. et al. "Microscopic theory of superconductivity". *Physical Review* **106**.1 (1957), p. 162.

[68] Eliashberg, G. "Interactions between electrons and lattice vibrations in a superconductor". *Sov. Phys. JETP* **11**.3 (1960), pp. 696–702.

[69] Allen, P. B. & Mitrović, B. "Theory of superconducting Tc". *Solid state physics*. Vol. 37. Elsevier, 1983, pp. 1–92.

[70] Togo, A. et al. "Distributions of phonon lifetimes in Brillouin zones". *Physical Review B* **91**.9 (2015), p. 094306.

[71] Estreicher, S. et al. "Phonons and defects in semiconductors and nanostructures: Phonon trapping, phonon scattering, and heat flow at heterojunctions". *Journal of Applied Physics* **115**.1 (2014), p. 012012.

[72] Liu, W & Asheghi, M. "Phonon–boundary scattering in ultrathin single-crystal silicon layers". *Applied Physics Letters* **84**.19 (2004), pp. 3819–3821.

[73] Asheghi, M et al. "Phonon-boundary scattering in thin silicon layers". *Applied Physics Letters* **71**.13 (1997), pp. 1798–1800.

[74] Sanders, D. & Walton, D. "Effect of magnon-phonon thermal relaxation on heat transport by magnons". *Physical Review B* **15**.3 (1977), p. 1489.

[75] Streib, S. et al. "Magnon-phonon interactions in magnetic insulators". *Physical Review B* **99**.18 (2019), p. 184442.

[76] Lindsay, L et al. "Thermal conductivity and large isotope effect in GaN from first principles". *Physical review letters* **109**.9 (2012), p. 095901.

[77] Lindsay, L et al. "Phonon-isotope scattering and thermal conductivity in materials with a large isotope effect: A first-principles study". *Physical Review B* **88**.14 (2013), p. 144306.

[78] Charsley, P et al. "An experimental investigation of dislocation-phonon scattering in some copper alloys". *physica status solidi (b)* **25**.2 (1968), pp. 531–540.

[79] Wang, T. et al. "Phonon scattering by dislocations in GaN". *ACS applied materials & interfaces* **11**.8 (2019), pp. 8175–8181.

[80] Kong, L. T. et al. "Implementation of Green's function molecular dynamics: An extension to LAMMPS". *Computer Physics Communications* **180**.6 (2009), pp. 1004–1010.

[81] Kong, L. T. "Phonon dispersion measured directly from molecular dynamics simulations". *Computer Physics Communications* **182**.10 (2011), pp. 2201–2207.

[82] Hellman, O. et al. "Temperature dependent effective potential method for accurate free energy calculations of solids". *Physical Review B* **87**.10 (2013), p. 104111.

[83] Hellman, O. & Abrikosov, I. A. "Temperature-dependent effective third-order interatomic force constants from first principles". *Physical Review B* **88**.14 (2013), p. 144301.

[84] Cheng, Y. et al. "Simulation of inelastic neutron scattering spectra using OCLIMAX". *Journal of chemical theory and computation* **15**.3 (2019), pp. 1974–1982.

[85] Squires, G. L. *Introduction to the theory of thermal neutron scattering*. Courier Corporation, 1996.

[86] Chou, W. "Spallation Neutron Source and other high intensity proton sources". *Accelerator Physics, Technology And Applications: Selected Lectures of OCPA International Accelerator School 2002*. World Scientific, 2004, pp. 231–255.

[87] Ramirez-Cuesta, A. "aCLIMAX 4.0. 1, The new version of the software for analyzing and interpreting INS spectra". *Computer Physics Communications* **157**.3 (2004), pp. 226–238.

[88] Togo, A. & Tanaka, I. "First principles phonon calculations in materials science". *Scripta Materialia* **108** (2015), pp. 1–5.

[89] Wang, Y. et al. "First-principles calculations of lattice dynamics and thermal properties of polar solids". *npj Computational Materials* **2** (2016), p. 16006.

[90] Tadano, T. et al. "Anharmonic force constants extracted from first-principles molecular dynamics: applications to heat transfer simulations". *Journal of Physics: Condensed Matter* **26**.22 (2014), p. 225402.

[91] Kathmann, S. M. et al. "Understanding Vibrational Anharmonicity and Phonon Dispersion in Solid Ammonia Borane". *The Journal of Physical Chemistry C* **116**.9 (2012), pp. 5926–5931.

[92] Alfe, D. "PHON: A program to calculate phonons using the small displacement method". *Computer Physics Communications* **180**.12 (2009), pp. 2622–2633.

[93] Giannozzi, P. et al. "Advanced capabilities for materials modelling with Quantum ESPRESSO". *Journal of Physics: Condensed Matter* **29**.46 (2017), p. 465901.

[94] Kresse, G. & Furthmüller, J. "Efficiency of ab-initio total energy calculations for metals and semiconductors using a plane-wave basis set". *Computational materials science* **6**.1 (1996), pp. 15–50.

[95] Clark, S. J. et al. "First principles methods using CASTEP". *Zeitschrift für Kristallographie-Crystalline Materials* **220**.5/6 (2005), pp. 567–570.

[96] Blomqvist, J. et al. "Structure and Thermodynamical Properties of Zirconium hydrides from first-principle". *Proceedings of the 15th International Conference on Environmental Degradation of Materials in Nuclear Power Systems—Water Reactors*. Springer. 2011, pp. 671–681.

[97] Chattaraj, D et al. "First principles study of the ZrX2 (X= H, D and T) compounds". *International Journal of Hydrogen Energy* **39**.18 (2014), pp. 9681–9689.

[98] Kolesnikov, A. et al. "Inelastic neutron scattering study of ordered gamma-ZrH". *Journal of Physics: Condensed Matter* **6**.43 (1994), p. 8989.

[99] Grimsdale, A. & Jacob, J. "Polymer-Based LEDs and Solar Cells" (2016).

[100] Wang, Y. et al. "Zinc Imidazolate Metal–Organic Frameworks (ZIF-8) for Electrochemical Reduction of CO2 to CO". *ChemPhysChem* **18**.22 (2017), pp. 3142–3147.

[101] Bickel, P. & Berlincourt, T. "Electrical properties of hydrides and deuterides of zirconium". *Physical Review B* **2**.12 (1970), p. 4807.

[102] Holliger, L. et al. "Hexagonal-based ordered phases in H-Zr". *Physical Review B* **80**.9 (2009), p. 094111.

[103] Huangs, J. et al. "Estimation of hydrogen redistribution in zirconium hydride under temperature gradient". *Journal of nuclear science and technology* **37**.10 (2000), pp. 887–892.

[104] Zuzek, E et al. "The H-Zr (hydrogen-zirconium) system". *Bulletin of alloy phase diagrams* **11**.4 (1990), pp. 385–395.

[105] Setoyama, D. & Yamanaka, S. "Phase diagram of Zr–O–H ternary system". *Journal of alloys and compounds* **370**.1-2 (2004), pp. 144–148.

[106] Dupin, N et al. "A thermodynamic database for zirconium alloys". *Journal of nuclear materials* **275**.3 (1999), pp. 287–295.

[107] Zhao, Z. et al. "Identification and characterization of a new zirconium hydride". *Journal of microscopy* **232**.3 (2008), pp. 410–421.

[108] Weck, P. F. et al. "Mechanical properties of zirconium alloys and zirconium hydrides predicted from density functional perturbation theory". *Dalton Transactions* **44**.43 (2015), pp. 18769–18779.

[109] Yamanaka, S et al. "Thermal and mechanical properties of zirconium hydride". *Journal of Alloys and Compounds* **293** (1999), pp. 23–29.

[110] Ackland, G. "Embrittlement and the bistable crystal structure of zirconium hydride". *Physical review letters* **80**.10 (1998), p. 2233.

[111] Elsässer, C et al. "Hydrogen Vibration in Cubic Dihydrides MH 2 (M= Ti, Zr), and Localization in Cubic Laves Phases ZrM 2 H 1/2 (M= V, Cr, Fe, Co)". *MRS Online Proceedings Library Archive* **453** (1996).

[112] Ikeda, S. et al. "Crystal analyser TOF spectrometer (CAT)". *Physica B+ C* **120**.1-3 (1983), pp. 131–135.

[113] Kolesnikov, A. et al. "Neutron scattering studies of ordered gamma-ZrD". *Journal of Physics: Condensed Matter* **6**.43 (1994), p. 8977.

[114] Kresse, G. & Hafner, J. "Ab initio molecular dynamics for liquid metals". *Physical Review B* **47**.1 (1993), p. 558.

[115] *RMG Website*. `https://www.rmgdft.org/`. Accessed: 2020-04-08.

[116] Perdew, J. P. et al. "Atoms, molecules, solids, and surfaces: Applications of the generalized gradient approximation for exchange and correlation". *Physical review B* **46**.11 (1992), p. 6671.

[117] Methfessel, M. & Paxton, A. "High-precision sampling for Brillouin-zone integration in metals". *Physical Review B* **40**.6 (1989), p. 3616.

[118] Seeger, P. A. et al. "Resolution of VISION, a crystal-analyzer spectrometer". *Nuclear Instruments and Methods in Physics Research Section A: Accelerators, Spectrometers, Detectors and Associated Equipment* **604**.3 (2009), pp. 719–728.

[119] Penfold, J & Tomkinson, J. *Rutherford Appleton Lab. Internal Rep*. Tech. rep. RAL-86-019, 1986.

[120] Rundle, R. et al. "The crystal structure of thorium and zirconium dihydrides by X-ray and neutron diffraction". *Acta Crystallographica* **5**.1 (1952), pp. 22–26.

[121] Momma, K. & Izumi, F. "VESTA 3 for three-dimensional visualization of crystal, volumetric and morphology data". *Journal of applied crystallography* **44**.6 (2011), pp. 1272–1276.

[122] Hinuma, Y. et al. "Band structure diagram paths based on crystallography". *Computational Materials Science* **128** (2017), pp. 140–184.

[123] Arnold, O. et al. "Mantid—Data analysis and visualization package for neutron scattering and μ SR experiments". *Nuclear Instruments and Methods in Physics Research Section A: Accelerators, Spectrometers, Detectors and Associated Equipment* **764** (2014), pp. 156–166.

[124] Olsson, P. et al. "Ab initio thermodynamics of zirconium hydrides and deuterides". *Computational materials science* **86** (2014), pp. 211–222.

[125] Zhang, P. et al. "First-principles study of ground state properties of ZrH2". *Computational materials science* **50**.12 (2011), pp. 3297–3302.

[126] Duclos, S. J. et al. "High-pressure studies of NaH to 54 GPa". *Physical Review B* **36**.14 (1987), p. 7664.

[127] Hochheimer, H. et al. "High pressure X-ray investigation of the alkali hydrides NaH, KH, RbH, and CsH". *Zeitschrift für Physikalische Chemie* **143**.143 (1985), pp. 139–144.

[128] Zhang, J. et al. "Phonon and elastic instabilities in rocksalt alkali hydrides under pressure: First-principles study". *Physical Review B* **75**.10 (2007), p. 104115.

[129] Barrera, G. et al. "LDA or GGA? A combined experimental inelastic neutron scattering and ab initio lattice dynamics study of alkali metal hydrides". *Chemical physics* **317**.2-3 (2005), pp. 119–129.

[130] Sun, X.-W. et al. "Ab initio study of phase transition and bulk modulus of NaH". *Journal of Solid State Chemistry* **184**.2 (2011), pp. 427–431.

[131] Wang, Y. et al. "LiH under high pressure and high temperature: A first-principles study". *physica status solidi (b)* **235**.2 (2003), pp. 470–473.

[132] Lebègue, S et al. "Pressure-induced simultaneous metal-insulator and structural-phase transitions in LiH: A quasiparticle study". *EPL (Europhysics Letters)* **63**.4 (2003), p. 562.

[133] Pandey, A. et al. "Exposing Key Vibrational Contributions to Properties of Organic Molecular Solids with High Signal, Low Frequency Neutron Spectroscopy and Ab Initio Simulations". *Crystal Growth & Design* **18**.9 (2018), pp. 4815–4821.

[134] Yu, W. et al. "First principles calculation of phonon dispersion, thermodynamic properties and B 1-to-B 2 phase transition of lighter alkali hydrides". *Journal of Physics: Condensed Matter* **19**.8 (2007), p. 086209.

[135] Wallace, D. C. *Thermodynamics of crystals*. Courier Corporation, 1998.

[136] Dove, M. T. & Dove, M. T. *Introduction to lattice dynamics*. Vol. 4. Cambridge university press, 1993.

[137] Birch, F. "Finite elastic strain of cubic crystals". *Physical review* **71**.11 (1947), p. 809.

[138] Ghosez, P. et al. "Dynamical atomic charges: The case of AB O 3 compounds". *Physical Review B* **58**.10 (1998), p. 6224.

[139] Segall, M. et al. "First-principles simulation: ideas, illustrations and the CASTEP code". *Journal of Physics: Condensed Matter* **14**.11 (2002), p. 2717.

[140] Ernzerhof, M. & Scuseria, G. E. "Assessment of the Perdew–Burke–Ernzerhof exchange-correlation functional". *The Journal of chemical physics* **110**.11 (1999), pp. 5029–5036.

[141] Gonze, X. et al. "Interatomic force constants from first principles: The case of α-quartz". *Physical Review B* **50**.17 (1994), p. 13035.

[142] George, L. & Saxena, S. K. "Structural stability of metal hydrides, alanates and borohydrides of alkali and alkali-earth elements: a review". *International Journal of Hydrogen Energy* **35**.11 (2010), pp. 5454–5470.

[143] Ahuja, R et al. "Theoretical search for the CrB-type high-pressure phase in LiH, NaH, KH and RbH". *Physica B: Condensed Matter* **265**.1-4 (1999), pp. 87–91.

[144] Shull, C. et al. "Neutron diffraction studies of NaH and NaD". *Physical Review* **73**.8 (1948), p. 842.

[145] Loubeyre, P et al. "Equation of state of 7 LiH and 7 LiD from x-ray diffraction to 94 GPa". *Physical Review B* **57**.17 (1998), p. 10403.

[146] Kuznetsov, V. & Shkrabkina, M. "X-ray diffraction study of NaH and KH at temperatures from 20 to 400 C". *Journal of Structural Chemistry* **3**.5 (1962), pp. 532–537.

[147] Hooper, J. et al. "Pressure induced structural transitions in KH, RbH, and CsH". *Journal of Applied Physics* **111**.11 (2012), p. 112611.

[148] Ponyatovskii, E. & Bashkin, I. "New phase transitions in hydrides of the ia, iii-a, and iv-a group metals". *Zeitschrift für Physikalische Chemie* **146**.2 (1985), pp. 137–157.

[149] Szigeti, B. "Compressibility and absorption frequency of ionic crystals". *Proceedings of the Royal Society of London. Series A. Mathematical and Physical Sciences* **204**.1076 (1950), pp. 51–62.

[150] Zhou, F. et al. "Lattice anharmonicity and thermal conductivity from compressive sensing of first-principles calculations". *Physical review letters* **113**.18 (2014), p. 185501.

APPENDIX

APPENDIX A

SUPPLEMENTARY INFORMATION FOR CHAPTER 6

A.1 Eigen states based on 2D Schrödinger equation

We have sampled 2D potential energy surfaces of all three materials and solved the according Schrödinger equations as shown in Eq. 6.2 in the original article. The eigenstates with the lowest 15 energies, which represent the wavefunctions of the single hydrogen/deuterium atom, are plotted in Fig. A.1. The black texts above the green background are indicating eigenfrequencies in meV, and areas in blue/red are wavefunctions.

A.2 Comparisons of eigenfrequencies among ZrH_x

Based on the eigenfrequencies in Fig. A.1 (and more not plotted), we plot in Fig. A.2 a figure showing the differences of eigenfrequencies below 1000 meV for three materials.

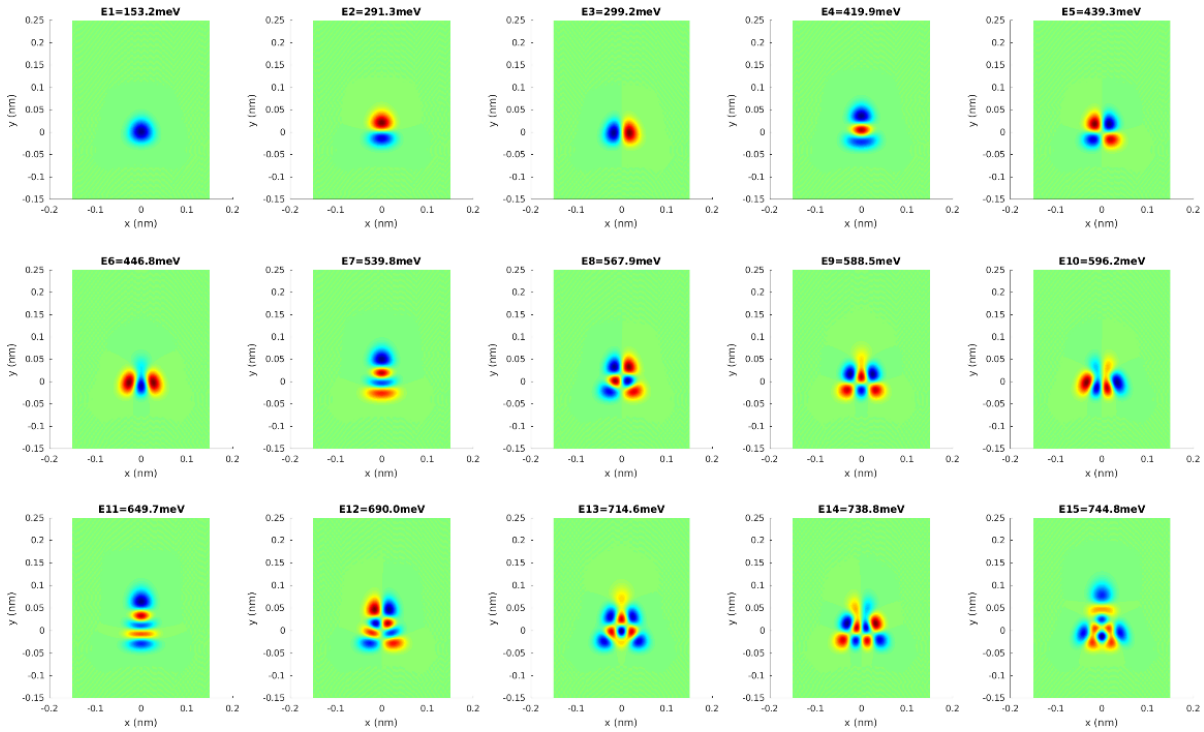
E1=153.2meV
E2=291.3meV
E3=299.2meV
E4=419.9meV
E5=439.3meV
E6=446.8meV
E7=539.8meV
E8=567.9meV
E9=588.5meV
E10=596.2meV
E11=649.7meV
E12=690.0meV
E13=714.6meV
E14=738.8meV
E15=744.8meV
x (nm)
y (nm)

(a)

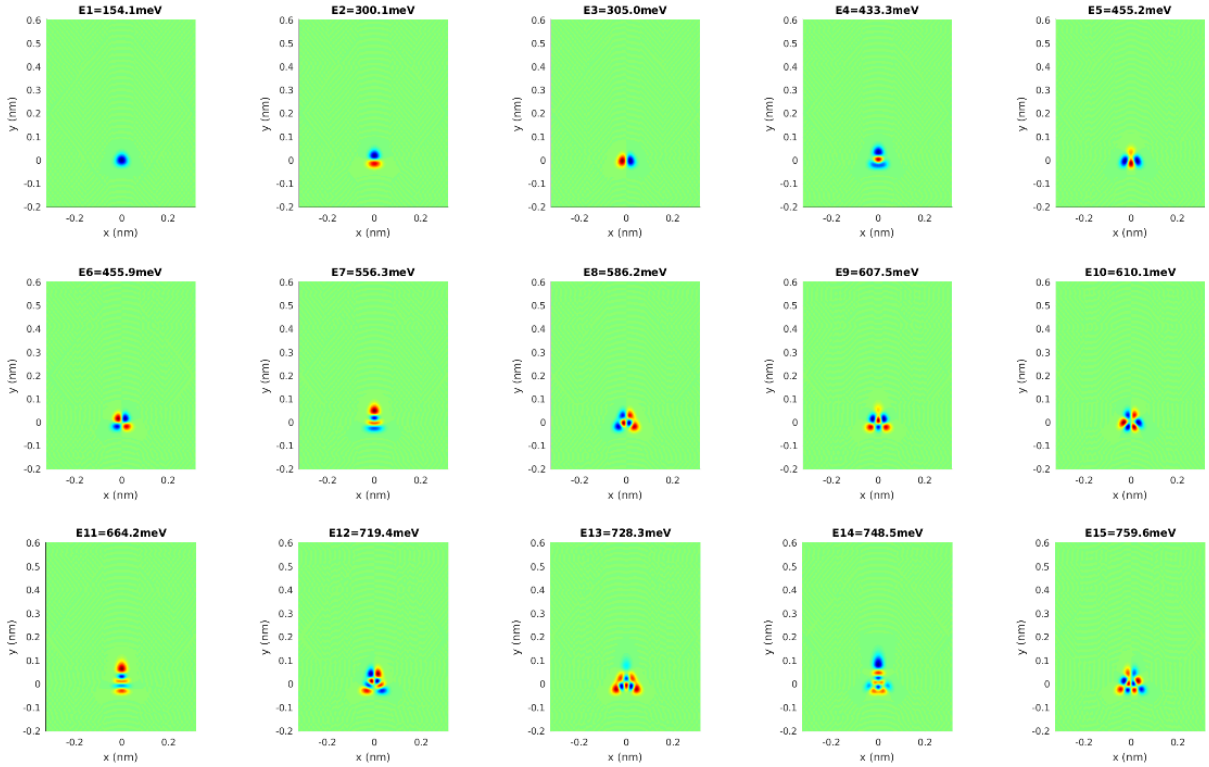
E1=154.1meV
E2=300.1meV
E3=305.0meV
E4=433.3meV
E5=455.2meV
E6=455.9meV
E7=556.3meV
E8=586.2meV
E9=607.5meV
E10=610.1meV
E11=664.2meV
E12=719.4meV
E13=728.3meV
E14=748.5meV
E15=759.6meV
x (nm)
y (nm)

(b)

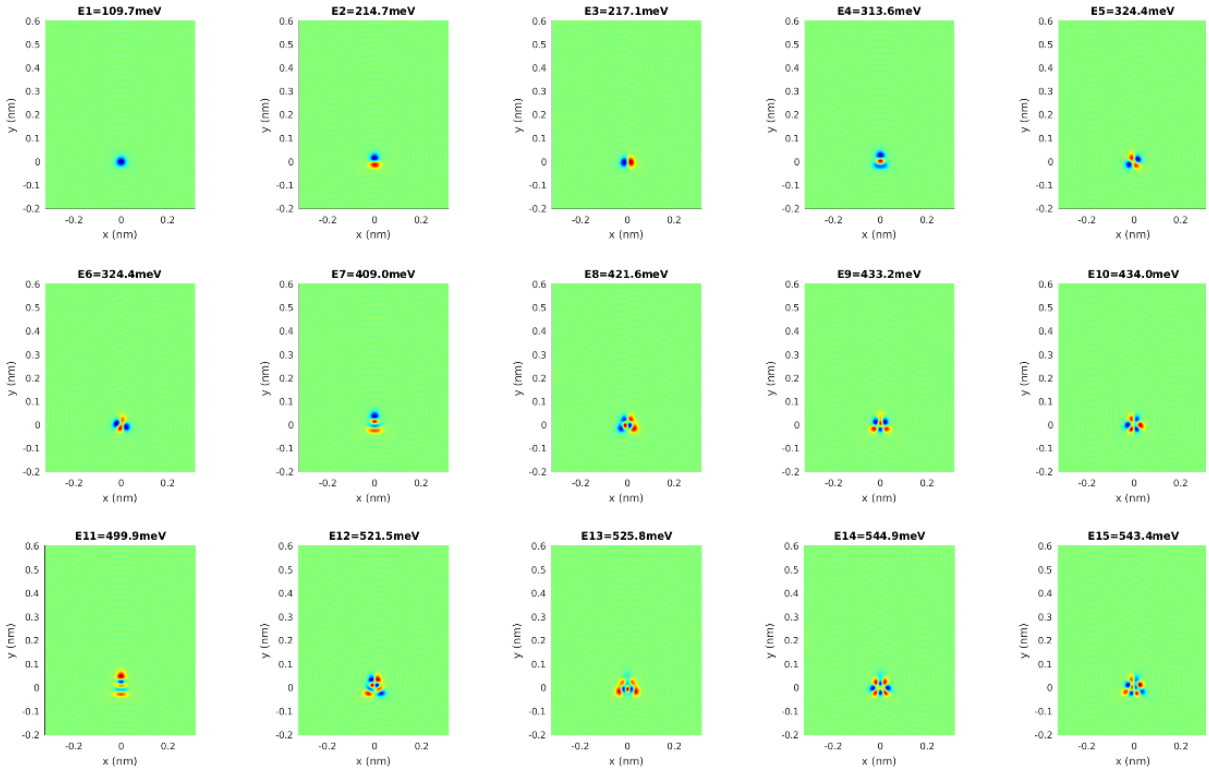

(c)

Figure A.1 First fifteen eigenfrequencies and wavefunctions of H/D for: (a) (112) plane of ϵ-ZrH_2, (b) (-112) plane of ZrH, and (c) (-112) plane of ZrD.

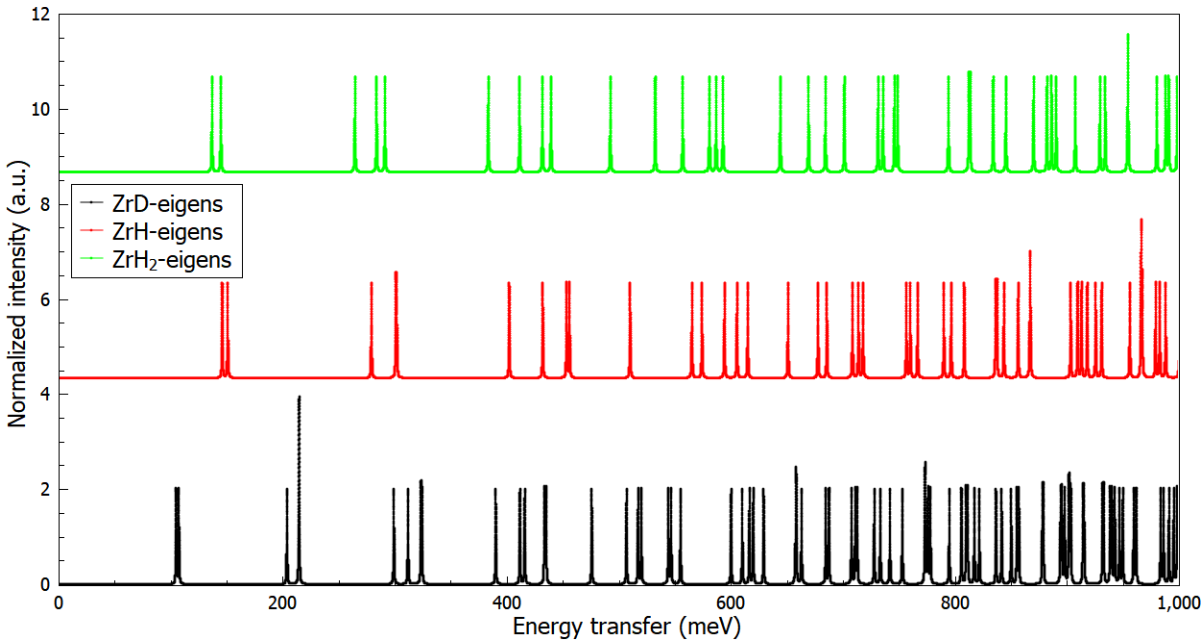

Figure A.2 Comparisons of eigenfrequencies by solving Schrödinger equations for ZrH_x in the energy range below 1000 meV.

A.3 The probability distribution of H atoms in ZrH_2

According to quantum theory, the probability distribution of a particle is the modulus squared of the particle's wavefunctions:

$$\rho(\mathbf{r}) = c|\psi(\mathbf{r})|^2 \tag{A.1}$$

where c is the normalization factor. To quantitatively obtain the spatial distribution of the hydrogen atom, the (unnormalized) probability distributions of hydrogen in (112) plane along x and y directions (with y=0 and x=0, respectively) in ZrH_2 are plotted in Fig. A.3. The dashed lines are indicating the full width at half maximum.

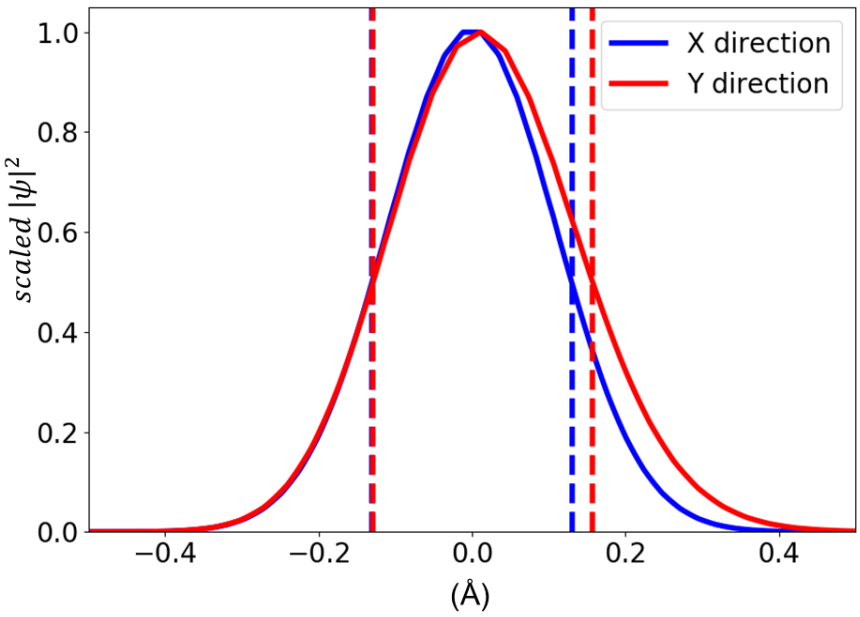

Figure A.3 Unnomalized probability distributions of H atom in ZrH_2 in (112) plane along x (blue) and y (red) directions, where the dashed lines are indicating full width at half maximum (FWHM).